UNIVERSIDAD AUTONOMA DE MADRID

Departamento de Física de la Materia Condensada

Light-matter collective modes and orbital magnetic susceptibility in novel materials

Tesis doctoral presentada por

Ángel Gutiérrez Rubio

Directores:
Prof. Francisco Guinea López
Prof. Tobias Stauber

Tutor:
Prof. Guillermo Gómez Santos

Madrid, enero de 2017

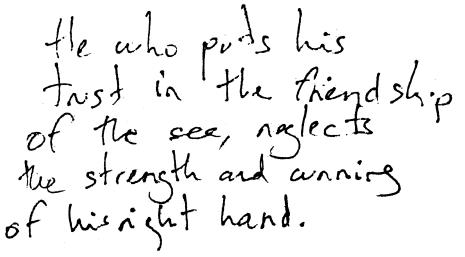

Joseph Conrad

Serán vuestras fazañas los joeces

Solisdán

Agradecimientos

La realización de esta tesis doctoral no hubiera sido posible sin la inestimable ayuda de mis directores, Francisco Guinea y Tobias Stauber. Estoy muy agradecido por su siempre generosa disposición hacia mí que, unida a sus vastos conocimientos, ha contribuido enormemente al desarrollo de mi trabajo y a mi formación como investigador.

No puedo dejar de mencionar el magnífico ambiente con que he topado en el ICMM, fuente constante de inspiración y admiración. Siempre he recibido la más desinteresada y valiosa de las ayudas por parte de todo el grupo de teoría. Mi brevedad es sin duda injusta, pero destacaré en este sentido a Héctor Ochoa, Bruno Amorim, Alberto Cortijo y Rafael Roldán, que encarrilaron mi trabajo durante los primeros años. María Ángeles Vozmediano, Belén Valenzuela, Pablo San José, Laura Fanfarillo, Vincenzo Parente, Jürgen Schiefele y Andreas Bill también me orientaron con acierto, y fue un auténtico placer trabajar con Maurcio Sturla, de quien guardo el mejor de los recuerdos. Añoro mi estancia en la UCSD, las discusiones con el lúcido Michael Fogler y vivir bajo el techo y las costumbres de los Woodington, así como echaré de menos la última etapa, en el IMDEA, que ha sido especialmente grata gracias a la presencia de Franchesca Finocchiaro, Luis González, Luca Chirolli, Ignacio Vincent y José Ángel Silva. Tampoco olvidaré los buenos momentos con mis antiguos compañeros de despacho, Fernando Domínguez, Robert Hussain, Roberto Moreno y Álvaro Gómez, ni el gran apoyo y sabios consejos de Jorge Cayao.

Agradezco también a la Residencia de Estudiantes la cálida acogida y el magnífico trato que allí recibí. Y a los amigos que allí hice, el privilegio de conocerlos, el haberme aportado tanto en el plano personal.

Por último, este trabajo no hubiera sido posible sin el apoyo incondicional y los ánimos de mi familia, a la que le debo todo.

A mi madre

Abstract

This thesis presents several theoretical studies about three novel materials, namely graphene, hexagonal boron nitride (hBN) and MoS_2. The different works are encompassed by light-matter interactions and semiclassical physics. The former aims at the description of the ensuing collective modes, plasmons and polaritons, whereas the latter deals with non-conventional ray optics and the study of the orbital magnetic susceptibility.

In the case of graphene, the linear current-current response function at finite temperature and doping is calculated. Focusing on the transverse channel, we present a thorough characterization of plasmons beyond the local approximation. We analyze their fast damping with temperature, the sensitivity to the surrounding dielectric media and the maximum confinement that can be achieved through different layered setups. Moreover, the absorption of single- and double-layered structures is discussed as a function of the polarization and incident angle of light.

Also in graphene, mass-profile quantum dots are studied as a new mechanism of carrier confinement. Recent experimental techniques involving an Ir substrate allow such a spatial modulation of the gap, which motivates our theoretical approach. We perform an analysis of the spectrum including the effect of a magnetic field, and three different regimes are identified according to its intensity. Linear chains of these dots are discussed as a function of the array parameters, resulting in bands of tunable gap and curvature. Some cases of particular interest are encountered, like overlap-assisted processes inducing a sign change in the renormalized mass or the existence of a regime of Frenkel excitons interacting through a dominant Förster transfer.

Light-matter interactions are further analyzed with the study of polaritons in hBN nanogranules. In the realm of Hamiltonian optics and by the application of the semiclassical Einstein-Brillouin-Keller and of Gutzwiller's approaches, we reproduce and explain the origin of mid-infrared resonances measured in an experiment. We find a clear physical picture to interpret them based on closed classical orbits with a common topology. Moreover, a method to predict intensity patterns in near-field measurements is devised and a numerical simulation proves its validity.

At last, the orbital magnetic susceptibilities of graphene and MoS_2 are calculated using multi-band tight-binding models. For graphene, our analy-

sis yields an extra $\sim 12\%$ diamagnetic contribution close to neutrality as a lattice effect of σ orbitals, and some diamagnetic peaks are identified with band crossings. For MoS_2, we discuss the diamagnetic wells in terms of the underlying Dirac-like gaps. The results reveal that a simple model of Dirac electrons with mass cannot succeed in a quantitative description due to the more complex structure of the Berry curvature. Other 2-band models that fit the band structure close to neutrality are also considered in this respect. Our analysis accounts for the contribution of each point of the Brillouin zone to the magnetic susceptibility, and helps to discern when geometrical effects take over the semiclassical description of the orbital magnetization.

Resumen

Esta tesis presenta varios estudios teóricos sobre tres materiales novedosos: grafeno, nitruro de boro hexagonal (hBN) y MoS_2. Los distintos trabajos están englobados bajo dos temas, a saber, las interacciones entre radiación y materia y la física semiclásica. El primero tiene como objeto describir los correspondientes modos colectivos, que son plasmones y polaritones, mientras que el segundo concierne la óptica de rayos no convencional y el estudio de la susceptibilidad magnética orbital.

En el caso del grafeno, se calcula la respuesta lineal corriente-corriente a temperatura y dopado finitos. Con respecto al canal transversal, se presenta una caracterización completa de los plasmones más allá de la aproximación local. Analizamos su rápido decaimiento con la temperatura, la sensibilidad a los medios dieléctricos del entorno y el máximo confinamiento que puede lograrse mediante disposiciones de varias capas. Además, la absorción de estructuras laminadas de una o dos capas se discute en función de la polarización y ángulo de incidencia de la luz.

También para grafeno, se estudian los puntos cuánticos de perfil de masas como un nuevo mecanismo para confinar portadores. Técnicas experimentales recientes que involucran un substrato de Ir permiten modular el *gap* espacialmente, lo que motiva nuestro trabajo teórico. Se lleva a cabo un análisis del espectro incluyendo el efecto de un campo magnético, y se identifican tres regímenes diferentes según su intensidad. En función de los parámetros de la red de puntos cuánticos, se analizan los espectros de cadenas lineales, obteniéndose bandas con *gaps* y curvaturas variables. Algunos casos de particular interés surgen entonces, como procesos asistidos por el solape de las funciones de onda, que inducen un cambio de signo en la masa renormalizada; o la existencia de un régimen de excitones de Frenkel que interaccionan a través de la dominante transferencia de Förster.

Las interacciones entre radiación y materia se analizan también para los polaritones en nanogranulos de hBN. En el contexto de la Óptica Hamiltoniana y a través de la aplicación de los formalismos semiclásicos de Einstein-Brillouin-Keller y de Gutzwiller, se reproducen las resonancias en el infrarrojo medio medidas en un experimento y se explica su origen. Encontramos una clara imagen física para interpretarlas, basada en las órbitas clásicas cerradas que comparten una misma topología. Además, se propone un método

para predecir los patrones de intensidad en medidas de campo cercano, cuya validez se prueba mediante una simulación numérica.

Por último, la susceptibilidad magnética orbital de grafeno y MoS_2 se calcula usando modelos de *tight-binding* multibanda. Para grafeno, nuestro análisis da una contribución diamagnética extra de un 12 % cerca del punto de neutralidad, consecuencia del efecto de red de los orbitales σ, y algunos picos diamagnéticos se identifican en términos de los *gaps* de Dirac subyacentes. Los resultados revelan que un modelo simple de electrones de Dirac masivos no responde a una descripción cuantitativa debido a una estructura algo más compleja de la curvatura de Berry. Otros modelos de dos bandas que se ajustan a la estructura de bandas cerca del punto de neutralidad también se tienen en cuenta a este respecto. Nuestro análisis desglosa la susceptibilidad magnética en la contribución de cada punto dentro de la zona de Brillouin, y ayuda a discernir cuándo los efectos geométricos dominan sobre la descripción semiclásica de la magnetización orbital.

Contents

Chapter 1

Introduction

Nowadays, condensed matter remains an active research field in physics. On the one hand, technological developments giving experimental access to the nanoscale and beyond, including material-production techniques and measurement tools like scanning tunneling microscopy or near-field probing, have brought significant advances. On the other hand, a plethora of theoretical models that manifest exotic phenomena of quantum field theory or present extraordinary electronic or optical properties have been realized in novel materials. A vast diversity of newly discovered or devised systems encoding rich physics are yet to be explored in this context.

The framework of this thesis lies on some of these novel materials, particularly regarding the characterization of their electronic, optical or magnetic properties. One of them is graphene, a 2D allotrope of carbon with a honeycomb lattice structure, which has received a lot of attention since its isolation through mechanical exfoliation a decade ago.[1] Its characteristic band structure close to half filling, showing an unusual linear dispersion, was first studied by Wallace[2] in the late 1940s. Interestingly, it was found that close to the Dirac cones, electrons behave as chiral and massless Dirac fermions, but with a speed $v_F \simeq 10^6\,\mathrm{m/s}$ and with the sublattice index playing the role of a spin. As a consequence, this material has emerged as a scenario that naturally manifests quantum electrodynamics (QED) even at room temperature.[3,4] Actually, distinctive phenomena like the Klein tunneling or the half-integer quantum Hall effect have been experimentally observed at ease,[5–7] as opposed to the difficulties encountered in high-energy physics.

An extensive study covering its transport, mechanical and optical properties has been performed these years.[4,8] The high mobility of the carriers of graphene together with its unprecedented flexibility, robustness and a good environmental stability stand out among its promising features. Particularly in the fields of photonics and optoelectronics, graphene has also emerged as an engaging prospect. In this respect, one can highlight the still debated minimum conductivity $\sigma \simeq 4e^2/h$ even when the carrier concentration tends to zero,[3] or its universal absorption constant.[8,9] Proposals exploiting these

properties, like solar cells, photodetectors, light-emitting devices or ultrafast lasers exemplify the wide range of applications.[10]

Nevertheless, several issues are yet to be overcome in order to play upon some of these extraordinary qualities. In this thesis, we will address one of particular relevance, namely the difficulty to confine carriers in graphene due to Klein tunneling.[4,11] Indeed, it is one of the main issues hampering the design of field-effect transistors and quantum dots out of this material. Although several solutions have been proposed, we devise a new one based on the induction of a mass profile. It was inspired by a recently developed experimental technique involving an Ir substrate, which in addition allows to engineer quantum-dot setups with nanometer accuracy.[12] Besides contributing to an extra confinement, the effect of magnetic fields in these systems results in a rich spectrum ranging from randomly distributed levels to a Landau structure, the former presenting a remarkable valley splitting of potential technological use. Moreover, as we will discuss below, the ability to tune interactions between the electron-hole pairs confined in the dots brings about engaging physics.

Another novel material analyzed in this thesis is MoS_2, a topological valley insulator which has attracted great attention together with other transition-metal dichalcogenides. The ability to exfoliate them into one layer of single-unit-cell thickness has renewed the interest in their study, nowadays focusing on 2D allotropes and Van der Waals heterostructures.[13,14] Importantly, due to the inversion-symmetry breaking, a band structure with two different valleys and a non-negligible spin-orbit coupling, there is a significant interplay between the spin and valley degrees of freedom. This is in stark contrast with the case of pristine graphene, for which they are degenerate and thus play a secondary role.

As a consequence, MoS_2 is deemed to be an ideal platform for the integration of valleytronics and spintronics.[15,16] Among its attractive features, one can highlight the intertwining between the spin and valley Hall effects;[17] its sizable band gap[18] that changes from indirect to direct when exfoliating the bulk into a single layer,[19] the latter lying in the visible frequency range and being suitable to the design of field-effect transistors; and the valley-dependent optical selection rules for a monolayer,[20,21] which is of potential use in optoelectronics.

At last and aiming more directly at nano-optics, part of this thesis focuses on hexagonal boron nitride (hBN). This material is an isomorph of graphite, with boron and nitrogen atoms respectively occupying the two sublattices of honeycomb planes stacked in the Bernal configuration. It is an insulating polar material well known as one of the best substrates for graphene, yielding considerably flat samples with high-quality electronic properties.[22,23] Moreover, it offers a mechanism to open a gap in graphene depending on the relative twist angle.[24,25]

However, it has been a matter of intense research by itself particularly

in the realm of nano-optics, not necessarily as a building block of a heterostructure. It turns out to be a natural hyperbolic material, namely a hybrid between a metal and a dielectric in terms of the propagation of electromagnetic modes. Conventional optics is not suitable for their description, which entails notable implications. The undamped propagation of near fields and a divergent density of states at several frequencies can be highlighted in this respect.[26,27]

Its production in multiple geometries and patterns and their experimental characterization are currently at reach, which makes it stand out as a good prospect in the mid infrared,[28,29] actually outclassing other ad hoc nanoscale-designed metamaterials.[30] Among the applications, summarized in the corresponding chapter of this work, the accomplishment of partial hyperlensing, namely the achievement of an almost unlimited spatial resolution, has been one of the most impressive.[31]

More precisely within the broad description of these materials, one of the topics assembling the studies presented in this thesis is light-matter interactions. They are the underlying cause of diverse collective phenomena that manifest near or beyond the diffraction limit of light, a key issue in optics. The state-of-the-art research activity on this topic mainly deals with the improvement of radiation confinement and amplification, and the achievement of an extraordinary spatial resolution, by means of tailoring these novel materials at the nanoscale and of probing them with near fields.

Plasmons are a distinguished example of the revolutionary phenomena encountered in this context.[32] The existence of these collective modes, arising due to electron-electron interactions, was pointed out for the first time in metal-dielectric interfaces.[33,34] Although achieving the aforementioned confinement into subwavelength dimensions and a great enhancement of near fields, the great losses associated to metals emerged as a major problem to be tackled.

These modes can be subject to the existence of an interface, and considering their fast decay away from it, practically live in two dimensions. For this reason, some of the aforementioned 2D materials emerged as a potential alternative, with the additional interest brought on by the peculiar behavior of their carriers.[35] Graphene soon became an archetype in modern plasmonics, showing greater confinement, larger propagation distances and more tunability within the THz regime via, e.g., electric gating.[36–39]

Part of this thesis is devoted to the characterization of transverse plasmons in this material. They are associated to oscillating transverse currents rather than to an oscillating density of electrons, or equivalently to magnetic rather than electric phenomena. Much less studied than their longitudinal counterparts, we provide a thorough discussion of their behavior in terms of temperature, doping, confinement and detection, contributing to a more comprehensive understanding of this phenomenon.

Interactions in this material will also be analyzed in a different setup,

namely engineered lattices of the aforementioned quantum dots. Being able to tune the spectrum density and also the intensity of the electromagnetic interactions between the dipoles of adjacent dots, different dynamic regimes can be induced. Actually, certain design parameters entail the existence of long-lived Frenkel excitons that interact through the dominant Förster term, yielding an effective bosonic tight-binding Hamiltonian. This conclusion opens the remarkable possibility to observe Bose-Einstein condensates in this scenario.

Another noteworthy collective mode, the so-called polaritons, results from the interaction of radiation with the phonons of a polar material. Although not necessarily bound to a surface, they are also of high subwavelength nature, presenting a great deal of confinement and extremely low losses.[29]

Due to the high anisotropy of its structure and the fact that its phonon frequencies lie in the infrared spectrum, hBN presents itself as an exciting system for the study of interactions between matter and near fields.[40,41] Moreover, recent experiments have reported striking results that point at its hyperbolic modes as the underlying cause, as well as pave the way to the design and implementation of optoelectronic devices.[26,29,42] Motivated by these measurements, in this thesis we analyze these excitations in the realm of non-conventional ray optics, managing to interpret the highly confined resonances and devising a way to predict the intensity patterns in near-field experiments. The heart of this approach lies in the intermediate regime in between the wavelike behavior and particle dynamics.

The bridge linking waves and rays, strongly related to semiclassical physics, is not exclusive to that part of the thesis. The passage from wave to particle dynamics, or between the quantum to the classical worlds, is the second assembling point that links some of the presented works. In particular, for the modern theory of orbital magnetism,[43–46] discussed for graphene and MoS_2, this issue is of fundamental relevance: what previously could be roughly understood in terms of classical electrons with an effective mass or isolated atoms has turned out to depend on a deeper quantum and geometrical nature,[47,48] which in turn manifests the rich underlying physics of these novel materials. Sometimes, however, a semiclassical behavior prevails. We will discuss these considerations also regarding effective models, contributing to a more thorough understanding of the orbital magnetic susceptibility.

This thesis is organized as follows. The second chapter is devoted to plasmons in graphene, particularly regarding the transverse channel, the influence of temperature, doping and the geometry of layered structures, as well as the maximum radiation confinement at reach. Also for graphene, the third chapter studies the spectrum of mass-profile quantum dots including the presence of magnetic fields, discusses interactions between adjacent dipole moments and points out the existence of an excitonic regime for certain array parameters. The fourth chapter focuses on the hyperbolic modes

in hBN and their interaction with near-field radiation, which explains the results of recent experiments and predicts field patterns in possible forthcoming measurements. At last, the fifth chapter deals with the magnetic response of graphene and MoS_2 from the modern perspective of orbital magnetism, considering multi-band spectra and discussing also the accuracy of effective models near the neutrality point. A brief conclusion together with several appendices close this work.

Chapter 2

Transverse current response of graphene at finite T, plasmons and absorption

2.1 Introduction

This chapter aims at a comprehensive characterization of the current-current response of graphene, with particular emphasis on the transverse channel. The study is performed by means of the linear-response theory, whose basic formalism is outlined in Appx. A and is discussed in Secs. 2.1.1 and 2.1.2 regarding the rise of electronic collective excitations, so-called plasmons.

In this context, Sec. 2.2 presents the linear transverse current-current response functions for graphene at finite temperature and chemical potential, which is the main result of this chapter. Within the Random Phase Approximation, we discuss in Secs. 2.3 and 2.4 the general aspects of transverse plasmons beyond the local response such as their dependence on temperature and on the surrounding dielectric media. Particular attention is paid to confinement and its enhancement by means of homogeneous dielectric embeddings or optical cavities. Finally, in Sec. 2.5 we discuss the absorption of electromagnetic radiation in single and double-layer systems.

This work addresses many unanswered questions concerning transverse plasmons that were however widely known for their longitudinal counterparts. Both of them are compared in several aspects throughout this chapter. Our approach manages to unravel remarkable differences that emerge as limitations to experimentally observe the former or to find potential applications.

2.1.1 Plasmons

During the last years, plasmonics has become a celebrated field to which deep and intense research is being targeted. The term plasmon alludes to

a collective harmonic movement of electrons[33] entailing equally oscillating electromagnetic fields, and was born in the context of studying losses of fast electrons when moving through metallic foils.[34,49] This concept also emerges as the existence of electromagnetic modes at the interface between a metal and a dielectric.[50,51]

As is discussed in Appx. A.4 and A.5, the interacting current-current response function is a tool that allows to characterize these excitations. Interactions can be included via the Random Phase Approximation (RPA), and the decomposition in the longitudinal and transverse components detailed therein accounts for the existence of two distinct and independent kinds of plasmons. These correspond to Transverse Magnetic (TM) and Transverse Electric (TE) modes, respectively.[32] Longitudinal plasmons have received most of the attention, because they are associated to the density response (recall the equivalence between χ_L and $\chi_{\rho\rho}$) and thus to charge accumulation, $\langle\rho\rangle_1(\mathbf{q},\omega) \neq 0$. Transverse plasmons, on the contrary, are associated to oscillating transverse currents, $\nabla \cdot \mathbf{j} = 0$ and $\langle j_T\rangle_1(\mathbf{q},\omega) \neq 0$, but preserve an homogeneous density charge.

The interest in their study lies on both the theoretical and practical sides. On the one hand, they manifest many-body effects between electrons associated to the long-range Coulomb interaction; on the other, longitudinal plasmons show striking features, like the possibility of confining to two dimensions and amplifying the associated electromagnetic fields.[32,52] Various applications in cutting-edge electronics and optoelectronics play upon this peculiarity[53–57] and enforce the will to extend this exploration to a wider range of systems. As we proceed to discuss, graphene is one particularly promising example. The aim of this chapter is to focus on this novel material, mainly regarding the less explored transverse channel.

2.1.2 Plasmons in graphene

The existence and behavior of plasmons in graphene stem from the interaction of its electrons with electromagnetic radiation. Some main results covering this aspect have been outlined in Ref. [8]. A constant value for the real part of the conductivity above twice the Fermi energy, i.e., an absorption value equal to 2.3% dependent only on universal constants for a wide range of frequencies, deserves to be highlighted.[9,58] At the same time, several issues still demand further research and suggest that this topic is far from being exhausted. For example, the real part of the conductivity shows a plateau between the intra and interband energy regions[59] whose numerical value cannot yet be accounted for theoretically.[60]

Graphene is thus a promising candidate to further research on plasmons[1,10,36,38,39] and has actually attracted a great deal of attention regarding the longitudinal channel. The dispersion relation of density plasmons, determined by the divergence of the loss function, is reproduced in Fig.

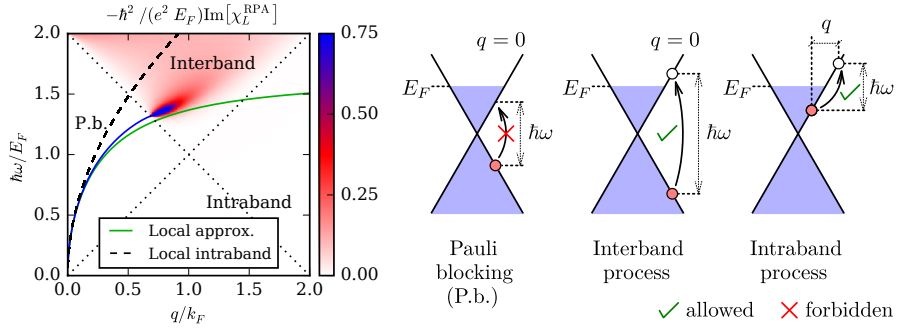

Figure 2.1: Density plot of the longitudinal loss function, cf. Appx. A.5. The blue line in the Pauli-blocking (P.b.) region plots the divergence of $\mathrm{Im}\left[\chi_L^{\mathrm{RPA}}\right]$ —namely the dispersion relation of plasmons—. So do the green and dashed black curves, which correspond to the local approximation including and neglecting interband processes, respectively. The former is significantly red shifted with respect to the latter, giving a much better approximation to the exact solution. The smearing over the zone where electron-hole excitations are available results in damping. On the right, the sketches around the Dirac point illustrate this mechanism, as well as its absence in the Pauli-blocking regime.

2.1. Two relevant features, particularly profitable for practical purposes, stand out by its mere inspection. First of all, within the validity of the considered model, plasmons are undamped for $\hbar\omega/E_F \lesssim 1.3$. This is due to the unavailability of electron-hole-excitation processes liable to quench the plasmonic excitation. Secondly, the significant separation of the dispersion-relation curve away from the light cone (which is pinned to the frequency axis in the plot) entails the great spatial confinement of electromagnetic fields mentioned in Sec. 2.1.1.

Importantly, the experimental observation of density plasmons is currently at reach[61,62] and several fundamental studies[63,64] have already been carried out considering the influence of temperature,[65,66] lattice effects,[67,68] band gap,[69] electron-electron interactions[70] or magnetic fields.[71] Also new plasmon-related phenomena have been discussed in double-layer structures, where Coulomb interaction between two graphene layers in the strong light matter coupling regime reveals to be the vehicle that tunnels photons through an otherwise forbidden transmission.[72]

On the other hand, not so much has been clarified about transverse plasmons in graphene.[73–77] Ref. [73] first spots their existence for the simplest case, namely a suspended layer at zero temperature and considering the local approximation ($q = 0$) for the current-current response function. However, it was not till very recently that their experimental observation was reported.[78]

Due to their transverse nature, the dispersion relation is closely pinned to the light cone and they are confined to energies between 1.667 and twice the Fermi energy (for larger energies, they are strongly damped), see Fig. 2.2 (left).[73] In subsequent sections, we aim at discussing this transverse light-matter coupling in more detail regarding the influence exerted by finite temperature, the possibility of inducing transverse plasmons in an undoped graphene sheet, the circumstances that demand the discard of the local approximation for the response function, the changes induced by modifying the dielectric surroundings, the highest spatial confinement within reach or their behavior when sheets are embedded inside an optical cavity.

Accordingly, the results of the remaining chapter are organized as follows. In Sec. 2.2, we calculate the current-current response function at finite temperature and doping for both the longitudinal and transverse channels. Sec. 2.3 then analyzes the questions mentioned above: i) effects related to finite temperature, ii) effects related to various dielectric media and the necessity of going beyond the local response, and iii) effects related to placing graphene inside a vertical cavity. This analysis is performed mainly pursuing the enhancement of confinement in the transverse channel. Sec. 2.5 complements this discussion by calculating the transmittance of electromagnetic radiation for s and p polarizations for a single and double layer structure, and Sec. 2.6 closes with a summary and outlook.

2.2 Current-current response function of graphene at finite temperature

In this section, we perform the calculation of the current-current response function for a graphene monolayer at finite temperature and doping. We will deal with the effective model with Hamiltonian $H_K = \hbar v_F \sigma \cdot \mathbf{k}$ and $H_{K'} = \hbar v_F \sigma^* \cdot \mathbf{k}$ for $\mathbf{k}$ around K and K' points, respectively. Here, σ is the isospin operator $\sigma = (\sigma_x, \sigma_y)$ containing the Pauli matrices and $v_F \simeq 10^6$ m/s is the Fermi velocity. Due to its rotational invariance, $\chi_{\mathbf{jj}}(\mathbf{q}, \omega)$ will be determined without loss of generality by the two scalars $\chi_{j_x j_x}(q\hat{x}, \omega)$ and $\chi_{j_x j_x}(q\hat{y}, \omega)$, which correspond to $\chi_L(q, \omega)$ and $\chi_T(q, \omega)$, respectively. $\hat{x}$ and $\hat{y}$ denote here unit vectors, and homogeneity in space is assumed.

$\chi_{j_x j_x}(\mathbf{q}, \omega)$ for graphene can be calculated with Eq. (A.11) and the Fourier transform of the paramagnetic-current operator,[79]

$$\hat{\mathbf{j}}_{\mathbf{q}} = e v_F \sum_{\mathbf{k},\alpha,\beta} \hat{\psi}^{\dagger}_{\mathbf{k}-\mathbf{q},\alpha} \sigma_{\alpha\beta} \hat{\psi}_{\mathbf{k},\beta} \,. \tag{2.1}$$

$\hat{\psi}^{(\dagger)}_{\mathbf{k},\alpha}$ is the annihilation (creation) operator of an electron in the α sublattice with momentum $\mathbf{k}$ and e is the electron charge. It is obvious then that

$$\chi_{\mathbf{jj}}(\mathbf{q}, \omega) = e^2 v_F^2 \chi_{\sigma\sigma}(\mathbf{q}, \omega) \,. \tag{2.2}$$

Since the isospin-isospin response function only differs in a multiplicative factor with respect to the current-current one, we will deal from now on with $\chi_{\sigma_x\sigma_x}(\mathbf{q},\omega)$. The Lehmann representation yields[79]

$$\chi^{(0)}_{\sigma_x\sigma_x}(\mathbf{q},\omega) = \frac{1}{S}\lim_{\epsilon\to 0^+}\sum_{\mathbf{k}}\sum_{\lambda\lambda'}\frac{n^{(0)}_{\mathbf{k},\lambda}-n^{(0)}_{\mathbf{k}+\mathbf{q},\lambda'}}{\hbar\omega+\epsilon_{\mathbf{k},\lambda}-\epsilon_{\mathbf{k}+\mathbf{q},\lambda'}+i\epsilon}\times \\ |\langle\chi_\lambda(\mathbf{k})|\sigma_x|\chi_{\lambda'}(\mathbf{k}+\mathbf{q})\rangle|^2\,, \tag{2.3}$$

for the wavefunctions

$$\chi_\lambda(\mathbf{k}) = \frac{1}{\sqrt{2}}\begin{pmatrix}1\\ \lambda e^{i\phi_{\mathbf{k}}}\end{pmatrix} \tag{2.4}$$

with eigenvalues $\epsilon_{\mathbf{k},\lambda}$ and the non-interacting Fermi statistics $n^{(0)}_{\mathbf{k},\lambda}$. $\lambda = +1(-1)$ corresponds to the upper (lower) band and $\phi_{\mathbf{k}}$ is the angle between $\hat{x}$ and $\mathbf{k}$.

It is also interesting to mention that although the density-density and the longitudinal total current-current response functions are related by Eq. (A.18), when considering the paramagnetic current instead, the analogous equation turns out to be[79]

$$\chi_{\rho\rho}(q,\omega) = \frac{ev_Fq}{\omega^2}\langle[\sigma^x_q,\rho_{-q}]\rangle + \frac{q^2}{\omega^2}\chi_{j_xj_x}(q\hat{x},\omega)\,. \tag{2.5}$$

Counting on all previous considerations, we can write the isospin-isospin bare response functions as follows, with $\beta = 1$ ($\beta = -1$) for the longitudinal (transverse) channel (that is, we could write $\mathbf{q} = \frac{q}{2}(|\beta+1|\hat{x} + |\beta-1|\hat{y})$ for $\beta = \{-1,+1\}$ in the left hand side of the formulas below):

$$\mathrm{Re}\left[\chi^{(0)}_{\sigma_x\sigma_x}(\mathbf{q},\omega,T,\mu)\right] = -\frac{E_{\max}}{4\pi\hbar^2v_F^2}+ \\ (-1)^{\frac{\beta+1}{2}}\frac{g}{4\pi\hbar v_F^2}\sum_{\alpha=\pm}\left[\frac{\omega^2}{q^2}\frac{2k_BT\log\left[1+\exp\left(\frac{\alpha\mu}{k_BT}\right)\right]}{\hbar v_F^2}+\right. \\ +\Theta(\omega-v_Fq)f_\beta(\omega,v_Fq)\left[G^{(\alpha,\beta)}_+(q,\omega,T,\mu)-G^{(\alpha,\beta)}_-(q,\omega,T,\mu)\right]+ \\ \left.+\Theta(v_Fq-\omega)f_\beta(\omega,v_Fq)\left[\frac{\pi}{2}\Theta(-\alpha)-H^{(\alpha,\beta)}(q,\omega,T,\mu)\right]\right], \tag{2.6}$$

$$\mathrm{Im}\left[\chi^{(0)}_{\sigma_x\sigma_x}(\mathbf{q},\omega,T,\mu)\right] = \frac{g}{4\pi\hbar v_F^2}\sum_{\alpha=\pm}\left[\Theta(v_Fq-\omega)f_\beta(\omega,v_Fq)\times\right. \\ \left[G^{(\alpha,\beta)}_+(q,\omega,T,\mu)-G^{(\alpha,\beta)}_-(q,\omega,T,\mu)\right]+ \\ \left.+\Theta(\omega-v_Fq)f_\beta(\omega,v_Fq)\left[-\frac{\pi}{2}\Theta(-\alpha)+H^{(\alpha,\beta)}(q,\omega,T,\mu)\right]\right], \tag{2.7}$$

with

$$f_\beta(\omega, v_F q) = \frac{\omega}{2}\left|1 - \frac{v_F^2 q^2}{\omega^2}\right|^{-\beta/2},$$

$$G_\pm^{(\alpha,\beta)}(q,\omega,T,\mu) = \int_1^\infty \frac{u\left[1-\frac{1}{u^2}\right]^{\beta/2}}{\exp\left[\frac{\hbar|v_F q u \pm \omega| - 2\alpha\mu}{2k_B T}\right]+1} du\,,$$

$$H^{(\alpha,\beta)}(q,\omega,T,\mu) = \int_{-1}^1 \frac{|u|\left[\frac{1}{u^2}-1\right]^{\beta/2}}{\exp\left[\frac{\hbar|v_F q u + \omega| - 2\alpha\mu}{2k_B T}\right]+1} du\,.$$

$E_{\max}$ is an ultraviolet cutoff which is canceled by the diamagnetic contribution, as required by gauge invariance.[79] We include the spin and valley degeneracies as $g = g_s g_v$. Given the electronic density n, the chemical potential is determined by

$$\int_{-\infty}^{\infty} d\epsilon\ \nu(\epsilon)\left[n_F(\epsilon) - \Theta(-\epsilon)\right] = n\,, \tag{2.8}$$

where the density of states is $\nu(\epsilon) = g|\epsilon|/(2\pi\hbar^2 v_F^2)$.

These are the main analytical results of this chapter. They generalize others as the ones given by Refs. [79,80], whose validity is restricted to $T = 0$, or those of Ref. [65], where only the longitudinal channel (or, equivalently, the density-density response) is taken into account.

2.3 Transverse response and plasmons

With the bare current-current response given by Eqs. (2.6) and (2.7) and the discussion of Appx. A.5, which captures electron-electron interactions, plasmons can be thoroughly featured. Regarding the transverse channel, the divergence of the denominator of Eq. (A.27) was already discussed by Ref. [73], demonstrating the existence of transverse electric (TE) modes in graphene. However, its conclusions are restricted to zero temperature, suspended graphene in vacuum and the local ($q = 0$) approximation of the conductivity. Throughout this section, we investigate what happens if those simplifications are discarded. In the following, it is our aim to offer a better understanding of TE modes in graphene by means of our more general result for the current-current response functions.

2.3.1 Transverse plasmons and temperature

The loss function

$$S(q,\omega) = -\mathrm{Im}\left[\chi^{\mathrm{RPA}}_{j_x j_x}(\mathbf{q},\omega)\right], \tag{2.9}$$

is a suitable tool to inquire about the existence and features of plasmons, as was discussed in Sec. 2.1.1. Aside from reproducing the singularities of

Eq. (A.27) at $T = 0$, it gives information about how they broaden due to damping (coming in our case from electron-hole excitations, see the outlines in Fig. 2.1) when $T > 0$ or whenever $\mathrm{Im}\left[\chi^{(0)}_{j_x j_x}(\mathbf{q}, \omega)\right] \neq 0$.

It is already known that density plasmons hold (although, of course, damped) at room temperature[81,82] or higher[66] ($T \sim T_F$) in the sense that the loss function is not excessively smeared around the singularity present at $T = 0$.

However, transverse plasmons behave in a different manner regarding this aspect. To demonstrate so, let us focus on Figs. 2.2 and 2.3. There, we represent the dispersion relation of transverse plasmons at $T = 0$ with a solid line,* whereas the colors correspond to the values of the loss function at the specified temperature. Due to the proximity of the curves to the light cone, it would be difficult to observe them in a plot of $\hbar\omega/E_F$ versus q/k_F. Instead, it is convenient to represent the difference $cq - \omega$ in units of $E_F/\hbar$ versus the wave vector q in units of $v_F k_F/c$.

We can see that at very low temperatures, the loss function still suggests the structure of the dispersion relation of transverse plasmons: they are so far well defined. However, rising T to $0.1T_F$ implies that no trace of them is preserved. This is due to the vicinity of the plasmon dispersion to the region of interband transition and also due to the small spectral weight of the transverse plasmon suppressed by $1/\tilde{c}^2$ with $\tilde{c} = c/v_F \approx 300$. The effect of frequency shifting as a consequence of the influence of T is also worthwhile being mentioned.[66] Not only does temperature determine to which extent longitudinal plasmons are damped, but also displaces the dispersion relation towards higher energies. From Figs. 2.2 and 2.3, an analogous result can be inferred for the transverse channel. Nevertheless, here we observe a red instead of a blue shift; the transverse plasmon thus becomes more localized but finally fades out.

2.3.2 Plasmons at zero doping

Another interesting consideration involving temperature is its ability to induce plasmonic excitations at zero doping. When E_F and T equal 0, neither electric nor magnetic modes can be present in a graphene layer. However, finite temperature involves thermally activated electron-hole excitations, allowing longitudinal (slightly damped) plasmons to appear.[81] In fact, the case of $E_F = 0$ and $T > 0$ (T being sufficiently low) can be shown to be equivalent to doped graphene at $T = 0$ with the Fermi energy $E_T \equiv 2 \ln 2 k_B T$.[82] In other words, the role of temperature is equivalent to inducing a nonzero value of doping.

*$\mathrm{Im}\left[\chi^{(0)}_{j_x j_x}(q\hat{y}, \omega)\right]$ is set equal to 0 for $\omega > E_F/\hbar(2 - q/k_F)$, i.e. outside the Pauli-blocking zone, where the loss function is really smeared around the solid line plotted because of electron-hole excitations.

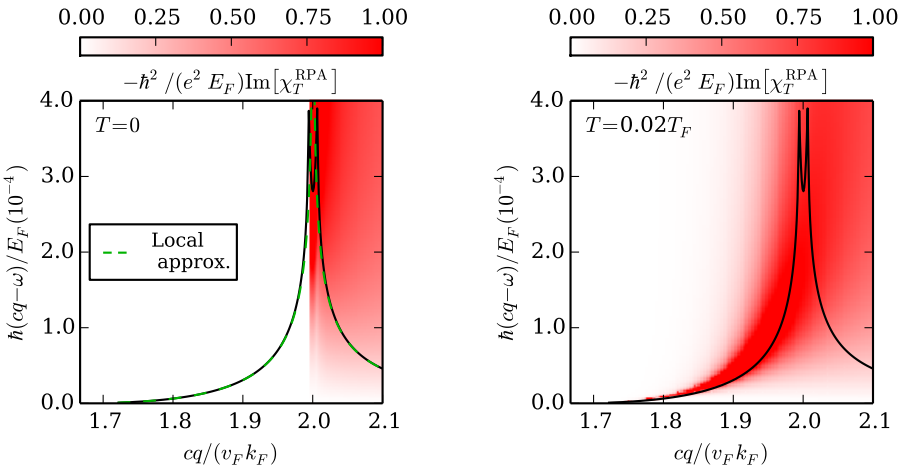

Figure 2.2: The black lines plot the dispersion relation for transverse plasmons at $T = 0$ (setting $\mathrm{Im}\left[\chi^{(0)}_{j_x j_x}\right] = 0$), and so does the dashed green line but for the local approximation. The value of the transverse loss function for the given temperatures is represented by the density plots. $T = 0.02T_F$ roughly corresponds to $27K$ for $E_F = 0.12$eV.

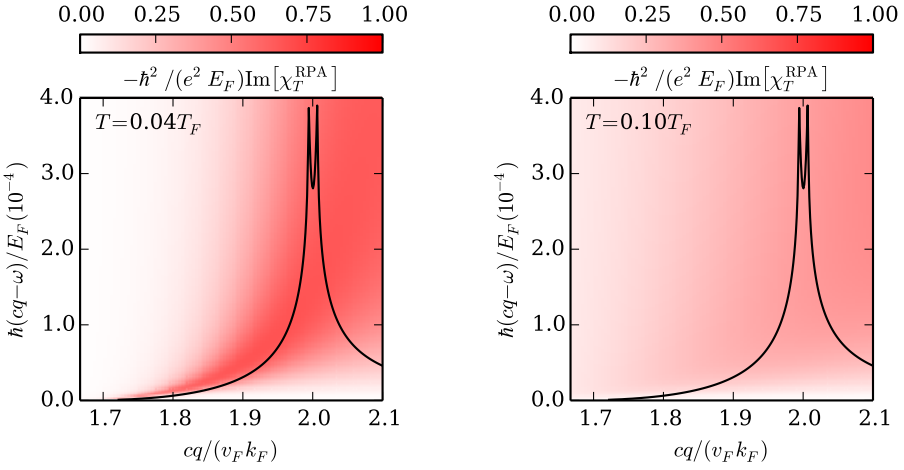

Figure 2.3: Same as in Fig. 2.2. $T = 0.04T_F$ and $T = 0.1T_F$ roughly correspond to $53K$ and $134K$, respectively, for $E_F = 0.12$eV. Whereas in the first case the dispersion relation structure is still recognizable, in the last one it is completely lost.

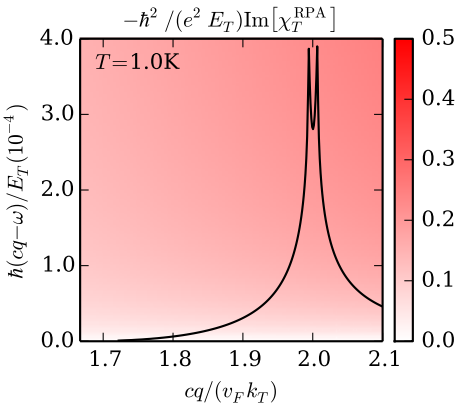

Figure 2.4: Same as in Fig. 2.2, but for $E_F = 0$ and $T = 1K$. The solid line corresponds to $k_T = E_T/(\hbar v_F)$ and $T = 0$, with $E_T \equiv 2\ln 2 k_B T$. The loss function does not show any trace of transverse plasmons.

Thus basically two forces compete in the context of this mechanism to make plasmons spring up: the excitation of carriers being favorable to their emergence and the increase of damping quenching them. Whereas in the longitudinal case there are well-defined oscillations, we find that for transverse plasmons they are completely washed out. We can understand this by comparing the energy scale set by the temperature T with the energy scale given by E_T:

$$k_B T/E_T = 1/(2\ln 2) \simeq 0.7\ . \tag{2.10}$$

Since already for $T = 0.1T_F$ there is no clear maximum in the loss function (see Fig. 2.3), the scale set by Eq. (2.10) seems too high to induce transverse plasmons at zero doping.

Fig. 2.4 confirms this intuition: the loss function for $T = 1K$ is completely diluted and does not reproduce the plasmon dispersion relation respective to $T = 0$ and a nonzero doping given by E_T. Lowering the temperature even more does not involve any change, which can be expected since Eq. (2.10) is a scale-invariant universal result. Thus, transverse plasmons cannot be found at zero doping, in contrast with density plasmons.

2.4 Influence of dielectric media

Longitudinal plasmons change their dispersion relation when graphene sheets (e.g. monolayer and double layer systems) are embedded between different dielectrics.[66] However, transverse plasmons do not behave similarly even in the simplest case, that is, a single sheet lying on a substrate. They exhibit an extreme sensibility to a slight difference in the refractive index of the

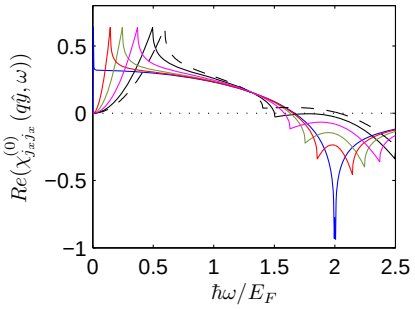

Figure 2.5: Re $\left(\chi^{(0)}_{j_x j_x}(q\hat{y},\omega)\right)$ at $T=0$ for different values of q/k_F: $5\cdot 10^{-3}$ (blue), 0.15 (red), 0.25 (green), 0.37 (magenta), 0.5 (solid black) and 0.6 (dashed).

two surrounding media to the extent of vanishing for $|n_2 - n_1| \sim 10^{-7}$ at room temperature.[83] This is due to the fact that the dispersion relation of transverse plasmons is extremely pinned to the light cone, such that when two different light cones exist and are sufficiently separated, they rapidly vanish.

Thus to focus on transverse plasmons and inquire about how the dispersion relation can substantially change due to their dielectric surroundings (permittivity and permeability), we will keep the vicinity of the graphene layer homogeneous with the same refractive index n. Within this constraint, we can analyze the consequences of modifying n.

2.4.1 Influence of the refractive index

Increasing the refractive index n decreases the speed of light, and as a consequence, the light cone is shifted to greater values of q for a fixed energy $\hbar\omega$. Since the plasmon relation must lie in the evanescent region, where $\omega < cq/n$, the current-current response $\chi^{(0)}_{j_x j_x}(q\hat{y},\omega)$ involved in that situation must be evaluated at larger q. As we mentioned before, previous discussions of the dispersion relation as the one in Ref. [73] would not be valid for high enough values of n, since they are only based on the local response ($q=0$). The relevance of this dependence is shown in Fig. 2.5, where the real part of the transverse current response is shown as a function of the energy for $q/k_F \sim 0 - 0.6$. The remarkable differences between curves imply significant changes in $\omega(q)$. Thus, Eqs. (2.6) and (2.7) allow to characterize transverse plasmons for high values of the refractive index.

Some results are shown in Fig. 2.6, where we focus on undamped plasmons at $T=0$. They can be compared to the solid black line of Figs. 2.2-2.4, respective to $\epsilon\mu = 1$. It is interesting to notice that, as we increase

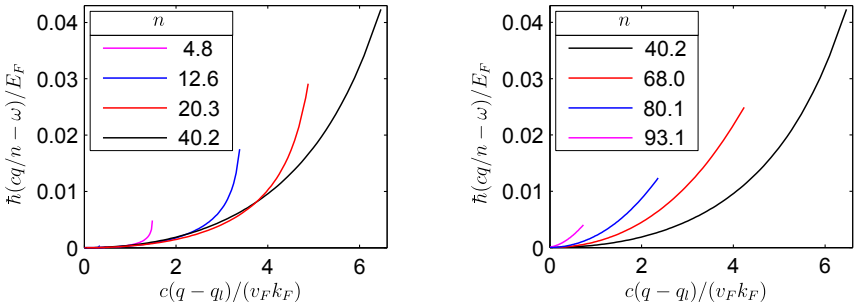

Figure 2.6: Dispersion relation of transverse plasmons for different refractive index n of the homogeneous dielectric medium embedding graphene. We only show the undamped region at $T = 0$. Curves are normalized to $q_l = n\omega_l/c$ with ω_l the lowest frequency for which transverse plasmons appear.

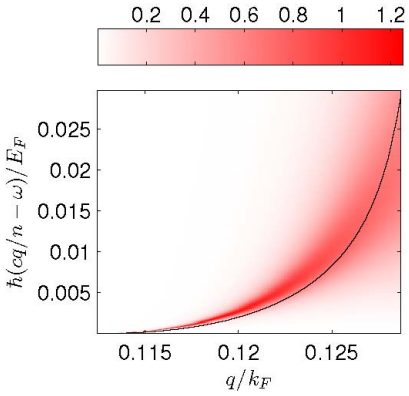

Figure 2.7: Same as Fig. 2.2, but for $T = 0.02T_F$ and $n = 20.3$. The loss function indicates the presence of damped transverse plasmons.

n starting from $n = 1$, the highest value of the curves moves further away from the light cone (left hand side of Fig. 2.6). But if we keep up increasing n, it turns back (right hand side of Fig. 2.6). Therefore, there is a maximal separation of the dispersion relation from the light cone which determines the fastest decay possible of the fields away from the graphene sheet.[66] The confinement of transverse plasmons can thus be increased by a factor of 10^2 by embedding the layer within a dielectric with $n \simeq 40$.

Regarding an experimental realization, large values of the refractive index could be provided by topological insulators at certain frequencies, ranging from $\epsilon \simeq 100$ at 0 THz to $\epsilon \simeq 250$ at 2 THz.[84] However, usual values of the Fermi energy around 0.5 eV would be too large to match those frequencies. A gate voltage could be applied to overcome this issue.

Regarding now the influence of temperature, there are no substantial

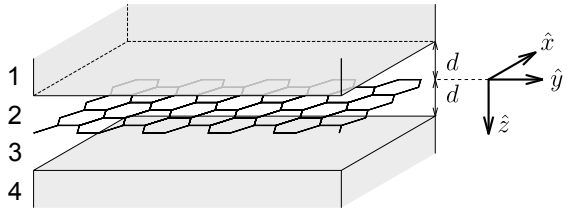

Figure 2.8: Schematic view of the cavity with graphene suspended in vacuum. Media 1 and 4 are semi infinite dielectrics/superconductors.

differences with respect to the case $\epsilon\mu = 1$ (previous section). Fig. 2.7 plots the loss function, which allows to see how at low temperatures the structure of the dispersion relation of plasmons is maintained. Once again, for $T > 0.1T_F$, it is completely diluted. Following the reasoning presented in the discussion of Eq. (2.10), neither would it be possible to have transverse plasmons for $E_F = 0$ induced by a finite T.

2.4.2 Influence of an optical cavity

Density plasmons are an excellent way of enclosing radiation in small regions. These dimensions just depend on the separation of the dispersion relation from the light cone: the decay length can be written as $\lambda = 2\pi/q'$, with $q' = \sqrt{q^2 - (n\omega/c)^2}$.[66] For energies of the order of $E_F/\hbar$, we can neglect retardation effects ($q' \simeq q$), yielding $\lambda \sim 2\pi/k_F$ and decay lengths of the order of 10 nm.

However, once again the situation drastically changes when considering the transverse channel. The proximity to the light cone implies that q' (even its maximum value, which can be estimated from Fig. 2.6) is now much smaller than that of its longitudinal counterpart. For suspended graphene, for example, we find a minimum value for undamped plasmons of $\lambda \sim 10^{-4}$ m. It is our aim to address the question of to which extent dodging this limitation is possible and whether confinement can be achieved by relying on a multilayer system.

Let us thus consider a single sheet of graphene embedded between four dielectrics (Fig. 2.8). For the sake of simplicity, we will set $\mu_1 = \mu_4 \to 0$ and $\mu_2 = \mu_3 = 1$, but keep the velocity of light constant and equal within the whole sample. This makes media 1 and 4 impenetrable by s-polarized electromagnetic waves and one might expect to force a faster decay of the potential vector $\mathbf{A}$ in the z direction.

To analyze this problem, we make the ansatz

$$\mathbf{A}_j(\mathbf{r},t) = M_j\hat{y}\exp\left[-q'z + i\left(qx - \omega t\right)\right] + N_j\hat{y}\exp\left[q'z + i\left(qx - \omega t\right)\right] \tag{2.11}$$

for every medium j, setting $M_1 = N_1 = M_4 = N_4 = 0$, and apply Maxwell equations at every interface. The transverse current-current response of graphene arises when attending to the frontier between dielectrics 2 and 3 (vacuum in our case), as well as RPA turns up when writing the surface current as[85] $\mathbf{j}(\mathbf{q},\omega) = \chi^{(0)}_{\mathbf{jj}}(\mathbf{q},\omega)\mathbf{A}(\mathbf{q},\omega)$ —which is equivalent to $\mathbf{j}(\mathbf{q},\omega) = \chi^{\mathrm{RPA}}_{\mathbf{jj}}(\mathbf{q},\omega)\mathbf{A}^{\mathrm{ext}}(\mathbf{q},\omega)$—. The resulting system of linear equations for M_j, N_j with $j = 2, 3$ will have a nontrivial solution only when its determinant is zero ($d > 0$):

$$2q' + \mu_0 \chi^{(0)}_{j_x j_x}(q\hat{y},\omega)\tanh(dq') = 0\,. \tag{2.12}$$

In that case,

$$N_2 = M_3 = -e^{2dq'}M_2\,,\ N_3 = M_2\,, \tag{2.13}$$

where M_2 is related to the incident field amplitude.

Let us now define the scale for the decay length. Denoting q'_p as the retarded wave vector which is most separated from the light cone and thus related to the maxima in Fig. 2.6, we can define $\lambda = 2\pi/q'_p$ as the length scale within which the transverse plasmon will be confined. Solving Eq. (2.12) numerically, we find a solution only for a layer separation $d > 0.15\lambda$. Thus, transverse plasmons in suspended graphene can be maximally confined to length scales of the order of 10^{-5} m, still much larger than those of the longitudinal channel. Relaxing the boundary conditions to other values does not significantly change these conclusions.

For short enough distances, it can be seen that the decay in the perpendicular direction to the frontiers differs quite a lot from being exponential, rather becoming practically linear. The plot for several values of d appears in Fig. 2.9, closing our discussion about transverse plasmons regarding the spatial decay of the electromagnetic fields attached to them.

To sum up, this section has mainly remarked the disparity between longitudinal and transverse plasmons as for confinement in the outskirts of the sheet, being the latter significantly more spread in space. This emerges from the nature underlying their dispersion relation (namely its proximity to the light cone) and can be hardly eluded even with the aid of setups like the one with impenetrable dielectrics shown in Fig. 2.8.

2.5 Absorption in single and double layer systems

In the previous sections, we have highlighted some aspects concerning the evanescent spectrum. Here, we will also cover some others related to the propagating modes, i.e., the absorption of s- and p-polarized light by a single and double layer graphene structure.

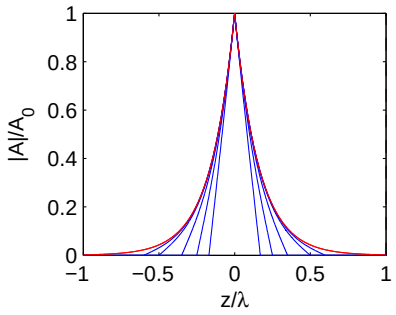

Figure 2.9: Modulus of the confined vector field of transverse plasmons for graphene in a cavity. Blue curves correspond to d/λ equal to 0.17, 0.25, 0.35, 0.5 and 0.6 (starting from the inner curve). For $d \leq 0.15\lambda$, no confined modes exist. Red curve: graphene in free space (media 1 and 4 absent). The length scale is given by $\lambda = 2.65 \cdot 10^{-4}$ m.

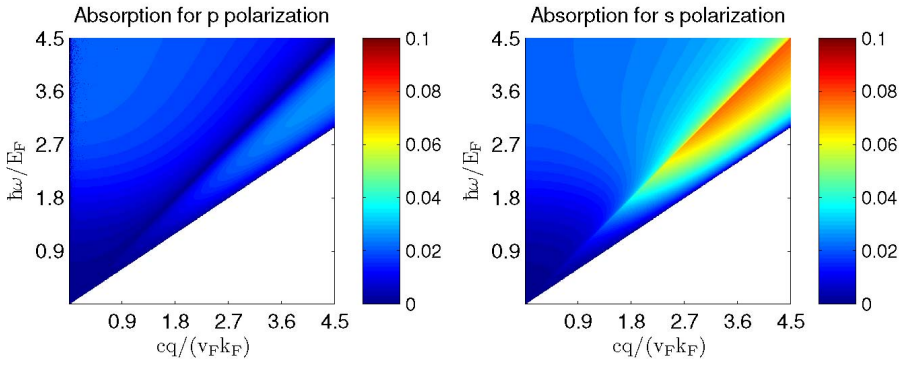

Figure 2.10: Absorption for graphene on a substrate with $\mu = 1$ and $n = 1.5$ for p- and s-polarized light at $T = 300K$. Incidence occurs from the substrate such that there is a critical angle for total reflection.

2.5.1 Single-layer structures

The amount of energy transmitted, reflected and absorbed is encoded in the Fresnel coefficients which emerge from the application of Maxwell equations in the frontier between two dielectrics when a layer of graphene is placed separating them.[86,87] For s-polarized light, the Fresnel coefficients for the parallel (conserved) component are given by[66]

$$t_s = \frac{2\mu_2 q_1'}{\mu_2 q_1' + \mu_1 q_2' + \mu_1\mu_2\mu_0\chi^{(0)}_{j_x j_x}(q\hat{y},\omega)} , \tag{2.14}$$

$$r_s = \frac{\mu_2 q_1' - \mu_1 q_2' - \mu_1\mu_2\mu_0\chi^{(0)}_{j_x j_x}(q\hat{y},\omega)}{\mu_2 q_1' + \mu_1 q_2' + \mu_1\mu_2\mu_0\chi^{(0)}_{j_x j_x}(q\hat{y},\omega)} . \tag{2.15}$$

The absorption is then:

$$\mathcal{A}_s = 1 - |r_s|^2 - |t_s|^2 \frac{\mu_1 q_2'}{\mu_2 q_1'} . \tag{2.16}$$

Equivalent equations are obtained for p-polarized light by replacing $\mu_i \to q_i'$, $q_i' \to \epsilon_i$ and $\chi^{(0)}_{j_x j_x}(q\hat{y},\omega) \to \chi^{(0)}_{j_x j_x}(q\hat{x},\omega)$.[†]

Their application to the simplest case, i.e., suspended graphene, reveals that the maximum absorption (2.3%) for p polarization corresponds to the normal incidence, whereas when dealing with s polarization, it is reached when

$$\left(\frac{qc}{\omega}\right)^2 = 1 - \left(\frac{\pi\alpha}{2}\right)^2 , \ \alpha = \frac{e^2}{4\pi\epsilon_0\hbar c} . \tag{2.17}$$

The angle of incidence is given by $\sin\theta = qc/\omega \Rightarrow \theta \simeq 89°$, and the absorption is exactly 50%, which resembles the theoretically highest absorption by a single interface.[88]

Also for graphene on a substrate, differences between both polarizations are important close to and beyond the light cone. Fig. 2.10 shows the results for a dielectric with $\mu = 1$ and $n = 1.5$. It can be realized that in the zone where total reflection should take place in the absence of graphene, some absorption ($\simeq 3\%$) is found for p polarization, but more than twice as much for s polarization.

2.5.2 Double layer structures

Other setups with more layers may also yield interesting results. In Ref. [72], two sheets of graphene separating three dielectrics with permittivities ϵ_1, ϵ_2 and ϵ_1 ($\epsilon_1 > \epsilon_2$) give rise to perfect transmission between the two light cones in the regime of strong light-matter coupling (for energies of the order of the fine-structure constant times the Fermi energy). The results can be

[†]Note that these expressions slightly differ from standard textbook notation.

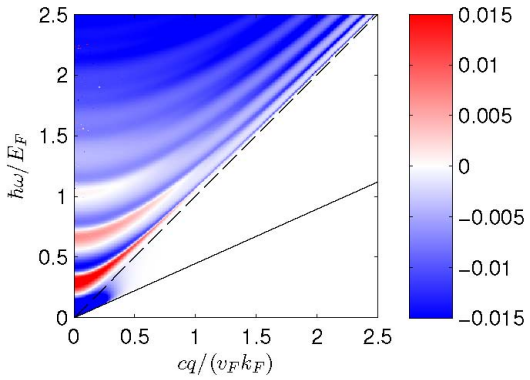

Figure 2.11: Transmission of incident light through a double-layer graphene structure with dielectric media $\epsilon_1 = \epsilon_3 = 5$, $\epsilon_2 = 1$ and $\mu = 1$. Shown is the difference $T_g - T_0$, with T_g (T_0) the transmission with (without) graphene. The distance separating the graphene layers is $d = 14.8\,\mu$m. The light cones respective to media 1 and 2 are denoted by the solid and dotted black lines, respectively.

interpreted as surface-plasmon-mediated extraordinary transmission similar to the one through sub-wavelength apertures.[89] This analysis was carried out for p polarization and here we want to extend it to s polarization. Results are shown in Fig. 2.11, where no perfect transmission takes place.[‡]

Our interpretation is the aforementioned fragility of transverse plasmons, which vanish for large layer separation in this staging unless the refractive indices n_1 and n_2 are sufficiently close to each other. As a consequence, there is no mean of tunneling s-polarized light through transverse-plasmon coupling between layers.

2.6 Conclusions

In summary, we have calculated the linear current-current response function for graphene at finite temperature and chemical potential. This analytical result enables the characterization and study of plasmons from a quite general standpoint.

This chapter focuses on the transverse channel, whose collective oscillations remained not as well studied as the ones of the longitudinal channel. As for them, we have analyzed the strong influence that temperature exerts when compared to their counterparts, i.e. that they vanish much earlier when increasing T. Red shifting of the dispersion relation or the impossibility of inducing their existence at zero doping by means of a finite temperature

[‡]The colored region inside the light cone for $q \to 0$ is due to high reflectivity of graphene at low frequencies.

also stand out as clear differences.

Moreover, the influence of the dielectric surroundings on transverse plasmons has been targeted, aiming at a increase of their confinement. The main consequences are enclosed in the evolution of the dispersion relation as a result of modifying the refractive index in which graphene is embedded. We have described these curves for a wide range of values of the refractive index, which made it necessary to go beyond the local response and showed that maximal confinement is obtained for $n \simeq 40$. This confinement can be enhanced by placing graphene inside a cavity consisting of a perfect diamagnet, i.e., $\mu = 0$. It reaches a maximum for a certain distance below which no transverse plasmons can be sustained, which can be used for a sensor.

In the last section, we commented on some aspects of the absorption of electromagnetic radiation by a single- and double-layer systems due to the presence of graphene, where the polarization of light as well as the incident angle give rise to fluctuations up to $\sim 50\%$.

Chapter 3

Mass-profile quantum dots in graphene and artificial periodic structures

3.1 Introduction

Due to the chiral nature of its carriers, gapless graphene cannot confine electrons via a lateral electrostatic potential, giving rise to the so-called Klein paradox.[11,90] Several setups have been found to tackle this problem, producing nanostructures of graphene in form of quantum dots[91,92] or nanoribbons.[93,94] Also confining Dirac electrons in rings with edge reconstruction,[95–97] inhomogeneous constant magnetic fields,[98–100] superlattices over different substrates[101–103] with a modulated Fermi velocity[104] or scalar potential[105] as well as nanohole patterning[106] and topological mass terms[107–110] have been discussed. So much research has aimed at achieving a gap opening because it is essential in regard to the design of nanodevices or possible applications to quantum computing.[111,112]

Once we count on any of these possibilities to confine electronic states, the ability to control the level degeneracy is of high interest. As an example, valleytronic devices[113] or spin qubits[112,114] usually require a lifted valley degeneracy to be engineered. This, in turn, is achievable by means of magnetic fields[95,115] or etching graphene ribbons with armchair boundaries.[112]

In this chapter, we study yet another alternative to confine electrons in graphene consisting in a position-dependent gap. This possibility was first discussed in the context of infinite-mass boundaries by Berry and Mondragon and was mainly motivated by theoretical considerations.[116] Other works have also analyzed the spectra of circularly shaped finite-mass profiles in the presence of electromagnetic fields.[117–119] Here, our renewed interest is based on recent experiments on graphene on top of an Ir(111) substrate in turn covered by Iridium clusters, which we summarize in Sec. 3.2. Covered and uncovered regions show different particle gaps, but the substrate

and the clusters leave the linear spectrum of graphene almost unaffected.[101] Quantum dots confined by a finite-mass boundary can thus be designed with nanosize accuracy where the local change in the one-particle gap is introduced by the removal of substrate clusters selected at will by an STM-tip.[12] So different quantum dot sizes and geometries are within reach and shall be discussed here.

In particular, we will study the bound-state spectrum of a circular dot as a function of the radius and the magnetic-field dependence. We will further establish a comparison between our system, i.e., mass-profile quantum dots (MP-QDs) and a potential-well quantum dot (PW-QD) previously characterized in Refs. [115,120]. We discuss their similar dependence on the dot size and the magnetic field, and also that the valley degeneracy splits proportionally to B in both cases. On the other hand, we remark several differences between them, e.g., the spectrum of MP-QDs being particle-hole symmetric and less dense, thus being more susceptible to optical experiments. Dealing with a simpler level structure may be advantageous also for applications, which endorses the interest in featuring MP-QDs. Finally, we relate the properties of the spectra obtained at high B fields to the non-trivial Berry phase of π in graphene. This gives rise to striking differences with respect to quantum dots hosted by other systems like a conventional 2D electron gas. We emphasize the novelty of this regime, which has not been addressed in the aforementioned related works and might be at experimental reach also in systems with high local strains.[121]

At last, again owing to the experimental feasibility to create periodic arrays of identical nano-structures and in regard to possible applications like those introduced in Ref. [122], a linear chain of MP-QDs is analyzed. Its band structure is calculated for a fixed radius R as a function of the lattice parameter D, and the relevance of overlap-assisted hopping processes is discussed for closely packed arrays. Single-particle processes such as hopping or spontaneous decay rates are compared to excitonic processes. Varying the distance between the dots allows the tuning to a Frenkel excitonic regime which can be described by a bosonic tight-binding Hamiltonian.

This chapter is organized as follows. Sec. 3.2 discusses several experiments that inspired our theoretical work. In Sec. 3.3, we present the model for mass-profile quantum dots and its solution. In Sec. 3.4.1, we discuss the spectrum at $B = 0$ for MP-QDs and PW-QDs, whereas in Sec. 3.4.2 we extend this analysis to $B \neq 0$. Sec. 3.5.1 focuses on a MP-QD one-dimensional linear chain, and in Sec. 3.5.2 the Coulomb interaction between electrons is included. We summarize our conclusions in Sec. 3.6. In three appendices, we present details of the solution of the eigenvalue problem and define the tight-binding model for arbitrary arrays of MP-QDs.

3.2 Experimental background

The experimental technique that partly motivates the theoretical analysis of this chapter has been reported in detail in Ref. [12]. In this section, we proceed to outline it, also making reference to other related measurements.

The setup is built on a graphene mono layer epitaxially grown on an Ir(111) substrate. This scenario has been a matter of interest by itself for several reasons. First of all, graphene has been reported to grow with high structural quality over this and other transition metal surfaces like Ni(111) and Ru(0001).[12,123–125] Secondly, the interaction with the Ir(111) substrate turns out to be weak: the resulting moiré pattern, with lattice parameter $\sim 2.5\,\mathrm{nm}$ —see Fig. 3.1(d)—, presents a band structure close to neutrality practically unaltered with respect to pristine graphene. Actually, Dirac cones have been observed through ARPES —cf. Figs. 3.2(a) and 3.2(c)— , with a gap less than $0.20\,\mathrm{eV}$ and shifted just $\sim 0.10\,\mathrm{eV}$ over the Fermi energy.[126] Theoretical calculations support these measurements, too.[127] Importantly, this is in contrast with the aforementioned Ni(111) and Ru(0001), whose bands strongly hybridize with the Dirac cones, completely blurring their original shape.[126] These remarkable features make Ir(111) stand out as an ideal platform to engineer heterostructures involving graphene.

The experimental technique that concerns us involves the deposition of Ir nano particles on this setup. This can be achieved by the evaporation of Ir from high purity filaments, which ends up clustering and covering the graphene monolayer according to the periodicity of the graphene/Ir moiré pattern. STM images clearly show arrays of $\sim 2.5\,\mathrm{nm}$ Ir clusters with very few defects, cf. Fig. 3.1(e). Their formation has been thoroughly discussed in Refs. [128,129], revealing that graphene strongly bonds with the metal substrate precisely at the nucleation regions. There, the hybridization of graphene orbitals changes from sp^2 to sp^3, which entails changes in the electronic structure with respect to the uncovered zones. Actually, the sublattice symmetry breaks, bringing about a gap opening of approximately $0.4\,\mathrm{eV}$, see Fig. 3.2(b).

Up to this point, the manipulations have taken place at a global scale, what is usually referred to as a *bottom-up* procedure. The full technique stems from an original combination with *top-down* (i.e., local) operations, which are at reach with an STM tip. This last step consists of the selective removal of clusters, which can be done with 100% extraction probability and extraordinary accuracy, see Fig. 3.2(f). We leave the technical details involving the patterning procedure to be consulted in Ref. [12].

This technique provides the remarkable possibility of engineering a mass profile in graphene, the gap roughly ranging from $50\,\mathrm{meV}$ in the uncovered zones to $400\,\mathrm{meV}$ under the clusters. As a result, mass-confined quantum dots can be tailored up to nanometer accuracy, which is the starting point of our theoretical analysis. The measured values of the gap will be used in

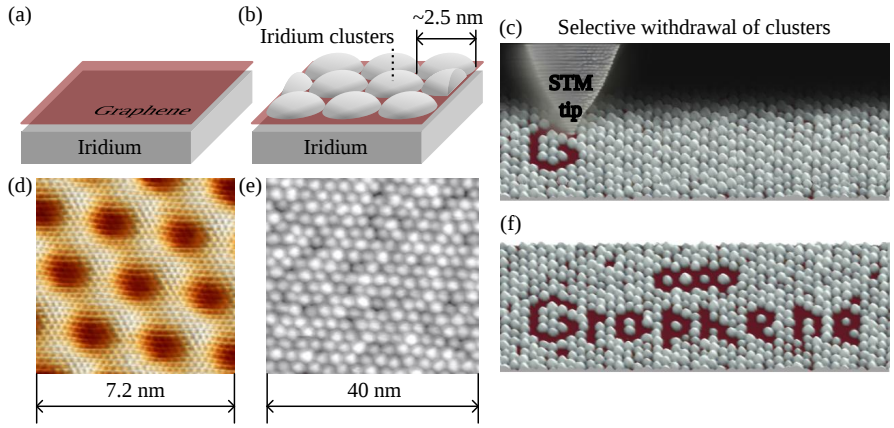

Figure 3.1: Outline of the whole experimental technique: a graphene monolayer epitaxially grown on an Ir(111) substrate —see (a)— is covered by Ir clusters —sketched in (b)—. Afterwards, they can be selectively removed by an STM tip, as shown in (c). (d)-(f) are the experimental STM images of these three stages, respectively. (d) clearly shows the moiré pattern resulting from the lattice mismatch between graphene and Ir(111). The nucleation spots for the deposition of Ir are arranged in a triangular lattice with lattice parameter $\sim 2.5\,\text{nm}$, which determines the size and arrangement of the clusters, seldom presenting defects —see (e)—. The final result (f) proves the high degree of accuracy of the etching process.

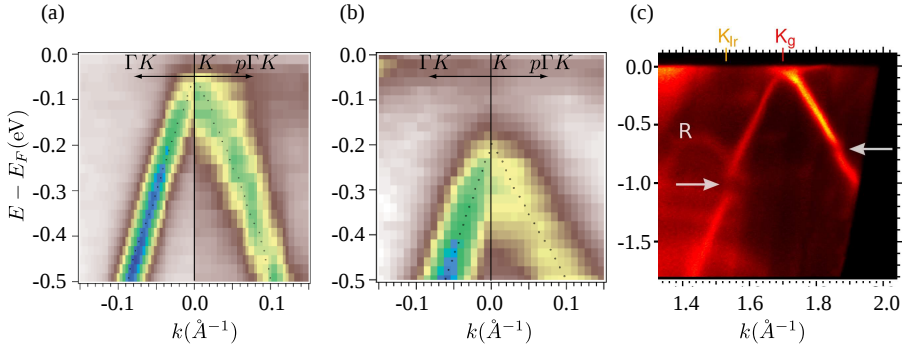

Figure 3.2: ARPES intensities in arbitrary units of the π-band of uncovered —(a) and (c), both corresponding to the sketch of Fig. 3.1(a)— and covered —(b), respective to Fig. 3.1(b)— graphene over Ir. (a) and (b) show the vicinity of the Fermi energy, whereas (c) goes beyond to show the mini gaps (marked with arrows) and folded bands (labeled with an R) distinctive of moiré patterns. Figures were extracted from Refs. [101,126] with permission of the authors.

subsequent calculations.

3.3 The model

For a position dependent gap $2\Delta(r)$, the Hamiltonian of graphene can be written as

$$H_\tau = H_0 + \tau\Delta(r)\sigma_z, \tag{3.1}$$

with

$$H_0 = v_F(\mathbf{p} + e\mathbf{A})\cdot\sigma\,, \tag{3.2}$$
$$\mathbf{B} = \nabla\times\mathbf{A} = (0,0,B)\,. \tag{3.3}$$

$\sigma = (\sigma_x, \sigma_y)$ and σ_z are the Pauli matrices, $v_F = 10^6$m/s is the Fermi velocity, $e > 0$ and the index $\tau = \pm 1$ labels the valleys.

The experimental techniques summarized in Sec. 3.2 allow to create MP-QDs with extremely versatile shapes. As a first foray in the physics of such systems, we aim at exploiting the symmetries of simple geometries. We will thus consider a circular and step-like mass profile,

$$\Delta(r) = \Delta_1\Theta(r-R) + \Delta_2\Theta(R-r) \tag{3.4}$$

with $\Delta_j = m_j v_F^2$ for $j = 1, 2$, and R the radius of the quantum dot. It can be solved by playing upon the rotational invariance, $[J_z, H_\tau] = 0$, with $J_z = -i\partial_\phi + \sigma_z/2$ the total angular momentum —orbital plus lattice— projected onto the $\hat{z}$ direction. So in polar coordinates, the eigenvectors can be written as

$$\psi^\tau(r,\phi) = e^{i(j-1/2)\phi}\begin{pmatrix}\chi_A^\tau(r)\\ \chi_B^\tau(r)e^{i\phi}\end{pmatrix}, \tag{3.5}$$

where j is a half odd integer. With Eq. (3.5), the eigenvalue problem of the Hamiltonian, Eq. (3.1), can be written as

$$r^2\partial_r^2\chi_\sigma^\tau(r) + r\partial_r\chi_\sigma^\tau(r) = (b^2r^4 + a_\sigma r^2 + n_\sigma^2)\chi_\sigma^\tau(r)\,, \tag{3.6}$$

where $\sigma = \pm 1$ corresponds to the A/B sublattice. We have also defined

$$a_\sigma = 2b(j+\sigma/2) - (E^2-\Delta^2)/(\hbar v_F)^2\,, \tag{3.7}$$
$$\Delta = mv_F^2\,,\ n_\sigma = |j-\sigma/2|\,,\ b = \frac{eB}{2\hbar}\,. \tag{3.8}$$

The solutions of Eq. (3.6) are given in appendices B.1 and B.2 for non-zero magnetic field $B \neq 0$ and $B = 0$, respectively. The matching conditions imposed on Eq. (3.5) at $r = R$, also detailed there, yield the bound-state

energies. The eigenstates will be labeled as $|\tau, j, n\rangle$, n ordering them in ascending absolute value of the energy.

A similar model was recently studied in Ref. [115],

$$H_\tau = H_0 + \tau\Delta_0\sigma_z + U(r)\,, \tag{3.9}$$

with a step-like electrostatic, rotationally invariant potential, $U = \Theta(R - r)U_0$ ($U_0 < 0$). Unlike in the case of a MP-QD —Eq. (3.1)—, the gap of a PW-QD —Δ_0— is not position dependent, whereas H_0 is again given by Eq. (3.2). The differences are sketched in the insets of Fig. 3.3, which outline the spectrum of the two different quantum dots considered throughout this work. $U_0 = (\Delta_1 - \Delta_2)\Theta(r - R)$ was chosen so as to give the same well depth as in the MP-QD.

The relation between the eigenfunctions of Eqs. (3.1) and (3.9) is discussed in appendices B.1 and B.2, as well as the symmetries they display. Further analysis about the spectra is held in subsequent sections.

3.4 Electronic spectrum of a single quantum dot

3.4.1 $B = 0$ case

Let us first discuss the spectra in the absence of magnetic fields. Results are plotted in Fig. 3.3. As it is proved in appendix B.2, the levels are doubly degenerate,

$$E(\tau, j) = E(-\tau, -j)\,, \tag{3.10}$$

reflecting the time reversal symmetry that connects the two valleys. Only for MP-QDs the electron-hole symmetry is also present,

$$E(\tau, j) = -E(-\tau, j)\,, \tag{3.11}$$

while absent in the case of PW-QDs (cf. also the discussion in appendix B.2 and the insets of Fig. 3.3). This aspect implies a striking difference: MP-QDs can host confined electron-hole pairs, whereas they are not present in PW-QDs.

Further comparing the spectra of MP-QDs and PW-QDs, one can notice a higher confinement of the states in the latter. This implies a denser spectrum of PW-QDs for the same depth of the mass and potential well. In turn, the larger level spacing makes MP-QDs more accessible for optical spectroscopy.

For experimentally realizable MP-QDs with $R \lesssim 10\,\text{nm}$, intra-band transitions between bound-state levels have a frequency of the order of 10 THz, enabling our system to support terahertz optical applications. For MP-QDs with $R \lesssim 6\,\text{nm}$, only one bound state in the conduction band is present, defining a possible qubit which can be optically turned on (electron-hole

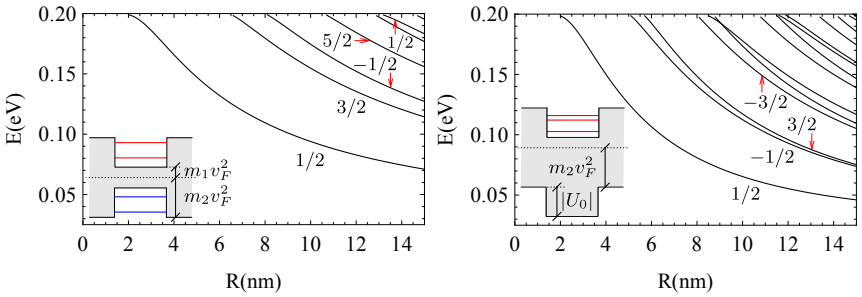

Figure 3.3: Spectra of a circular MP-QD (left) and a PW-QD (right) for $B = 0$. The values of j respective to $\tau = 1$ label the most bounded energy levels. Insets: diagrams of the bound-state levels in the mass and potential well. The shadowed region corresponds to forbidden values of the energy, and the colored lines inside the wells represent bound states. The electron (red)-hole (blue) symmetry is only present in the MP-QD.

pair creation) and off (neutral ground state). Furthermore, excitonic effects lifting the valley degeneracy could manifest many-body effects also in the THz range, promoting the system as an experimentally realizable probe for interactions in quantum dots, including electron-phonon coupling.[130]

3.4.2 $B \neq 0$ case

In Fig. 3.4, we show the spectra of a MP-QD (left) and a PW-QD (right) as a function of the radius for zero and non-zero magnetic field B. We observe a splitting between levels belonging to different ($\tau = \pm 1$) valleys which is proportional to the magnitude of the applied magnetic field. For $B = 4\,\mathrm{T}$, we can achieve a splitting up to 2 meV (THz regime) for quantum dots with only one bound state (i.e. for $R \lesssim 6\,\mathrm{nm}$). Remarkably, the splitting of the levels is considerably larger in the MP-QD.

These plots also show that if levels belong to different valleys, their energies are modified by the magnetic field in a different manner. Whereas every $\tau = +1$ level rises with B, some $\tau = -1$ ones are lowered, i.e., become more confined. Interestingly, for some R values for which there were an equal number of $\tau = \pm 1$ states at $B = 0$, we observe that new $\tau = -1$ states appear and other $\tau = +1$ states vanish when applying a sufficiently high magnetic field. The opposite happens in the valence band. As we will see later, this fact will be relevant to explain the spectrum for $R \gg l_B$, with the magnetic length $l_B = \sqrt{\hbar/(eB)}$.

In Fig. 3.5, we present the spectra as a function of the fixed dot radius R over the magnetic length l_B. They show more clearly one of our previous considerations concerning the appearance and disappearance of states with different valley index (see Fig. 3.4), i.e., as long as B is increased for a

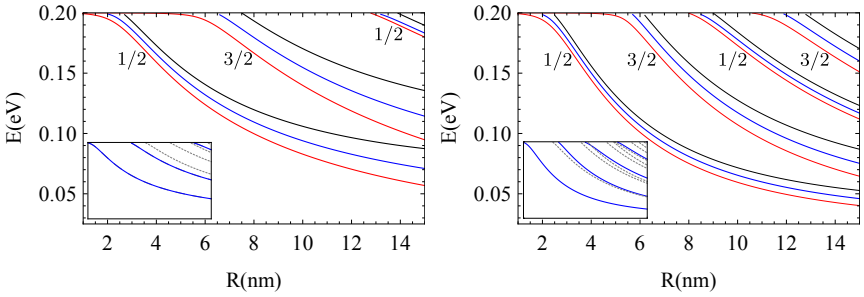

Figure 3.4: Splitting of the valley degeneracy of a circular MP-QD (upper panel) and a PW-QD (lower panel) when a perpendicular magnetic field is applied. Blue lines correspond to $B = 0$, and they split into black ($\tau = 1$) and red ($\tau = -1$) lines when applying $B = 4$T. For clarity, only levels with $|j| = \{1/2, 3/2\}$ (labels of the curves) have been plotted. In the insets, where the full spectra at $B = 0$ is shown, they are highlighted in blue.

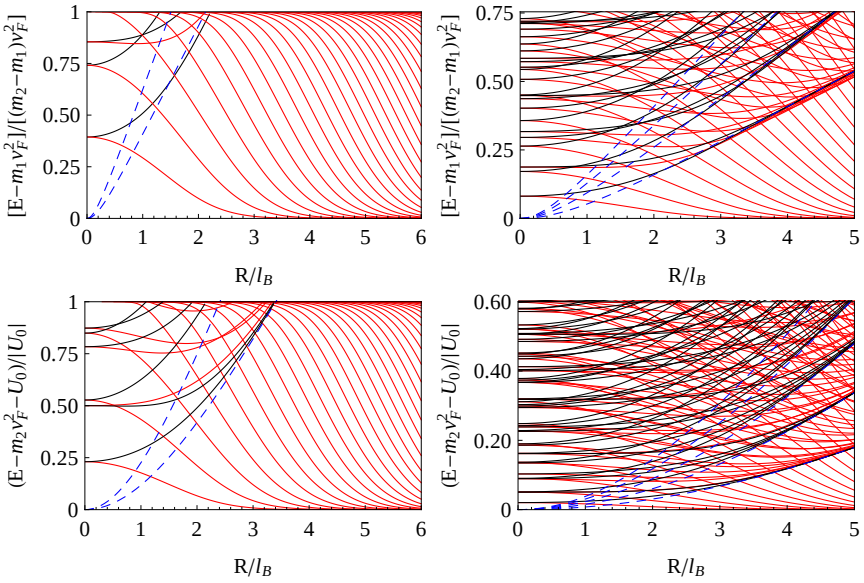

Figure 3.5: Upper panels: MP-QDs. Lower panels: PW-QDs. Left panels: spectra for $R = 10\,\text{nm}$ ($R = l_B \Rightarrow B = 6.6\,\text{T}$). Right panels: spectra for $R = 40\,\text{nm}$ ($R = l_B \Rightarrow B = 0.41\,\text{T}$). Black (red) corresponds to $\tau = (-)1$ valley. Convergence to Landau levels (bottom of the well and dashed blue lines) can clearly be appreciated. The spectrum structure with only $\tau = -1$ levels and approximately equidistant energy levels appears for $B > B_c$, see Eq. (3.13).

fixed R, some $\tau = +1$ levels are no longer bound states whereas others with $\tau = -1$ enter the well. Remarkably, one can appreciate three (and not two, as usual) different regions in these plots for both the MP-QD and the PW-QD: i) for $B \to 0$, we recover the degenerate spectrum, in which the level spacing does not seem to have a definite structure. ii) As soon as B is sufficiently large, the levels converge to straight lines and to the bottom of the well. iii) For greater values of B, only bound states with $\tau = -1$ are allowed in the conduction band, see left panels of Fig. 3.5. In this last case, for energies not close to the top or the bottom of the well, we encounter equally spaced non-degenerate levels. Near the bottom, we can notice how a growing number of states with B converge to the lowest possible energy. We will devote part of this section to discuss the emergence of these patterns featured in points ii) and iii).

Concerning the intermediate region ii), Fig. 3.5 resembles a typical Fock-Darwin spectrum,[85,108] the potential well or the mass profile playing the role of the harmonic potential in that model. In this regime, the energy term corresponding to B dominates over the well depth. This is confirmed by the dependence

$$|E_n| = \sqrt{\Delta^2 + 2n\left(\hbar v_F / l_B\right)^2} \tag{3.12}$$

($n \geq 0$ refers to the nth asymptote), revealing a structure characteristic of Landau levels in gapped graphene.[131,132] The existence of the lowest Landau level is of particular relevance, since it is responsible for the structure of the spectrum for large B, as discussed below.

The degeneracy of the Landau levels in this region is also noteworthy, which is proportional to the magnetic flux through the system. One can verify this dependence in Fig. 3.5: while B is increased, more $\tau = -1$ levels appear inside the wells and converge asymptotically to graphene Landau levels, providing them with the required degeneracy.

For B greater than a critical value

$$B_c \simeq \frac{\left(m_2^2 - m_1^2\right) v_F^2}{2e\hbar} \simeq 30\,\mathrm{T}, \tag{3.13}$$

only the lowest Landau level will remain, see Fig. 3.5. We encounter the aforementioned region iii), with only $\tau = -1$ states. Our previous considerations on the degeneracy explain the level structure of this part of the spectrum. As long as B is increased, a constant income of levels is needed to guarantee that the lowest Landau level is degenerate enough. As a result, our quantum dots show an excited spectrum of equally spaced levels that will converge to the bottom of the well at higher B. Their difference in energy can be tuned with the radius, since a higher area $\mathcal{A}$ increases the degeneracy of Landau levels, in turn implying a greater density of incoming states. Experiments with graphene have been carried out for values of

$B \gtrsim B_c$,[133] so this regime may be observable for our values of Δ_1 and Δ_2. As an alternative, pseudo-magnetic fields exceeding B_c could be induced by strain.[121]

As we have seen, the chiral nature of carriers in graphene manifests itself in the results. The presence of a Landau level whose energy is B independent is the most determinant feature in the quantum dot spectrum. It guarantees the existence of bound states at arbitrarily high values of B with the structure of the third region discussed before. This is in stark contrast to quantum dots of ordinary 2D semiconductors, where no bound states exist beyond some critical B_c. The approximate equidistant level structure might be useful for optical experiments in the THz-regime, inducing transitions between several adjacent levels. Since conduction and valence bands host bound states of opposite valleys, no interband transitions are allowed.

3.5 Arrays of MP-QDs

The controlled removal of metal clusters on top of graphene placed on a Ir(111) substrate allows for creating artificial periodic lattice structures within the nanoscale, cf. Sec. 3.2 and references therein. In this section, we will thus focus on linear chains of MP-QDs, setting with this elementary example the procedure to analyze more complicated one- or two-dimensional arrays. For the sake of simplicity, we fix the dot radius $R = 6.5\,\mathrm{nm}$, which is the biggest yielding a single bound state per band (cf. Fig. 3.3). Our aim is to carry out a tight-binding calculation considering both the valence and the conduction band. Later on, we will also add the Coulomb interaction between the excitations hosted in different dots.

3.5.1 One-particle physics

We start our analysis by considering two MP-QDs whose centers are separated by a distance D. It turns out that the overlap λ of the two wave functions is not negligible for D close to $2R$. This is demonstrated in Fig. B.3. Although its square is smaller, we will not neglect it for the moment. Actually, we will show below that its contribution will be relevant for an array of quantum dots with a small lattice parameter $D \simeq 2R$. Henceforth, only $O(\lambda^n)$ terms with $n \geq 3$ will be discarded unless the contrary is specified. This introduces an error of less than 1%, see right panel of Fig. 3.7.

A sketch of all different processes that can take place between the two MP-QDs is shown in Fig. 3.6. In appendix B.3, we demonstrate that the probability amplitudes of the hopping-processes ξ, κ, μ and $\lambda\kappa$ are relevant, whereas η, the electron-hole annihilation, can be shown to be precisely zero.

$\lambda\kappa$ is a term of the order of λ^2 (cf. Fig. 3.7). It is not a direct hopping parameter like $\{\eta, \kappa, \mu\}$, but a hopping process provoked or *assisted* by the

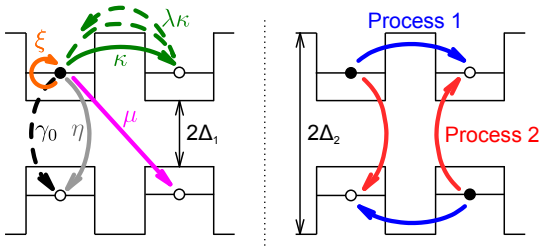

Figure 3.6: Outline of different hopping processes between two MP-QDs. Left hand side: single-particle processes. γ_0 is the spontaneous decay, Eq. (3.20). Right hand side: interaction processes.

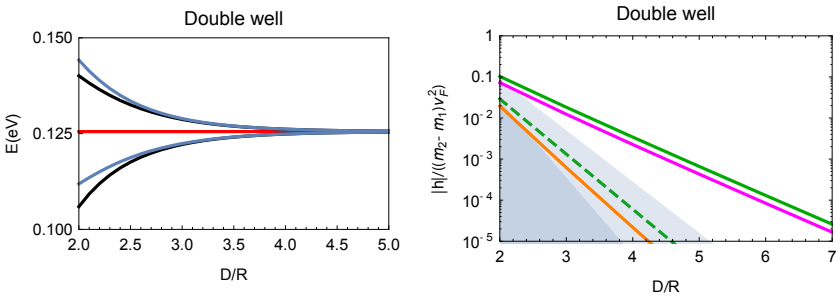

Figure 3.7: Left plot: Bound-state energies of two nearby MP-QDs. Red: Bound-state energy of a single well. Black (blue): Bound-state energies neglecting the overlap squared (cubed) of the wave functions. For more details, see appendix B.3. Right panel: Comparison between the hopping processes depicted in Fig. 3.6 (with the same color code). h labeling the vertical axis refers to κ, μ and ξ. The strong (light) shadowed region corresponds to values below the overlap cubed (squared).

overlap.

The left plot of Fig. 3.7 shows the spectrum of the double well as a function of the distance between the centers. There, it can be seen that considering or neglecting terms of the order of the overlap squared does not alter the values of the energies considerably. Nevertheless, the situation will be different in periodic arrays of quantum dots closely packed, as we will discuss below.

In appendix B.3, we define a tight-binding model for a linear chain of MP-QDs with $R = 6.5\,\text{nm}$. The resulting bands appear in Fig. 3.8, ranging from dispersive to flat with the increase of D. The gaps and carrier effective masses are thus tunable with the lattice parameter.

Clearly, for a lattice parameter close to the dot diameter, the effect of the overlap on the band structure is significant. This is mainly due to the

next-nearest neighbor hopping assisted by λ, see Fig. B.4 and its discussion in appendix B.3. Note that this effect cannot take place in a double well and this explains why the influence of the overlap-assisted processes on the eigen energies was much weaker.

As a result, the effective mass m^* of the carriers with $k \simeq 0$ is strongly renormalized by λ. Remarkably, for a closely packed chain, the overlap-assisted processes give rise to a change of sign in the curvature of the bands around $k = 0$ (see inset of Fig. 3.8). For low densities, the ground state is thus given by a Fermi ring[134] and shows that the implications of considering second order processes in a tight-binding approach go beyond a mere correction in eigen energies.

3.5.2 Coulomb interaction

The second part of this section aims to include Coulomb interactions in our system. Processes like those depicted on the right hand side of Fig. 3.6 come into play. Their rates γ_C can be calculated with the help of Fermi's golden rule,

$$\gamma_C = \frac{2\pi}{\hbar} |\langle f|V_{\text{int}}|i\rangle|^2 F_{fi}\,, \tag{3.14}$$

where V_{int} is the Coulomb interaction and F_{fi} the generalized delta-function, see Eq. (3.16).[135] $|i\rangle$ ($|f\rangle$) refers to the initial (final) state of the transition which is a two-particle —electron-hole— state

$$|E\mathbf{R}_a\rangle \otimes |E'\mathbf{R}_b\rangle\,, \tag{3.15}$$

where, in turn, $|E\mathbf{R}_\alpha\rangle$ describes the eigenstate with energy E of a single well centered at $\mathbf{R}_\alpha$. Since we are dealing with only a single bound state per well in the valence and conduction band, and since the Coulomb interaction does not couple valleys nor spins, we can neglect the other quantum numbers (j, τ, spin) that strictly label the state and only keep E and $\mathbf{R}_\alpha$ in Eq. (3.15). In the overlap factor

$$F_{fi} = \int_{-\infty}^{\infty} d\epsilon\, \rho_i(\epsilon)\rho_f(\epsilon)\,, \tag{3.16}$$

a Lorentzian was considered for the density of states of the $|i\rangle$ ($|f\rangle$) level, whose energy is centered at $E_{i(f)}$:

$$\rho_{i(f)}(\epsilon) = \frac{1}{\pi} \frac{\Gamma}{(\epsilon - E_{i(f)})^2 + \Gamma^2}\,. \tag{3.17}$$

A typical broadening of $\Gamma = 10\,\text{meV}$ was used.[9]

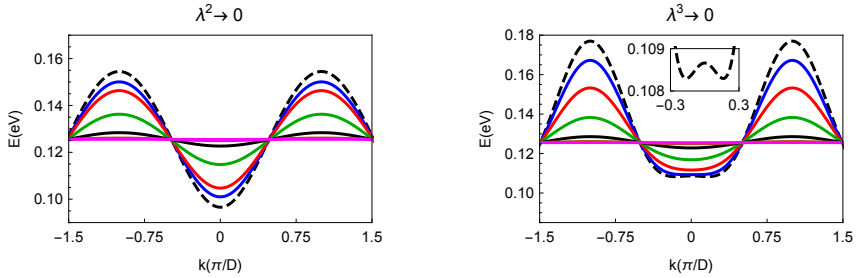

Figure 3.8: Bands of a one-dimensional chain of quantum dots. Dashed black: $D = 2\,R$; blue: $D = 2.1\,R$; red: $D = 2.3\,R$; green: $D = 2.7\,R$; solid black: $D = 3.5\,R$; magenta: $D = 6\,R$. Terms of higher order than the overlap squared (cubed) are neglected in the left (right) figure. The inset plots a close view of the $D = 2\,R$ curve, showing its negative curvature at $k = 0$.

Process 2 in Fig. 3.6 is an example of Förster transfer.[136] In this case, one can approximate the matrix element in Eq. (3.14) by its multipolar expansion,

$$\langle f|V_{\rm int}|i\rangle \simeq \frac{1}{4\pi\epsilon_0}\frac{D\mu_a\cdot\mu_b - 3(\mu_a\cdot\mathbf{D})(\mu_b\cdot\mathbf{D})}{D^5}\,, \tag{3.18}$$

where $\mathbf{D} = \mathbf{R}_a - \mathbf{R}_b$, and in turn $\mathbf{R}_a$ and $\mathbf{R}_b$ are the centers of the MP-QDs involved in the process. The dipole momenta are

$$\mu_j = \int d^2r\,|\psi(\mathbf{r}-\mathbf{R}_j)|^2(\mathbf{r}-\mathbf{R}_j)\,,\ j=\{a,b\}\,, \tag{3.19}$$

with $|\psi(\mathbf{r}-\mathbf{R}_j)|^2$ the density probability associated to the single-particle bound state centered at $\mathbf{R}_j$. We checked numerically the excellent agreement between Eq. (3.18) and the exact value of the transition matrix element.

A comparison between the rates γ of all processes depicted on Fig. 3.6 is shown in Fig. 3.9. We highlight the algebraic behavior of the Förster transfer versus the exponential one of all the rest. The spontaneous decay rate,[136]

$$\gamma_0 = \frac{\omega_0^3|\mu|^2}{3\pi\epsilon_0\hbar c^3} \simeq 1.9\cdot 10^7\,\mathrm{s}^{-1}\,, \tag{3.20}$$

is also plotted as reference, with μ given by Eq. (3.19) and $\hbar\omega_0$ being the energy difference between the levels involved. For $D \simeq 7R$, this indicates the existence of a regime in which Förster transfer is the dominant process. In that case, the particle-hole excitations have a sufficiently long lifetime to overlap with the adjacent site to form a band. These Frenkel excitons can

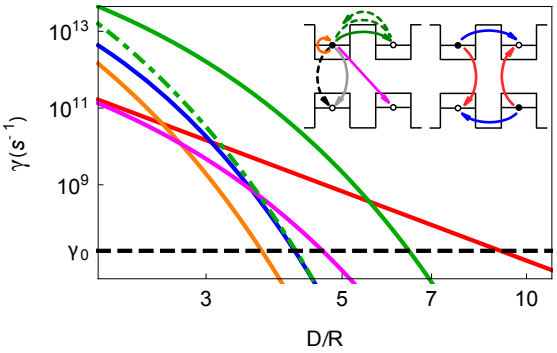

Figure 3.9: Comparison between the rates γ, Eq. (3.14), of single-particle and excitonic processes. The color code was introduced in Fig. 3.6. It is reproduced in the inset for clarity.

thus be described by the following quasi-bosonic tight-binding Hamiltonian in the diluted limit:

$$H \simeq -\sum_{\langle i,j \rangle} \left[t_{ex} a^\dagger(\mathbf{R}_j) a(\mathbf{R}_i) + \text{h.c.} \right]. \tag{3.21}$$

Here, $a(\mathbf{R}_i) \equiv c_-^\dagger(\mathbf{R}_i) c_+(\mathbf{R}_i)$ annihilates and $a^\dagger(\mathbf{R}_i) \equiv c_+^\dagger(\mathbf{R}_i) c_-(\mathbf{R}_i)$ creates an exciton at lattice site $\mathbf{R}_i$, where $c_+^{(\dagger)}(\mathbf{R}_i)$ and $c_-^{(\dagger)}(\mathbf{R}_i)$ are the electron annihilation (creation) operators in the upper and lower levels of a single dot centered at $\mathbf{R}_i$, respectively. The excitonic operators $a^{(\dagger)}(\mathbf{R}_i)$ satisfy bosonic commutation relations in the diluted limit.[137]

The effective excitonic hopping amplitude induced by Förster transfer is given by $t_{ex} \equiv \langle +\mathbf{R}_j; -\mathbf{R}_i | V_{int} | -\mathbf{R}_j; +\mathbf{R}_i \rangle$ (cf. the notation in appendix B.3), which takes place only between nearest neighbors. Other processes, outlined in appendix B.3 and which were neglected in Eq. (3.21), would induce a finite lifetime of the excitons. For lattices with $D/R \lesssim 3.5$, the bands turn dispersive (see Fig. 3.8) and single-particle processes become dominant.

The previous considerations promote the system under study to a highly tunable probe which can further host collective excitations in form of interband plasmons.[35,138] The engineering of lattices exhibiting different symmetries and dimensionality thus opens up a new scenario to explore interactions in artificial lattices.

3.6 Conclusions

Motivated by recent experimental advances, we have studied the bound-state spectra of mass-profile quantum dots (MP-QDs) and compared it with

the corresponding spectrum of recently studied potential-well quantum dots (PW-QDs). Both systems allow to confine electrons in 2D and control the lifting of the valley degeneracy by applying a perpendicular magnetic field to the sheet. We have seen that the behavior of their spectra as a function of the radius and the magnetic field is similar, but the level structure of MP-QDs is simpler. This could make the latter more suitable for optical applications in the mid-infrared and THz regime. Moreover, we have featured different regions of the spectra according to the magnitude of the magnetic field. Besides the quantum dot spectrum at $B \to 0$, we have discussed the convergence to Landau levels at intermediate values of B and the appearance of an equally spaced level structure for large B-fields. The latter arises due to the existence of a lowest Landau level pinned to the band edge whose energy is B independent, in stark contrast with quantum dots hosted by conventional 2D systems.

In the second part, the electronic spectrum of linear chains of MP-QDs with fixed radius $R = 6.5\,\mathrm{nm}$ (and therefore a single valence and conduction bound level) was discussed. Bands of tunable gap and curvature were then obtained. Overlap-assisted processes are shown to play a significant role for closely packed arrays, renormalizing the effective mass of the carriers to the extent of changing its sign for $D \simeq 2R$. When including interactions, the engineered lattice parameter allows to encounter Frenkel excitons. Remarkably, a system of bosons in a linear chain ultimately governed by efficient Förster transfer between adjacent dots can be reproduced for $D \simeq 7R$. This analysis paves the way to research on the Bose-Einstein condensates virtually hosted by this kind of systems.

Chapter 4

Hamiltonian optics of hyperbolic polaritons in hBN nanogranules

4.1 Introduction

As we mentioned in Ch. 1, subwavelength confinement of electromagnetic radiation is one of the state-of-the-art topics in nano-optics. Ch. 2 dealt with light-electron coupling, resulting in plasmons, as the mechanism to achieve it. Now, we turn to analyze another kind of light-matter coupling, involving phonons instead, whose corresponding excitations receive the name of polaritons. These emerge as a promising prospect for confinement purposes in two and three dimensions. Remarkably, the fact that they present lower losses than plasmons in metals or some of their hallmarks, like their directionality or the exotic refraction that we will discuss in detail, make them particularly appealing. Furthermore, their experimental observation is at reach by novel near-field techniques, which encourages both their theoretical study as well as the quest for possible applications in the fields of condensed matter physics and optics. We will give an overview of these topics in Sec. 4.1.1.

This chapter initially focuses on recent experiments performed on hBN nanogranules, which have reported highly confined subwavelength resonances of polaritonic nature with low losses and great quality factors. A summary is presented in Sec. 4.2. Our subsequent analysis aims at their theoretical description and, above all, at the search for an accurate physical picture. For such purposes, Hamiltonian optics emerges as a convenient tool to be combined with the Einstein-Brillouin-Keller procedure on one side and Gutzwiller's trace formula on the other. Secs. 4.3, 4.4 and 4.5 focus on these topics, respectively. These formalisms are of wide use in semi-classical physics, aiming at the intermediate regime between particle and wave dynamics. Besides reproducing the measurements, our analysis paves the way to the interpretation of intensity patterns in cutting-edge near-field experi-

ments by means of ray optics, which is analyzed in Sec. 4.6. Sec. 4.7 closes the chapter with the conclusions.

4.1.1 Hyperbolic materials

In this section, we introduce hyperbolic materials and summarize the main features of their extraordinary electromagnetic modes. In particular, we will focus on *natural* hyperbolic materials, which result from the combination of an anisotropic electromagnetic response and its coupling to phonons.

As for the first factor, we recall that in anisotropic solids, the dielectric constant is no longer a scalar, but a tensor $\hat{\epsilon}$ instead. Therefore, $\mathbf{D} = \hat{\epsilon}\,\mathbf{E}$ and $\mathbf{E}$ are not aligned. $\hat{\epsilon}$ is given by its three eigenvalues ϵ_x, ϵ_y and ϵ_z, namely the dielectric constants along the principal or most symmetric axes. In particular, we will focus on crystals with a rotational symmetry around the z axis, which results in $\epsilon_x = \epsilon_y \equiv \epsilon_\perp$. We will refer to $\epsilon_\perp$ (ϵ_z) as the in-(out-of-)plane dielectric constant.

Hyperbolic or extraordinary modes emerge in this context when $\epsilon_z\epsilon_\perp < 0$. That is, when the material behaves as a metal —in the sense of screening propagating radiation— along some directions and as a dielectric along the rest. They are named after the shape of their isofrequency contours (see Fig. 4.1), given by the hyperboloid

$$\frac{k_x^2 + k_y^2}{\epsilon_z} + \frac{k_z^2}{\epsilon_\perp} = \mu\frac{\omega^2}{c^2}\,. \tag{4.1}$$

Here, $\mathbf{k} = (k_x, k_y, k_z)$ is the wavevector, μ the relative magnetic permeability of the material and c the speed of light in vacuum. The two different cases, $\epsilon_z < 0$ and $\epsilon_\perp < 0$, are respectively called type I and type II according to the number of directions that present a metallic behavior. Importantly, Fig. 4.1 shows that the phase velocity —parallel to $\mathbf{k}$— and the group velocity $\mathbf{v}_g$ are not generally aligned. Actually, $\mathbf{k}\cdot\mathbf{v}_g \to 0$ for high values of k. Also for large wavevectors, the propagation of these modes is highly directional: it happens at the fixed angle $\arctan(\epsilon_z/\epsilon_\perp)$ with the z direction. This property is a clear hint of the presence of hyperbolic modes, see Sec. 4.2 and particularly the insets in Fig. 4.4.

Interestingly too, the area of any isofrequency surface in $\mathbf{k}$ space is infinite, in contrast with that of the spheres corresponding to isotropic materials, so the density of states diverges when $k \to \infty$ at any fixed ω. Another quirk of these modes is that $\mathbf{k}\cdot\mathbf{E} \neq 0$, which directly follows from Maxwell's equations, similarly to what happens with other light-matter coupled modes as plasmons, see Ch. 2.

The limit $k \gg \omega/c$ simplifies the description of these modes but still preserves their main peculiarities. It allows to approximate the hyperbolic isofrequency surfaces by their asymptotic cone. In this case, $\mathbf{k} \parallel \mathbf{E}$ and $\mathbf{v}_g \cdot \mathbf{k} = 0$.

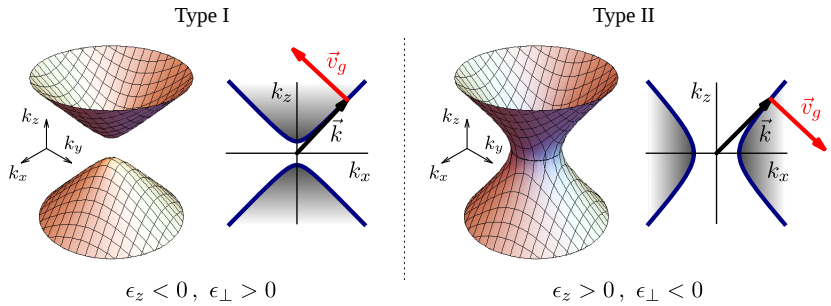

Figure 4.1: Isofrequency surfaces of the dispersion relation of extraordinary modes for type-I and -II hyperbolic materials. The 3D contours are presented together with a 2D section, where the direction of a wavevector $\mathbf{k}$ and its respective group velocity $\mathbf{v}_g$ —perpendicular to the surface— are drawn. The shadowed regions indicate where the left-hand side of Eq. (4.1) is greater than the right-hand side, which allows to determine the direction of $\mathbf{v}_g$.

All the foregoing differences with respect to isotropic materials encode a great deal of the exotic behavior of the extraordinary modes. As an example, since the high-momenta polaritons remain immune to evanescent decay, volume confinement of polaritons inside nanogranules is possible,[29,139,140] as well as near fields can penetrate hyperbolic materials and propagate barely damped. Also, the misalignment of the phase and group velocities results in negative refraction for certain setups. These facts together entail the ability to engineer lenses with sub-diffractional focusing[41,141] and super-resolution imaging similar to Pendry's proposal,[142] which is referred to as partial hyperlensing.[27,30,31,143] The aforementioned divergence of the density of states, although limited in practice by a maximum k of the order of the inverse lattice parameter, can be exploited in regard to applications, too. A strong enhancement of spontaneous emission of systems placed nearby and photoluminescence engineering stand out in this respect.[30]

Natural hyperbolic materials

The unusual properties of hyperbolic materials can be found in many different contexts. As an example, some ferromagnets,[144] magnetized plasmas,[145] layered superconductors[146,147] and liquid crystals[148] can be mentioned. As for the experimental realization of hyperbolic materials, *metamaterials* emerged as the first candidates. They consist of nano-engineered systems that combine metals and dielectrics to achieve the desired anisotropic $\hat{\epsilon}$.[30,149] Their main flaws are the technical difficulties encountered in their production and the large size of their unit cells ($\sim$ nm), which establishes a quite low cutoff for the wavevector of hyperbolic modes.

However, natural hyperbolic materials offer an alternative to these issues.

As is clear from their name, they do not require the combination with other materials to display the hyperbolic character. The change in sign of the dielectric constant in different directions can happen due to the light-matter coupling with anisotropic phonons.

For a crystal with a rotational symmetry axis, the resulting components of the dielectric tensor take the form[30,150]

$$\epsilon_w(\omega) = \epsilon_w(\infty)\frac{\omega_{LO,w}^2 - \omega^2}{\omega_{TO,w}^2 - \omega^2}\,, \tag{4.2}$$

with the subscript w referring to the principal axes, $w = \perp, z$, and $\omega_{LO(TO),w}$ to the frequencies of longitudinal (transverse) optical phonons in the w direction, respectively. The difference in these frequencies implies that, for certain ranges of ω —the so-called reststrahlen bands—, the material shows hyperbolic behavior, $\epsilon_\perp \epsilon_z < 0$.

Hexagonal boron nitride (hBN) is an example of such an anisotropic ionic crystal. Its layered structure, sketched in Fig. 4.2, results in $\hat{\epsilon}$ having two different eigenvalues, ϵ_z and $\epsilon_\perp$, corresponding to the out-of- and in-plane directions. The respective frequencies $\omega_{LO(TO),z(\perp)}$ and the high-frequency dielectric permittivities $\epsilon_w(\omega)$ have been experimentally measured. Ref. [29] reports the values

$$\omega_{LO,z} = 825\,\mathrm{cm}^{-1}\,, \qquad \omega_{LO,\perp} = 1614\,\mathrm{cm}^{-1}\,, \tag{4.3}$$

$$\omega_{TO,z} = 760\,\mathrm{cm}^{-1}\,, \qquad \omega_{TO,\perp} = 1360\,\mathrm{cm}^{-1}\,, \tag{4.4}$$

$$\epsilon_z(\infty) = 4.90\,, \qquad \epsilon_\perp(\infty) = 2.95\,, \tag{4.5}$$

which yields the $\epsilon_{z(\perp)}(\omega)$ plotted in Fig. 4.2. The two reststrahlen bands correspond to the aforementioned types I and II. They belong to the mid-infrared regime, which makes hBN a good prospect in regard to technological applications. Moreover, the ability to switch between both types by means of tuning the frequency is an extra feature that can be exploited.

Importantly, the observation of polaritons is at experimental reach, and actually numerous measurements have been reported.[29,40,41,139,141,151] As for the losses, they turn out to be much lower than for metals. Indeed, they have been neglected in Eq. (4.2), $\mathrm{Im}\,\epsilon$ being from 3 to 6 times lower than that of silver, reportedly one of the best plasmonic materials.[28]

All these considerations make hBN, already a well-known premier constituent of van der Waals heterostructures,[14,152] worth being studied in the realm of nano-optics. This chapter is devoted to the application of ray optics in this context.

4.2 Experimental background

In this section, we proceed to briefly summarize the experiment presented in Ref. [29], which reported remarkable results concerning radiation confinement through polaritons. At the same time, however, some aspects lacked

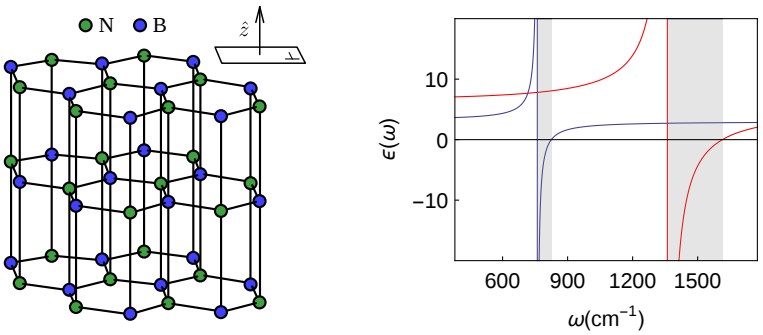

Figure 4.2: Left: crystal structure of hBN, consisting of stacked honeycomb layers. Right: ϵ_z (blue) and $\epsilon_\perp$ (red) of hBN. The lower ($760\,\mathrm{cm}^{-1} < \omega < 825\,\mathrm{cm}^{-1}$) and upper ($1360\,\mathrm{cm}^{-1} < \omega < 1614\,\mathrm{cm}^{-1}$) reststrahlen bands have been shadowed in gray.

more theoretical support and above all a clearer physical picture. Actually, this was the main inspiration of our work, which reproduces the experimental data and paves the way to apply unconventional ray optics to light-matter excitations.

The experiment was performed on arrays of hBN truncated cones (from now on simply referred to as cones) on a Si/SiO_2 substrate. Their periodicity allows the coupling of low-k far-field incident radiation to the greater wavevector of hyperbolic modes. An outline of the setup and an actual picture of a sample appear in Fig. 4.3. The fabrication consisted in electron-beam lithography on previously grown hBN crystals (cf. Ref. [29] for more details), so that the principal z axis of hBN is perpendicular to the surface of the substrate. 24 different samples were produced with this procedure, each of them with a different cone height, ranging from 80 to 410 nm.

The measured data is the optical reflectivity of the samples after the incidence of circularly-polarized radiation normal to, tilted ($\sim 25°$) and grazing ($\sim 70°$) the surface. Clear resonances, namely peaks in the reflection, appear in both reststrahlen bands. An example is shown in Fig. 4.3, and all the data is grouped in Fig. 4.4 together with some calculations presented in the experimental paper.

Several aspects of these measurements must be highlighted. First of all, the resonances are restricted to the reststrahlen bands, and they only happen when there is a significant projection of $\mathbf{E}$ in the metallic directions of hBN. The respective wavelengths vary from 17 (6) to 86 (61) times the height (diameter) of single cones, far beyond the diffraction limit. They show extraordinarily high quality factors $Q = \omega_{\mathrm{res}}/\Delta\omega_{\mathrm{res}}$ (with ω_{res} the resonant frequency and $\Delta\omega_{\mathrm{res}}$ the peak width) ranging from 66 (140) to 220 (235) in the upper (lower) reststrahlen band, well exceeding the theoretical maximum

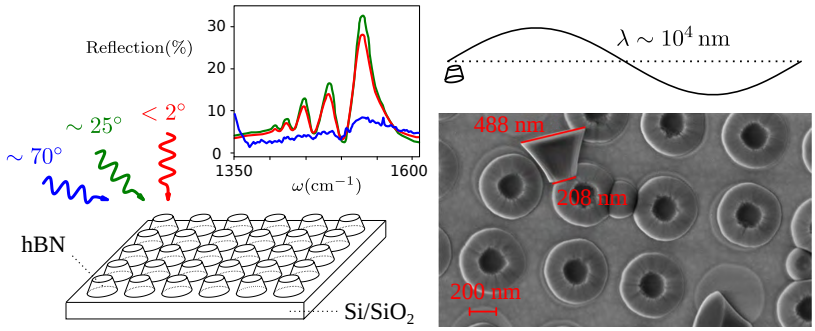

Figure 4.3: An outline of the experimental setup of Ref. [29] appears on the left, together with an actual top view on the right. The latter, obtained with a scanning electron microscope, shows some overturned cones from which the dimensions were extracted. An example of the data for a single array and frequencies in the upper reststrahlen band is given by the plot, clearly showing resonances. The legend is provided by the colored wavy arrows, which indicate the angles of incidence of radiation. At last, the scaled sketch of a cone together with an incident wavelength illustrates the high subwavelength nature of the resonances.

for plasmonics in Ag spheres[153] and other systems like SiC nanopillars.[154] Importantly, with the exception of the aspect ratio (namely diameter divided by height of single cones), the features that distinguish the samples do not affect the value of the resonant frequencies. That can be clearly seen in Fig. 4.4, since the markers respective to different setups cluster together. At last, finite-element calculations that simulate the reflection spectra show a highly directional pattern in the intensity of the electric field, see the insets of Fig. 4.4. All these facts point at hyperbolic modes as the ultimate cause of the resonances.

The theoretical results presented in Ref. [29] and summarized in Appx. C.1 reproduce the tendencies in frequency versus aspect-ratio plots. However, the field-intensity density plots suggest that a simpler physical picture might account for the resonances. Rather than a wavelike description, a particle perspective seems convenient in that respect. Indeed, ray optics emerges as the natural tool to tackle the problem. Besides providing with an extra interpretation of the aforementioned results, this procedure yields relevant information regarding the study of near-field experiments. In particular, Sec. 4.6 will show that field-intensity patterns can be easily interpreted by means of this formalism. Throughout this chapter, we proceed to discuss unconventional ray optics and its application to the reported experiment.

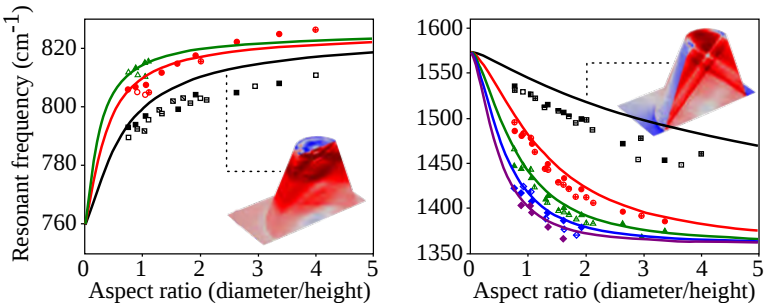

Figure 4.4: Measurements of the resonant frequency as a function of the aspect ratio of individual hBN cones. Different markers correspond to different samples with varying cone heights, and each color is respective to one peak in a reflectivity plot like that of Fig. 4.3. The curves depict the solutions of the electromagnetic problem of single ellipsoids instead of cones, cf. Appx. C.1 for details. The insets show the spatial distribution of $|\mathbf{E}|$ in the inside of an hBN cone for the resonances indicated with dotted lines. These results were obtained by finite-element calculations. In the color scale, blue (red) corresponds to low (high) values of the electric field. A remarkable cross-hatch pattern reveals the hyperbolic character of the underlying modes.

4.3 Hamiltonian optics in hBN

According to the discussion of the previous section, the consideration of a single ellipsoidal nanogranule embedded in vacuum suffices to account for the most relevant aspects of the experimental measurements. Recall also that due to the fabrication process, the symmetry axis is assumed to be aligned with the z principal axis of the dielectric tensor. We will focus on such a system henceforth, and carry out its study from the perspective of classical mechanics. In this section, we proceed to establish the connection between the wave and particle behaviors, paving the way to the application of the semi-classical methods of Secs. 4.4 and 4.5 and aiming at a more comprehensive interpretation of the resonances.

4.3.1 The optical Hamiltonian

Ray optics establishes a connection between Fermat's and Hamilton's principles, or equivalently between ray and particle dynamics. It is primarily based upon the resolution of Maxwell's equations in the limit of vanishing wavelengths, the so-called eikonal approximation.[155] Combined with the general ansatz

$$\mathbf{E}(\mathbf{r},t) = \mathbf{E}_0(\mathbf{r})e^{-i\omega t}\,, \qquad \mathbf{E}_0(\mathbf{r}) = \mathbf{e}(\mathbf{r})\exp\left[ik_0 S(\mathbf{r})\right]\,, \qquad k_0 = \omega/c\,, \quad (4.6)$$

with analogous expressions for $\mathbf{B}(\mathbf{r},t)$, it results in a condition for the spatial phase $S(\mathbf{r})$, namely the eikonal equation. Importantly, the latter encodes all the phenomenology of geometrical optics.

This formalism can also be applied to hyperbolic materials. An analogous procedure to that of conventional optics yields the eikonal equation

$$\left[(\nabla S)^2 - \epsilon_\perp \mu\right]\left[\epsilon_\perp\left(S_x^2 + S_y^2\right) + \epsilon_z S_z^2 - \epsilon_\perp \epsilon_z \mu\right] = 0\,, \tag{4.7}$$

where $S_w = \partial S/\partial w$, $w = x, y, z$. The first factor corresponds to an ordinary ray, characteristic of isotropic media, whereas the second is respective to extraordinary modes, namely phonon-polariton collective modes. Henceforth, we will focus on the last term, further approximated to only retain long-wavevector solutions —the hallmark of hyperbolic behavior—, and refer to the eikonal equation simply as

$$\epsilon_\perp\left(S_x^2 + S_y^2\right) + \epsilon_z S_z^2 \simeq 0\,. \tag{4.8}$$

Eq. (4.8) directly builds a bridge between the electromagnetic problem and classical mechanics. Actually, it is the Hamilton-Jacobi equation at zero energy of the *optical* Hamiltonian

$$H = \epsilon_x p_x^2 + \epsilon_y p_y^2 + \epsilon_z p_z^2\,, \tag{4.9}$$

which in turn corresponds to a fictitious free particle with anisotropic masses given by $m_i = 1/(2\epsilon_i)$, $i = x, y, z$, some of which are negative. A great deal of the unconventional behavior of this system is precisely encoded by this fact, as will be shown subsequently.

Importantly, the knowledge of the equations of motion respective to this Hamiltonian is tantamount to the resolution of the eikonal equation, and further provides the sought particle-like picture of the resonances as constructively interfering trajectories. On the other hand, the formalism of Hamiltonian mechanics allows to play upon conservation theorems, see Sec. 4.3.2, that greatly simplify the problem. This is the approach that we will adopt and discuss henceforth from the perspectives of the Einstein-Brillouin-Keller method in Sec. 4.4 and the Gutzwiller's approach in Sec. 4.5.

4.3.2 Ellipsoidal coordinates and conserved quantities

Due to the geometry of the problem, we are interested in the study of the optical Hamiltonian in ellipsoidal coordinates. Considering a prolate ellipsoid with semi axes $a_\perp$ and a_z, they can be defined as

$$\left.\begin{aligned} x &= b\sqrt{|\epsilon_\perp|}\sin\xi\sin\theta\cos\psi \\ y &= b\sqrt{|\epsilon_\perp|}\sin\xi\sin\theta\sin\psi \\ z &= b\sqrt{|\epsilon_z|}\cos\xi\cos\theta \end{aligned}\right\}\,, \qquad b \equiv \sqrt{\frac{a_\perp^2}{|\epsilon_\perp|} + \frac{a_z^2}{|\epsilon_z|}}\,, \tag{4.10}$$

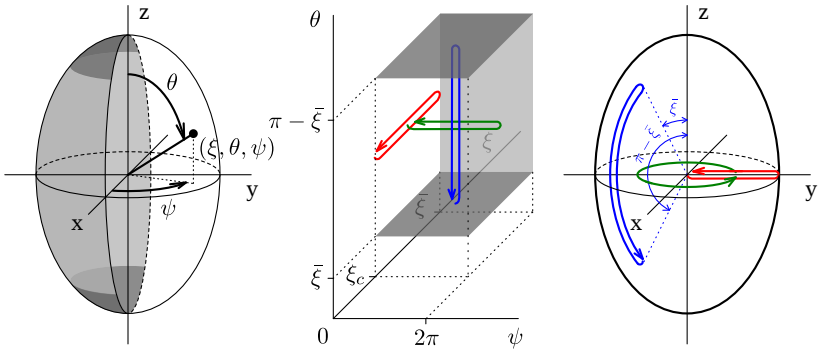

Figure 4.5: Left and center: outlines of the ellipsoidal coordinates inside the spheroid. The boundary, depicted in light and dark gray, corresponds to $\{(\xi,\theta,\psi)\,|\,\xi = \bar{\xi}\}$ and $\{(\xi,\theta,\psi)\,|\,\theta = \bar{\xi}$ or $\theta = \pi - \bar{\xi}\}$. Only half of it appears in the left outline for the sake of clarity. Center and right: in colors, independent trajectories used to define the integration paths of Sec. 4.4 and the action variables of Sec. 4.5.1. In both cases, red, blue and green are associated to the ξ, θ and ψ coordinates, respectively.

for the inside region, with the radial coordinate $0 < \xi < \bar{\xi}$ and

$$\tan\bar{\xi} = a_\perp/a_z\sqrt{|\epsilon_z/\epsilon_\perp|}\,, \tag{4.11}$$

and the polar and azimuthal variables $\bar{\xi} < \theta < \pi - \bar{\xi}$, $0 < \psi < 2\pi$. An outline appears in Fig. 4.5.

After rescaling by an overall factor, the optical Hamiltonian takes the form

$$H = \frac{p_\theta^2 - p_\xi^2}{\sin^2\theta - \sin^2\xi} - \frac{p_\psi^2}{\sin^2\theta\sin^2\xi} = 0\,. \tag{4.12}$$

Recall from the previous section that we are only interested in solutions with zero energy, hence the last equality. The fact that H is separable and therefore integrable entails the existence of three independent conserved quantities. It is straightforward to identify the energy $E = H$ and the angular momentum around the z axis $l_z = p_\psi$ as such. The third one,

$$l_{12} = p_\theta^2 + \frac{l_z^2}{\sin^2\theta} - E\sin^2\theta = p_\xi^2 + \frac{l_z^2}{\sin^2\xi} - E\sin^2\xi\,, \tag{4.13}$$

corresponds to the product of the angular momentum with respect to the two foci of the ellipsoid.

Restricting ourselves to the case of interest, $E = 0$, the momenta can be expressed as a function of the position coordinates and the conserved

quantities as

$$p_\Omega = \pm|l_z|\sqrt{\frac{1}{\sin^2\xi_c} - \frac{1}{\sin^2\Omega}}\,, \qquad p_\psi = l_z\,, \tag{4.14}$$

for $\Omega = \xi, \theta$. We have defined

$$\xi_c = \arcsin\sqrt{l_z^2/l_{12}}\,, \tag{4.15}$$

which is the radial coordinate of the caustic and determines the classically accessible regions inside the ellipsoid, if any: provided that $0 < \xi_c < \bar{\xi}$, the momenta p_ξ, p_θ are real in the region $\xi_c \leq \xi \leq \bar{\xi}$, $\bar{\xi} \leq \theta < \pi - \bar{\xi}$. Conversely, if ξ_c exceeds $\bar{\xi}$, p_ξ and p_θ acquire imaginary values.

These expressions encode the full solution of the dynamics of the system, actually yielding the explicit expressions for the trajectories in the phase diagram, and will be used throughout this chapter.

4.3.3 The effective surface Hamiltonian

An analogous analysis to that of Sec. 4.3.2 can be performed for the outside region of the prolate ellipsoid. The only changes to consider are the eikonal equation, now respective to vacuum, and a different definition of the ellipsoidal coordinates, namely

$$\left.\begin{aligned} x &= a\sinh\eta\sin\theta\cos\psi \\ y &= a\sinh\eta\sin\theta\sin\psi \\ z &= a\cosh\eta\cos\theta \end{aligned}\right\}\,, \qquad a = \sqrt{a_z^2 - a_\perp^2}\,, \tag{4.16}$$

with the radial parameter $\eta > \bar{\eta}$,

$$\tanh\bar{\eta} = a_\perp/a_z\,, \tag{4.17}$$

and the angular coordinates $0 < \theta < \pi$, $0 < \psi < 2\pi$. With the same rescaling as in Eq. (4.12), the optical Hamiltonian at $E = 0$ takes the form

$$H = \frac{p_\eta^2 + p_\theta^2}{\cosh^2\eta - \cos^2\theta} + \frac{p_\phi^2}{\sinh^2\eta\sin^2\theta} = 0\,. \tag{4.18}$$

At last, the radial momentum is now

$$p_\eta = \pm i|l_z|\sqrt{\frac{1}{\sin^2\xi_c} + \frac{1}{\sinh^2\eta}}\,, \tag{4.19}$$

whereas p_θ and p_ψ remain the same as in Eqs. (4.14).

The condition that yields surface modes corresponds to p_ξ and p_η being purely imaginary, so that field intensities decay away from the interface.

As is proved in Appx. C.2, this consideration together with the contour conditions at the interface yield

$$i\sqrt{\epsilon_\perp}\sqrt{\epsilon_z}p_\xi = p_\eta\,. \tag{4.20}$$

The effective surface Hamiltonian H_S can then be obtained combining Eqs. (4.12), (4.18) and (4.20):

$$H_S = \frac{p_\theta^2}{\sin^2\theta - \sin^2\xi_c} - \frac{p_\psi^2}{\sin^2\xi_c \sin^2\theta}\,, \tag{4.21}$$

with the definition

$$\frac{1}{\sin^2\xi_c} = \frac{1}{\epsilon_\perp\epsilon_z - 1}\left(\epsilon_\perp\epsilon_z\frac{1}{\sin^2\bar{\xi}} + \frac{1}{\sinh^2\bar{\eta}}\right)\,. \tag{4.22}$$

This formula, valid for surface waves, replaces Eq. (4.15), which only applies to bulk modes. E and l_z being the conserved quantities now, Eqs. (4.14) still hold for θ and ψ.

4.4 EBK method

As we discussed in the introduction, semiclassical physics builds a bridge between the classical and quantum regimes, or equivalently between wave and particle —or ray— dynamics. The Bohr-Sommerfeld conditions were the first foray into this field, soon after completed by the deeper insight of the Wentzel–Kramers–Brillouin (WKB) approximation.[156,157] However, it was not till the development of the EBK method[158–160] that a fully-fledged formalism was devised. Conceived as a procedure to find the asymptotic solutions —i.e., the large eigenvalues and their eigenvectors— of boundary problems for partial differential equations, its validity is general to the extent of quasiperiodic systems.[161]

In this section, however, it will be applied to the simplest case, namely the regular system featured in Sec. 4.3. It will reveal itself as a relatively simple method to reproduce the spectrum of the polaritonic resonances described previously. Together with the alternative perspective of Sec. 4.5, more physical insight in their interpretation will be provided as well.

Eqs. (4.14) specify a hypersurface in the six-dimensional phase space that has the topology of a three-dimensional torus.[157,162] Three independent loops can be chosen in such a geometry, each one associated to a single ellipsoidal coordinate, see Fig. 4.5. Then, according to the EBK rules, the total phase acquired along any of them is an integer multiple of 2π. A shift of $-\pi/2$ upon crossing the caustic and also the reflection phase shift(s) δ at the boundary, with

$$\tan\frac{\delta}{2} = \frac{i}{\sqrt{\epsilon_\perp}\sqrt{\epsilon_z}}\left(\frac{\sin^{-2}\xi_c + \sin^{-2}\bar{\eta}}{\sin^{-2}\xi_c - \sin^{-2}\bar{\xi}}\right)^{1/2}\,, \tag{4.23}$$

must be taken into account.[159] This last result is derived in Appx. C.2 by imposing the continuity of the potential and the normal component of $\mathbf{D}$ at the interface.

The EBK quantization conditions take the form

$$2\int_{\xi_c}^{\bar{\xi}} |p_\xi|\, d\xi - \frac{\pi}{2} + \delta = 2\pi\nu\,, \qquad \int_{\bar{\xi}}^{\pi-\bar{\xi}} |p_\theta|\, d\theta - \delta = \pi\lambda\,, \qquad l_z = \mu\,. \tag{4.24}$$

Without loss of generality, the quantum numbers (ν, λ, μ) can be taken to be non-negative integers. The two first equations can be rewritten in terms of elementary functions as

$$2\varphi(\bar{\xi}, \xi_c) - \frac{\pi}{2} + \delta = 2\pi\nu\,, \qquad 2\varphi\left(\frac{\pi}{2}, \bar{\xi}\right) - \delta = \pi\lambda\,, \tag{4.25}$$

having defined

$$\varphi(\xi, \xi_c) = \mu\int_{\xi_c}^{\xi} \sqrt{\frac{1}{\sin^2\xi_c} - \frac{1}{\sin^2\xi'}}\, d\xi' = \frac{\mu}{\sin\xi_c} A(\xi, \xi_c) - \mu B(\xi, \xi_c)\,, \tag{4.26}$$

$$A(\xi, \xi_c) = \arccos\left(\frac{\cos\xi}{\cos\xi_c}\right)\,, \qquad B(\xi, \xi_c) = \arccos\left(\frac{\cot\xi}{\cot\xi_c}\right)\,. \tag{4.27}$$

The resolution of these conditions can be carried out as follows. Combining Eqs. (4.25), we obtain the expression for ξ_c,

$$\sin\xi_c = \frac{\mu}{2\nu + \lambda + \mu + 1/2}\,. \tag{4.28}$$

Then, with ξ_c fixed by the quantum numbers (ν, λ, μ), δ given by Eq. (4.23) and $\bar{\eta}$ by Eq. (4.17), Eqs. (4.25) can be solved numerically for $\bar{\xi}$. At last, the final solution for the resonant frequencies ω can be determined from $\bar{\xi}$ by means of Eq. (4.11).

Comparing Eqs. (4.25)-(4.28) with the exact solution in the asymptotic limit,[159,163] the correspondence between the EBK quantum numbers (ν, λ, ν) and the indices of the exact solution (l, m, n) —cf. Appx. C.1— can be established:[164]

$$l = 2\nu + \lambda + \mu\,, \qquad m = \mu\,, \qquad n = \nu\,. \tag{4.29}$$

These relations allow to identify the $\nu > 0$ and $\nu = 0$ solutions as the bulk and surface modes, respectively: the scalar potential of the former oscillates inside the granule along the radial direction ξ, whereas that of the latter monotonically increases with ξ and reaches a maximum at the surface.[165]

To compare the EBK results with the experimental data, we calculated the eigenmode spectra of an hBN spheroid as a function of its aspect ratio. The measured optical constants of hBN, Eq. (4.5), were used neglecting the

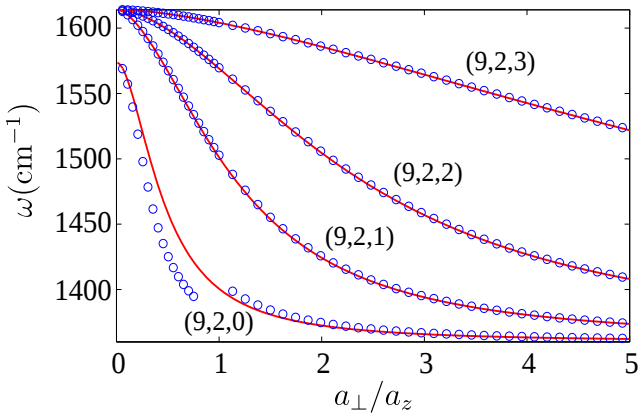

Figure 4.6: Eigenfrequencies of polariton modes in an hBN spheroid as a function of the aspect ratio $a_\perp/a_z$. The red lines are exact solutions of Eq. (C.6), whereas the blue circles are obtained by the EBK method. The indices (l, m, n), with $n = 0$ and $n > 0$ denoting surface and bulk modes, respectively, label the curves according to Eqs. (4.24) and (4.30). For the $(9, 2, 0)$ branch, which is classified as a surface mode, the left (right) blue circles correspond to the surface (bulk) EBK quantization method.

damping in order to obtain real solutions for ω. Examples of these calculations are shown in Fig. 4.6. EBK solutions are expected to be asymptotically exact at large quantum numbers but as one can see in the figure, an excellent agreement is already reached for the bulk modes for modest values of (l, m, n). On the other hand, some surface modes show considerable deviations from the exact result at intermediate aspect ratios. We discuss such modes in more detail below.

4.4.1 Surface modes

The hyperbolic surface modes (HSM)[166] are similar[167] to Dyakonov surface waves[168–170] of uniaxial materials with a positive-definite permittivity tensor. However, the HSMs have several new properties. Unlike the standard Dyakonov waves, the momenta and therefore the achievable degree of confinement for the HSM are limited only by the microscopic (for hBN, atomic) structure. The HSM are robust to surface defects in the sense that there can only be three other fixed directions for the defect-scattered wave. This is a stronger angular restriction than the absence of electron backscattering in topological insulators[110] and graphene.[4] Finally, compared to surface plasmons in metals, which lack any directionality, the HSM of polar insulators should exhibit a much lower damping as they are free of electronic losses.

In the present case of the spheroid, the HSMs correspond to the EBK

quantum numbers $\nu = 0$ (and so to $n = 0$), and the EBK rules for the angular coordinates take the form

$$2\int_{\bar{\xi}}^{\pi-\bar{\xi}} |p_\theta| d\theta = -\pi(2\lambda - 1)\,, \qquad p_\psi = \mu\,. \tag{4.30}$$

According to Eq. (4.28), the ξ coordinate of the caustic is now given by

$$\sin\xi_c = \frac{m}{l+1/2} = \frac{\mu}{\lambda+\mu+1/2}\,, \tag{4.31}$$

and the calculation of the resonant frequencies is performed as described previously.

While the assumption of a spheroidal granule simplifies the theoretical analysis, one may ask if it is possible to make some correspondence between such a theory and the available experiments that were all done with HM samples of non-spheroidal shapes. Our tentative answer is as follows. The modes observed in truncated hBN nanocones,[29] which were originally called 'volume-confined' are, in fact, similar to a subset of our HSM, specifically $(l, m, n) = (l, 0, 0)$ and $(l, 1, 0)$ modes. The modes of cuboidal hyperbolic metamaterials[140] and hBN slabs[40,41] are conceptually similar to our bulk modes. However, indexing them with l, m or n would be tenuous as the conserved quantities in such systems are considerably different from those of prolate spheroids (for example, translational momenta in slabs versus angular momenta in spheroids).

4.5 Periodic orbits

Classical dynamics can prominently impact the structure of quantum energies and quantum wavefunctions.[171] In particular, the latter may contain enhanced intensity lines along these classical trajectories, as well as the discrete spectrum can be understood as stemming from the energies of the simplest —generally the shortest— of all periodic paths. Constructively interfering with themselves, these are supposed to give rise to the resonances of the experiment described in Sec. 4.2.

Throughout this section, we proceed to study the closed orbits of the optical Hamiltonian. For that purpose, we will first perform a canonical transformation to the action-angle variables. Then, the distribution of the energies of the shortest orbits as a function of the aspect ratio will be analyzed. At that point, the clustering of topologically similar orbits will emerge as the underlying cause of the existence of discrete resonances. Each of them will be associated to a characteristic shape and provided with the physical picture of a constructively interfering closed orbit. Sec. 4.6 will prove the relevance of this analysis by explaining the intensity patterns of a simulated near-field experiment in terms of the found trajectories.

4.5.1 Action-angle variables

To study the classical periodic orbits of the polaritons, it is convenient to perform a canonical transformation to action-angle variables,[162,172] with no need to explicitly solve the equations of motion. Being n the number of degrees of freedom, $\mathbf{q} = (q_1, \ldots, q_n)$ the position variables and $\mathbf{p} = (p_1, \ldots, p_n)$ their conjugate momenta, the actions are defined as

$$J_i = \oint_{P_i} d\mathbf{q} \cdot \mathbf{p}(\mathbf{q}, C_1, \ldots, C_n)\,, \qquad i = 1, \ldots, n\,, \tag{4.32}$$

where all the considered paths $\{P_i \,|\, i = 1, \ldots, n\}$ must be independent. C_i with $i = 1, \ldots, n$ denote the conserved quantities. We will refer to the angle variables as θ_i.

In our case, $n = 3$, $\{C_1, C_2, C_3\} = \{E, l_z, l_{12}\}$ and the integration paths are depicted in Fig. 4.5. Using Eqs. (4.14), the action variables are

$$\left.\begin{aligned} J_\xi &= 2\int_{\xi_c}^{\bar\xi} d\xi\, p_\xi = 2|l_z| \int_{\xi_c}^{\bar\xi} d\xi \sqrt{\tfrac{1}{\sin^2\xi_c} - \tfrac{1}{\sin^2\xi} + \tfrac{E}{l_z^2}\sin^2\xi}\,, \\ J_\theta &= 2\int_{\bar\xi}^{\pi-\bar\xi} d\theta\, p_\theta = 2|l_z| \int_{\bar\xi}^{\pi-\bar\xi} d\theta \sqrt{\tfrac{1}{\sin^2\xi_c} - \tfrac{1}{\sin^2\theta} + \tfrac{E}{l_z^2}\sin^2\theta}\,, \\ J_\psi &= \int_0^{2\pi} d\psi\, p_\psi = 2\pi l_z\,. \end{aligned}\right\} \tag{4.33}$$

An orbit on an invariant torus in phase space is periodic (closed) if the ratios of the individual frequencies of motion ν_i respective to the action-angle coordinates are rational numbers. These can be calculated as

$$\nu_i = \frac{\partial H}{\partial J_i} = \left|\frac{\partial(E, J_j, J_k)}{\partial(J_\xi, J_\theta, J_\psi)}\right| = \left|\frac{\partial(E, J_j, J_k)}{\partial(E, l_z, l_{12})}\right| \Bigg/ \left|\frac{\partial(J_\xi, J_\theta, J_\psi)}{\partial(E, l_z, l_{12})}\right|\,, \tag{4.34}$$

with $\{i, j, k\} = \{\xi, \theta, \psi\}$. When setting $E = 0$, the primitives of the integrals are elementary functions, and the ratios of the frequencies can be expressed as

$$\nu_\xi : \nu_\theta : \nu_\psi = \pi - 2A : -A : (B - A)\,\mathrm{sign}(l_z)\,, \tag{4.35}$$

where $A = A(\bar\xi, \xi_c)$ and $B = B(\bar\xi, \xi_c)$ are defined by Eqs. (4.27).

To get a particular periodic orbit, we follow these steps. First, we fix the frequency ratios as two rational numbers. Next, we determine A and B consistent with this choice and we solve for $\bar\xi$ and ξ_c with Eqs. (4.27). Finally, the resonant frequency ω is obtained from Eq. (4.11), and the orbit is generated and plotted using Eqs. (4.14).

According to Sec. 4.3.3, there are surface modes with imaginary p_ξ described by the effective surface Hamiltonian H_S. The analysis of these periodic orbits is analogous but simpler because there is only one frequency ratio,

$$\nu_\psi : \nu_\theta = 1 - \frac{1}{\sin\xi_c}\,. \tag{4.36}$$

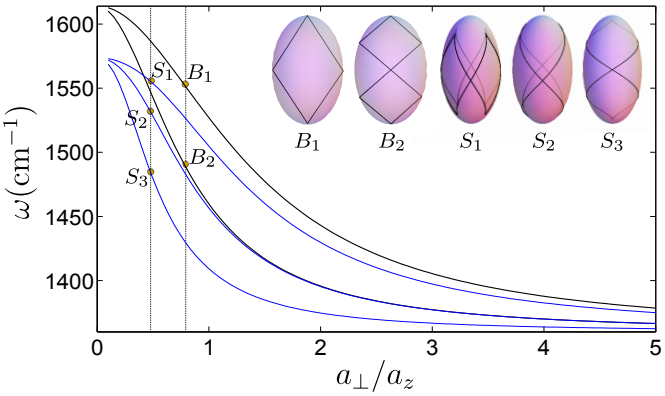

Figure 4.7: Frequencies of representative periodic orbits as a function of the spheroid aspect ratio. Black lines are respective to the bulk orbits B_1 and B_2, with frequency ratios $|\nu_\xi| : |\nu_\theta| : |\nu_\psi| = 2:1:0$ and $4:1:0$, respectively. Blue lines correspond to the surface orbits S_1, S_2 and S_3, with $|\nu_\theta| : |\nu_\psi| = 2:1$, $1:1$ and $1:2$. The insets depict them inside the granule. For the surface cases, they include all the orbits of the given type passing through the equatorial point facing the viewer: two for S_1 and S_2 and one for S_3.

ω is now obtained by means of Eq. (4.22). Closed orbits like the S_1-S_3 insets in Fig. 4.7 are obtained when this quotient is a rational number. Inserting Eq. (4.31) in Eq. (4.36), it can be seen that roughly a quarter of all possible HSM periodic orbits are simultaneously EBK eigenmodes.

4.5.2 Gutzwiller's trace formula and clustering of the orbits

In this section, we proceed to discuss the expected relation between classical periodic orbits and a quantized spectrum, which in the experiment corresponds to the discrete resonant frequencies.

According to the trace formulas given by Gutzwiller[171] for chaotic Hamiltonian systems and by Berry and Tabor[173] for integrable ones,

$$n(E) = n_{\mathrm{TF}}(E) + \frac{2}{\hbar^{(N+1)/2}} \sum_{\mathbf{M}} \frac{\cos\{2\pi \mathbf{M}\cdot[(\mathbf{C}_\mathbf{M}/\hbar) - \frac{1}{4}\alpha_\mathbf{M}] + \frac{1}{4}\pi\beta_\mathbf{M}\}}{|\mathbf{M}|^{(N-1)/2}|\nu(\mathbf{C}_\mathbf{M})|\sqrt{|K(\mathbf{C}_\mathbf{M})|}}\,, \tag{4.37}$$

the density of states (DOS) $n(E)$ of the quantized eigenmodes can be represented by a sum over the periodic orbits added to the Thomas-Fermi (TF) value. $\mathbf{M}$ is a nonzero vector with non-negative integer components whose ratios are those of Eqs. (4.35) or (4.36), thus encoding the topology of the corresponding orbit. $\mathbf{C}_\mathbf{M}$ and $\nu(\mathbf{C}_\mathbf{M})$ are vectors containing the conserved quantities and frequencies described in Sec. 4.5.1, respectively. Finally, $\alpha_\mathbf{M}$

is a vector whose components are the number of caustics encountered in the oscillation along each coordinate, $\beta_{\mathbf{M}}$ is the excess of positive over negative eigenvalues of the matrix $\nu \cdot \partial^2 \mathbf{C}/\partial\theta_i \partial\theta_j$ and $K(\mathbf{C_M})$ is the scalar curvature of the energy contour, defined in Ref. [173].

In the present case of the indefinite Hamiltonian, although the ray dynamics in a spheroidal particle is of course integrable, the DOS diverges without a momentum cutoff. As a consequence, carrying out the summation in the Berry-Tabor formula, one should get infinity not only at some discrete frequencies that are equal to the measured resonant values, but in fact at all frequencies in the reststrahlen band. The treatment of these divergences is an intriguing problem yet to be studied. For this reason, we will restrict ourselves to a qualitative discussion of the trace formula, which will still provide relevant information.

In general, the orbits can have very complicated shapes. At a first glance, their dispersion relations (ω versus the aspect ratio) cover a great part of the reststrahlen bands rather than producing the expected discrete spectrum, cf. Sec. 4.2. However, a more careful analysis allows the classification of orbits in groups to tackle this problem. In this respect, although Eq. (4.37) will not be rigorously applied, its qualitative analysis suggests the breakdown of the density of states in contributions that can be associated to a common topology, instead of focusing on single orbits. Then, a partial summation approximation over the simplest and shortest shapes would account for the spectrum structure.

Roughly speaking, $|\nu_\psi/\nu_\theta|$ is the relevant quantity labeling the topology of any orbit. It represents the ratio of the winding numbers along the polar and azimuthal angles after one cycle. On the other hand, $|\nu_\xi|$ fixes the oscillation frequency in the radial direction, and in turn determines the typical radial distance of the orbit from the center of the spheroid. As $|\nu_\xi|$ increases, the orbit is pushed towards the surface of the spheroid. In the limit $|\nu_\xi| \to \infty$, it becomes a smooth trajectory grazing along the boundary, similarly to what happens with the whispering gallery modes well known in ray optics and acoustics.

Fig. 4.8 (left) illustrates this classification. Orbits sharing the same $|\nu_\psi/\nu_\theta|$ show the same topology and appear grouped under a same class. Remarkably, as the right plot of the figure shows, the dispersion relations of all the orbits belonging to a single class converge to a curve. Actually, this clustering can be interpreted as the underlying cause of the spectrum discreteness. Fig. 4.9 (right) shows another example with more orbits, having fixed the aspect ratio for the sake of clarity.

In general, the groups of orbits with the simplest $\mathbf{M}$, and therefore the shortest length, are expected to reproduce the resonant frequencies like the ones reported in Sec. 4.2. In our case, $|\nu_\psi/\nu_\theta|$ yields the different topologies and roughly determines the orbit length —cf. Fig. 4.8 (left)—, whereas ν_ξ labels the different orbits that belong to each of these classes. Therefore,

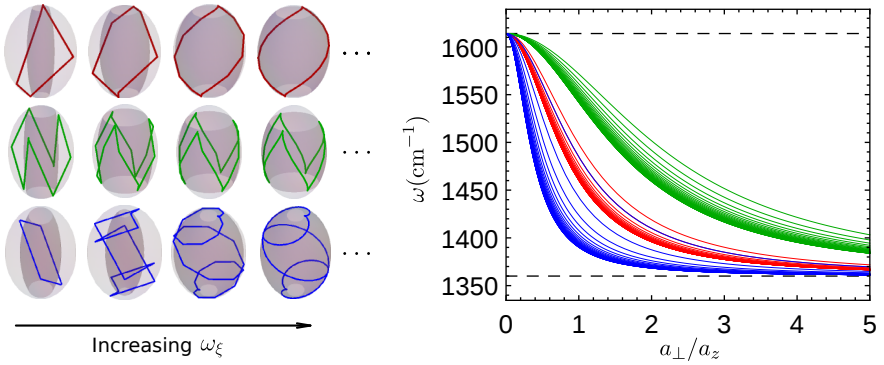

Figure 4.8: Left: periodic orbits for different values of ν_ξ, ν_θ, and ν_ψ. Red, green and blue correspond to $|\nu_\psi/\nu_\theta| = 1$, $1/3$ and 3, respectively. $|\nu_\xi|$ increases from left to right, making the caustic —darker surface— approach the boundary and yielding smoother orbits. The value of $|\nu_\xi/\nu_\psi|$ could be inferred from the number of radial bounces that occur during one azimuthal cycle. Right: dispersions (electromagnetic field frequencies) of the periodic orbits as a function of the aspect ratio of the granule. Sharing the legend with the left, the curves respective to the 40 first integer values of $|\nu_\xi|/(2\pi)$ have been plotted. As $|\nu_\xi|$ increases, the distance between adjacent curves associated to the same topology decreases. The $|\nu_\xi| \to \infty$ limit corresponds to whispering gallery trajectories grazing along the surface of the granule.

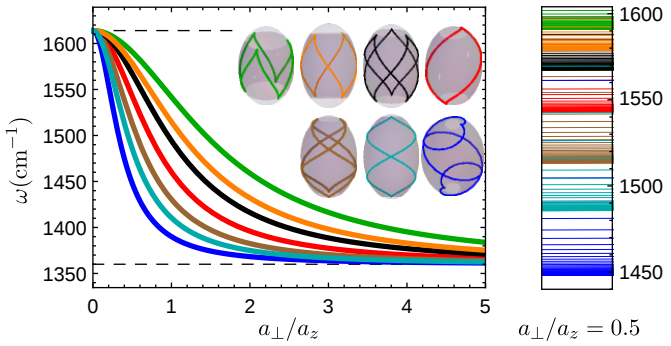

Figure 4.9: Left: frequencies of the whispering gallery periodic orbits as a function of the aspect ratio. The orbits have frequency ratios $|\nu_\psi/\nu_\theta| = i/j$ with $\{i, j\} \subset \{1, 2, 3\}$, whose values can be inferred comparing the winding numbers around the polar and azimuthal angles. The insets depict the shape of the orbits grazing the surface of a granule and provide the color legend. Right: discretization of the spectrum —cf. Fig. 4.8— at a fixed aspect ratio for all the orbit classes depicted on the left.

retaining only the simplest values of $|\nu_\psi/\nu_\theta|$, it seems convenient to perform a partial summation in Eq. (4.37) concerning the component of $\mathbf{M}$ respective to the ξ coordinate. These considerations motivate Fig. 4.9, which plots the limiting dispersion relation of these groups, namely those with $|\nu_\psi/\nu_\theta| = i/j$ and $\{i, j\} \subset \{1, 2, 3\}$. As Sec. 4.6 will show, the shapes depicted as insets predict the patterns in the field intensities to be observed in near-field experiments.

4.6 Response to a dipole

A peculiar property of the spheroid is that the dipole moment of all $m > 1$ modes exactly vanishes, and so they have extremely weak coupling to far-field radiation. Furthermore, while the dipole moment of the bulk modes is nonzero, it is quite small. Detection of all such modes in conventional optics experiments would be challenging.[29] However, the observation of these modes may be possible using scanning near-field optical microscopy. This technique uses a sharp metal tip to perturb and measure the system response locally. Crudely, one can model the tip as a point dipole and the measured signal as the electric field created by the system at the location of such a dipole, see Refs. [174–176] and citations therein.

In this section, we calculate the field created by the nanogranule in response to a nearby oscillating electric dipole. This way, we will show that the analysis performed throughout this chapter in terms of Hamiltonian optics yields more than a mere interpretation of the experimental results of

Sec. 4.2. Actually, the resulting field intensities will be predicted from the classical orbits previously featured.

We assume that the dipole is located at a point $\mathbf{R}$ in the $x-z$ plane. Let the spheroidal coordinates of $\mathbf{R}$ be $(\eta_0, \theta_0, 0)$ with $\eta_0 > \bar{\eta}$. The local direction of the coordinate lines is specified by the unitary vectors $\hat{\eta}$, $\hat{\theta}$ and $\hat{\psi}$, which are normal to the surfaces given by η, θ and ψ constant, respectively. The dipole moment $\mathbf{d}$ is also assumed to lie in the $x-z$ plane, $\mathbf{d} = d_\eta \hat{\eta} + d_\theta \hat{\theta}$, with $\hat{\eta}$ and $\hat{\theta}$ evaluated at $(\eta, \theta) = (\eta_0, \theta_0)$.

Following the notation in Appx. C.1, the scalar potentials inside and outside the spheroid will be denoted by $\Phi_1(\mathbf{r})$ and $\Phi_2(\mathbf{r})$, respectively, and the potential of the dipole alone, by $\Phi_d(\mathbf{r})$. They can be expanded in series of the spheroidal harmonics $Y_l^m(\theta, \psi) = P_l^m(\cos\theta)\cos(m\psi)$ as[165,177]

$$\Phi_1 = \sum_{l=0}^{\infty} \sum_{m=0}^{l} D_l^m t_l^m P_l^m(\cos\xi) Y_l^m(\theta, \psi) \quad \text{for } \xi < \bar{\xi}\,, \tag{4.38}$$

$$\Phi_2 = \sum_{l=0}^{\infty} \sum_{m=0}^{l} D_l^m r_l^m Q_l^m(\cosh\eta) Y_l^m(\theta, \psi) + \Phi_d \quad \text{for } \eta > \bar{\eta}\,, \tag{4.39}$$

$$\Phi_d = \sum_{l=0}^{\infty} \sum_{m=0}^{l} D_l^m P_l^m(\cosh\eta) Y_l^m(\theta, \psi) \quad \text{for } \eta < \eta_0\,. \tag{4.40}$$

The expansion coefficients D_l^m of Φ_d can be derived from the known expansion coefficients C_l^m of the potential of a point charge,[178]

$$D_l^m = \mathbf{d} \cdot \partial_{\mathbf{R}} C_l^m = (d_\eta \partial_{\eta_0} + d_\theta \partial_{\theta_0}) C_l^m\,, \tag{4.41}$$

$$C_l^m(\mathbf{R}) = \frac{\epsilon_m}{a} i^m (2l+1) \left[\frac{(l-m)!}{(l+m)!}\right]^2 Q_l^m(\cosh\eta_0) P_l^m(\cos\theta_0)\,, \tag{4.42}$$

where ϵ_m is the Neumann factor: $\epsilon_0 = 1$, $\epsilon_m = 2$ for m a positive integer. We obtain

$$D_l^m = \frac{\epsilon_m}{a} i^m (2l+1) \left[\frac{(l-m)!}{(l+m)!}\right]^2 \Big[d_\eta \partial_{\eta_0} Q_l^m(\cosh\eta_0) P_l^m(\cos\theta_0) + \\ + d_\theta Q_l^m(\cosh\eta_0) \partial_{\theta_0} P_l^m(\cos\theta_0) \Big]\,. \tag{4.43}$$

Imposing the continuity of the normal component of the vector displacement at the surface, Eq. (C.5), we get the matrix equation for the series coefficients:

$$\mathcal{M} \begin{pmatrix} t_l^m \\ r_l^m \end{pmatrix} = \begin{pmatrix} P_l^m(\cosh\bar{\eta}) \\ \partial_{\bar{\eta}} P_l^m(\cosh\bar{\eta}) \end{pmatrix}\,, \tag{4.44}$$

where

$$\mathcal{M} = \begin{pmatrix} P_l^m(\cos\bar{\xi}) & -Q_l^m(\cosh\bar{\eta}) \\ i\sqrt{\epsilon_\perp}\sqrt{\epsilon_z}\,\partial_{\bar{\xi}} P_l^m(\cos\bar{\xi}) & -\partial_{\bar{\eta}} Q_l^m(\cosh\bar{\eta}) \end{pmatrix}\,. \tag{4.45}$$

The system has the solution

$$t_l^m = \frac{1}{\det \mathcal{M}} \big[- \partial_{\bar{\eta}} Q_l^m(\cosh \bar{\eta}) P_l^m(\cosh \bar{\eta}) + Q_l^m(\cosh \bar{\eta}) \partial_{\bar{\eta}} P_l^m(\cosh \bar{\eta}) \big] , \tag{4.46}$$

$$r_l^m = \frac{1}{\det \mathcal{M}} \big[- i\sqrt{\varepsilon_\perp}\sqrt{\varepsilon_z} \partial_{\bar{\xi}} P_l^m(\cos \bar{\xi}) P_l^m(\cosh \bar{\eta}) + \\ + P_l^m(\cos \bar{\xi}) \partial_{\bar{\eta}} P_l^m(\cosh \bar{\eta}) \big] , \tag{4.47}$$

When Eq. (C.6) is satisfied, $\det \mathcal{M}$ vanishes, to that t_l^m and r_l^m diverge. This behavior is consistent with having a resonant response at the polariton eigenfrequencies.

The response electric field outside the spheroid is $\mathbf{E}_2^r = -\partial_{\mathbf{r}}[\Phi_2(\mathbf{r}) - \Phi_d(\mathbf{r})]$. The distributions of the electric field calculated at several periodic orbit frequencies of the bulk waves and the HSM are shown in Fig. 4.10. They display an enhanced amplitude at the locations of the classical trajectories launched from the point on the surface facing the dipole source. However, at frequencies away from those of the resonances, wave packets follow trajectories that spread all over the spheroid, giving rise to an irregular background. The damping loss of the media has been neglected throughout these calculations, making this effect more apparent. If the frequency is detuned by roughly $5\,\mathrm{cm}^{-1}$, i.e., a mere 0.3% to either side off the periodic orbit frequency, these classical trajectories disappear.

The reason why the shape of the high-intensity ray patterns matches the classical periodic orbits, dominating the field distribution, can be understood as follows. Consider that the incident field is a superposition of wave packets launched from a finite-size region facing the dipole. Wave packets whose launching points belong to a short periodic orbit create a strongly concentrated electric field. The rest, however, follow quasi periodic classical trajectories that spread all over the spheroid, giving an approximately uniform background.

Near-field imaging experiments are expected to be most sensitive to the electric field distribution on the surface of the granule. Panels S_1-S_3 of Fig. 4.10 show examples of such distributions projected on the $x - z$ plane. They demonstrate directional ray patterns at the frequencies of the surface periodic orbits S_1-S_3 of Fig. 4.7.

4.7 Conclusions

In this chapter, we have investigated several properties of confined polariton modes in spheroidal nanogranules of polar hyperbolic materials. Motivated by the experimental measurement of subwavelength resonances with high quality factors, our analysis provided a transparent physical picture based on ray optics.

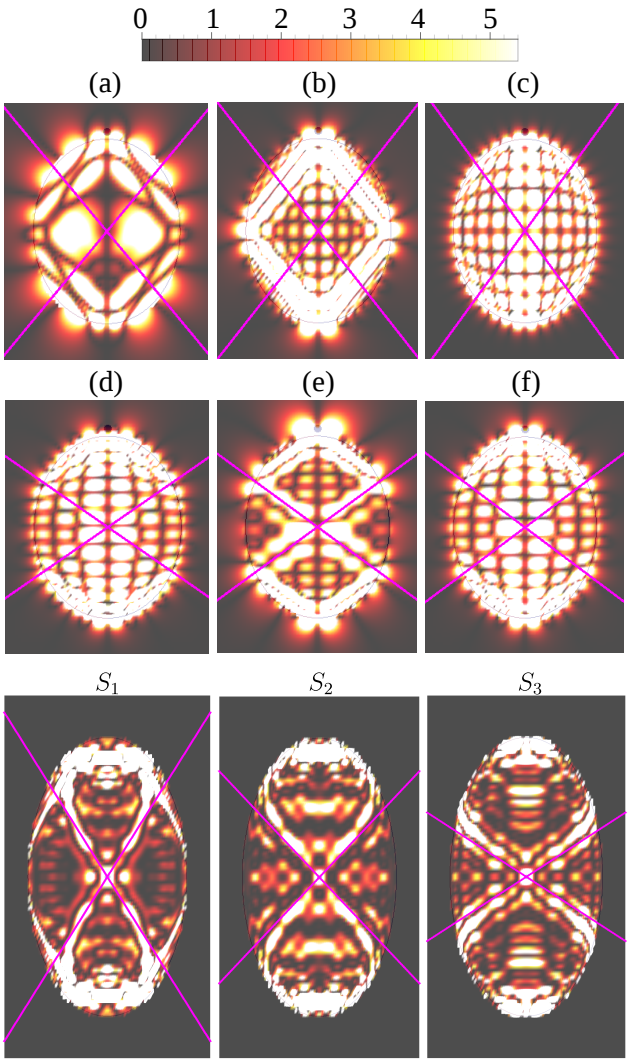

Figure 4.10: (a)-(f): color plots of $|E_x|$ in a meridional cross section of a hBN spheroid due to a dipole source located just above the north pole and pointing north. Outside the spheroid, the own field of the dipole is subtracted away for clarity. The frequencies in (a)-(c) are 1551, 1555 and 1561 cm^{-1}. In (d)-(f), they are 1490, 1494 and 1497 cm^{-1}. The middle numbers in these sets match the frequencies of B_1 and B_2 in Fig. 4.7 for the aspect ratio $a_\perp/a_z = \tanh 1 \simeq 0.761$. The tilted magenta lines run parallel to the polariton group velocity. S_1-S_3: color plot of E_z^2 at the surface of the spheroid projected onto the meridional plane. The dipole is now just above the surface at the center of each plot. The frequencies in S_1-S_3 are 1557, 1535 and 1488 cm^{-1}, same as in Fig. 4.7 for the aspect ratio $a_\perp/a_z = \tanh 0.5 \simeq 0.462$. The tilted magenta lines run parallel to the HSM group velocity at the center of the image.

A correspondence between particle and wave dynamics was established with the optical Hamiltonian for both bulk and surface modes. Subsequently, the problem was analyzed under two complementary approaches of wide use in semi-classical physics, namely the EBK and Gutzwiller's formalisms, which ultimately allowed to complete the interpretation of the measurements. With the former, we presented a method for computing eigenfrequencies in the asymptotic limit, and verified its accuracy by comparison with the exact analytical results. The latter, on the other hand, unraveled the convergence of the dispersion relation of closed orbits with the same topology, allowing to associate a shape or trajectory to each resonance. Not only does this support their interpretation as the result of a constructive ray interference, but also yields insightful information about some suggested near-field measurements. Numerical simulations and wave packet dynamics of polaritons were presented endorsing this point.

Concerning future prospects, the studied phenomena may also have far-reaching technological implications. One can imagine a whole class of polaritonic devices that would include nano resonators, hyperlenses or infrared photon sources. Such devices would be deeply sub-diffractional and low-loss because phonon polaritons are immune to electronic losses that plague conventional metal-based plasmonics. Our general approach may be useful for the design and optimization of these devices.

Chapter 5

Orbital magnetic susceptibility of graphene and MoS_2

5.1 Introduction

Till the development of the modern theory of orbital magnetization, the magnetic response was addressed from either the perspective of isolated atoms or the picture of electron gases with a certain effective mass.[179–181] In a nutshell, the former considered the Schrödinger equation with the minimal coupling, the interaction $\sim \mathbf{H} \cdot \mathbf{S}$ between the magnetic field and the spin, and Hund's rules. These together resulted in the competition between the Larmor and Van Vleck's contributions, or in Curie's law at zero temperature. As for metals and semiconductors, the magnetic response was believed to be utterly determined by the competition between Landau diamagnetism —as a sort of Lenz's law for the carriers— and Pauli paramagnetism —accounting for the coupling of their spins with $\mathbf{H}$—.

However, orbital magnetization in solids has gained renewed attention in view of new two-dimensional materials with topologically non-trivial band structures,[182] for which effects not captured by the aforementioned formalism become relevant. Semiclassical approaches including geometrical effects due to a non-trivial Berry curvature[43,48,183–186] or Green's function techniques[44,45,187,188] offer new perspectives and thus reinforce the motivation for deeper studies in this field.

Many advances, like the generalization of Fukuyama's formula to tight-binding systems,[45] are fairly recent. Among the new phenomena arising from this approach, one can highlight the prediction of paramagnetism resulting from the periodic lattice potential due to a sum rule. A paramagnetic orbital response also occurs necessarily around van Hove singularities[189] and in Dirac systems the sublattice isospin degree of freedom gives rise to a contribution that can be interpreted as the traditional Pauli para-

magnetism.[132] Moreover, contrarily to previous approaches via the Peierls-Landau formula[190] and its generalization to multi-band systems, interband (or better geometrical) processes turn out to play a crucial role, e.g., filled bands need not be magnetically inert.[43,191] In this context, it was shown that the band structure does not allow to uniquely determine the magnetic response of a solid, in stark contrast with the Peierls-Landau approach, i.e., different systems with an identical band structure can display completely opposite orbital magnetic responses.[47] The topological aspects of the band structure partly encoded in the Berry curvature play an important role in this scenario.[43,185] In fact, using the semiclassical wavepacket approach, a complete discussion about the several contributions to the magnetic susceptibility including purely geometrical terms was recently presented in Ref. [48].

Given the interest that all these results have inspired, this chapter focuses on two prominent 2D materials which display a non-trivial topological band structure, namely graphene and MoS_2. Graphene is characterized by a Berry phase of π manifested in the half-integer quantum Hall effect,[6,7] gapped graphene shows topological currents at zero magnetic field,[192] and MoS_2 is a topological valley insulator.[15,193] It is thus worthwhile to count on a detailed characterization of their magnetic response through the discussion of the magnetic susceptibility. Moreover, the availability of experimental techniques involving highly pure graphene flakes encourages our study as liable to be tested.[194]

In this chapter, we will perform the numerical calculation of the orbital magnetic susceptibility, χ_{orb}, for multi-band tight-binding models using the Green's function formalism. For graphene, we will deal with a nearest-neighbor 8-band model including all $2s$ and $2p$ orbitals. To model MoS_2, the relevant bands are formed by d-orbitals with a small influence of p orbitals amounting to an effective 12-band model.[193,195,196]

We will also discuss the nature of the processes involved in the magnetic response by analyzing the contribution of each point of the first Brillouin zone to χ_{orb}. The action of processes related to the Fermi surface or to geometrical effects can be distinguished by means of this approach, which yields valuable information to physically understand the magnetic response of solids. Finally, we address the magnetic response by means of several 2-band tight-binding as well as continuum models. The latter are mostly valid for energies close to the valence and conduction bands, but also suit other parts of the spectrum like the Dirac gap in between the second and third core bands of MoS_2. We analyze the sources underlying all these facts, the Berry curvature playing a crucial role, and discuss the seek for a 2-band model that yields an accurate continuum description of MoS_2 at the neutrality point. This will allow us to address a still debated question about the magnetic response: under which conditions χ_{orb} can be qualitatively extracted from the mere knowledge of the band structure.

This chapter is organized as follows. The formalism for calculating the orbital magnetic susceptibility of a general tight-binding model as well as previous approaches are recalled in Sec. 5.2 and in an appendix. In Sec. 5.3, we introduce the Hamiltonians used to describe gapless and gapped graphene, calculate and compare their respective magnetic susceptibilities, and relate these to the features of the band structure. Sec. 5.4 is analogous but devoted to MoS_2. Sec. 5.5 establishes a comparison with effective models for both materials, and finally our conclusions are presented in Sec. 5.6.

5.2 Magnetic susceptibility of tight-binding models

We numerically calculate the orbital magnetic susceptibility using the following formula, valid for arbitrary tight-binding models:[44,45]

$$\begin{aligned}\chi_{\mathrm{orb}} = &-\frac{\mu_0 e^2}{2\pi\hbar^2} \times \mathrm{Im} \int_{-\infty}^{\infty} dE\, n_F(E) \\ &\times \frac{1}{A} \sum_{\mathbf{k}} \mathrm{Tr} \Big\{ \hat{\gamma}^x \hat{G} \hat{\gamma}^y \hat{G} \hat{\gamma}^x \hat{G} \hat{\gamma}^y \hat{G} + \\ &+ \frac{1}{2} (\hat{G}\hat{\gamma}^x \hat{G}\hat{\gamma}^y + \hat{G}\hat{\gamma}^y \hat{G}\hat{\gamma}^x) \hat{G} \frac{\partial \hat{\gamma}^y}{\partial k_x} \Big\}, \end{aligned} \tag{5.1}$$

where $\hat{G} = (E - H_{\mathbf{k}} + i0^+)^{-1}$, $\hat{\gamma}^{x,y} = \partial H_{\mathbf{k}} / \partial k_{x,y}$ and $H_{\mathbf{k}}$ is the Hamiltonian at wave vector $\mathbf{k}$ including the spin degree of freedom. Further, μ_0 is the vacuum permeability, A denotes the sample area, and $n_F(E) = (e^{(E-\mu)/T} + 1)^{-1}$ is the Fermi function. In the following, we will present results at $T = 0$ with the Fermi energy $\mu = E_F$.

To derive the gauge-invariant magnetic susceptibility for a general tight-binding model, the correct wavevector dependence of the current operator needs to be used.[80] Only then the gauge-dependent contribution of the diamagnetic current is canceled, see the appendix. The longitudinal response can be obtained from the above formula by replacing the y superscripts with x and vice versa. It must necessarily be zero due to gauge invariance, which is guaranteed by the exact cancellation of the first term by the second term. Let us also highlight the sum rule[45]

$$\int_{-\infty}^{\infty} dE_F\, \chi_{\mathrm{orb}}(E_F) = 0\,, \tag{5.2}$$

which is obtained from the fact that $\chi_{\mathrm{orb}}(E_F)$ can be analytically continued into the upper complex plane, together with the residuum theorem. Details on the above discussion can be found in the appendix.

5.2.1 Previous approaches

We recall that the first term in brackets of Eq. (5.1) yields the Fukuyama formula,[187] which is valid for a Galilean invariant system with a possible linear term in $\mathbf{k}$, i.e., for all models with $\frac{\partial \hat{\gamma}^y}{\partial k_x} = 0$. But also for isotropic models like the tight-binding model for graphene involving only the p_z orbitals, this term is dominant and the second term can almost be neglected. However, in the case of the tight-binding models for graphene involving s orbitals, the second term becomes quantitatively important, i.e., $\frac{\partial \hat{\gamma}^y}{\partial k_x}$ is not small due to the directional σ-bonds.

An even earlier approach is given by the Peierls-Landau orbital susceptibility and its trivial extension to multi-band systems,[187,190]

$$\chi_{\mathrm{PL}} = \frac{\mu_0 e^2}{12\hbar^2} \frac{1}{A} \sum_{\mathbf{k},n} n_F'(\epsilon_{n,\mathbf{k}}) \left[\epsilon^{xx}_{n,\mathbf{k}} \epsilon^{yy}_{n,\mathbf{k}} - (\epsilon^{xy}_{n,\mathbf{k}})^2 \right] . \tag{5.3}$$

Here, $n_F'(\epsilon)$ is the derivative of the Fermi-Dirac distribution, $\epsilon^{x_i x_j}_{n,\mathbf{k}}$ denotes the derivative of the energy eigenvalues with respect to k_{x_i} and k_{x_j}, and n is the band index.

Remarkably, χ_{PL} only depends on the dispersion relation, whereas in Eq. (5.1), further information concerning the features of the eigenstates is contained. Furthermore, due to n_F', only states around the Fermi surface contribute to Eq. (5.3). This is again in contrast with Eq. (5.1), where matrix instead of scalar multiplications properly include all contributions originating from possible interband transitions. These differences turn out to be crucial in the appropriate description of the magnetic response of a multi-band tight-binding system, as we will show throughout this work.

5.2.2 Continuum models and lattice contribution

Several prominent features of the magnetic response of systems with a direct band gap at the K-points can be understood from the effective continuum model of gapped Dirac fermions:[132]

$$\chi_{\mathrm{Dirac}} = -\frac{g_s g_v \mu_0 e^2}{6\pi} \frac{1}{2m_{\mathrm{eff}}} \Theta(|\Delta| - |E_F|) , \tag{5.4}$$

where g_s and g_v are the spin and valley degeneracy, respectively, $2|\Delta|$ is the gap and m_{eff} is the mean effective mass derived from the curvature of the bands close to it. For a Dirac model with constant gap, we have $m_{\mathrm{eff}} = |\Delta|/v_F^2$, with v_F the Fermi velocity. For chemical potentials inside the gap, χ_{Dirac} is equal to the geometrical susceptibility as introduced in Ref. [48].

For a general gap with a k^2-dependence ($\Delta \to \Delta + \beta k^2$), this is modified to $m_{\mathrm{eff}}^{-1} = [(\hbar v_F)^2 + \beta\Delta]/(\hbar^2|\Delta|)$. In the limit of $\Delta\beta \to 0$, the step function

becomes a Dirac delta leading to the expression first obtained by McClure in the limit $T \to 0$:[197–199]

$$\chi_{\text{Dirac}} = -\frac{g_s g_v \mu_0 e^2 v_F^2}{6\pi} \delta(E_F - E_{DC}) \,. \tag{5.5}$$

We included the constant energy shift $E_{DC} = 0$ to indicate the location of the Dirac cone, needed for subsequent generalizations. In fact, the above formulas also hold for $H = \sum_{\mathbf{k}} \hbar(\mathbf{v}_1 \cdot \mathbf{k})\sigma_x + \hbar(\mathbf{v}_2 \cdot \mathbf{k})\sigma_y + \Delta\sigma_z$ by replacing $v_F^2 \to |\mathbf{v}_1 \times \mathbf{v}_2|_z$, so more general band-crossings ($\Delta = 0$) or gaps ($\Delta \neq 0$) display the same features of the response.

If we describe graphene by a single orbital tight-binding model with only nearest-neighbor hoppings, lattice effects can be separated from the contribution that come from the continuum model. We can then define the lattice susceptibility as[45]

$$\chi_{\text{lattice}} \equiv \chi_{\text{orb}} - \chi_{\text{Dirac}} \,, \tag{5.6}$$

valid for the gapless or gapped case. Using the following unit of the susceptibility

$$\chi_0 = \frac{\mu_0 e^2 |t| a^2}{\hbar^2},$$

we find that $\chi_{\text{lattice}}/\chi_0$ is now scale-invariant, i.e., independent of the parameters of the model, where t is the hopping amplitude and a the lattice constant. In the continuum limit $a \to 0$ keeping $\frac{3at}{2\hbar} = v_F = \text{const.}$, $\chi_0 \to 0$ and the lattice contribution thus also tends to zero.

In the case of multi-band Hamiltonians with several hopping parameters, such a simple, scale-invariant quantity cannot be defined, especially not in the case of MoS_2. Still, we will present all results in units of χ_0 and use $t = 2.8\,\text{eV}$ and $t = 1.6\,\text{eV}$ for graphene and MoS_2, respectively. Notice that then $\chi_0/a \sim \alpha\frac{v_F}{c}$ is the natural scale of the magnetic susceptibility with $\alpha \approx 1/137$ the fine-structure constant.

In the subsequent sections, we will use the above definitions and proceed to apply these expressions to different tight-binding systems modeling graphene and MoS_2. Special attention will be paid to interpret the physics encoded in Eq. (5.1), to the relation of the results with the underlying band structure and to the possibility of finding effective models that yield a correct description of the magnetic response of these materials.

5.3 Magnetic susceptibility of graphene

In this section, we discuss the magnetic response of graphene within the Slater-Koster description including all four orbitals of the valence band, i.e., $2s$, $2p_x$, $2p_y$, and $2p_z$. The parameters of the hopping elements and energies

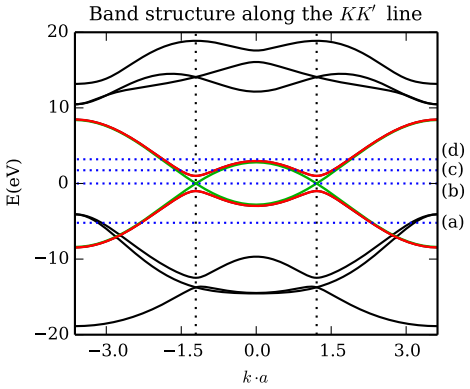

Figure 5.1: Band structure of the Slater-Koster model including the σ-bonds (black lines) and π-bonds (red and green referring to the gapless and gapped case, respectively). Vertical dotted lines indicate the position of K and K' points. Horizontal blue dotted lines labeled with a letter are respective to the Fermi energies of Fig. 5.3.

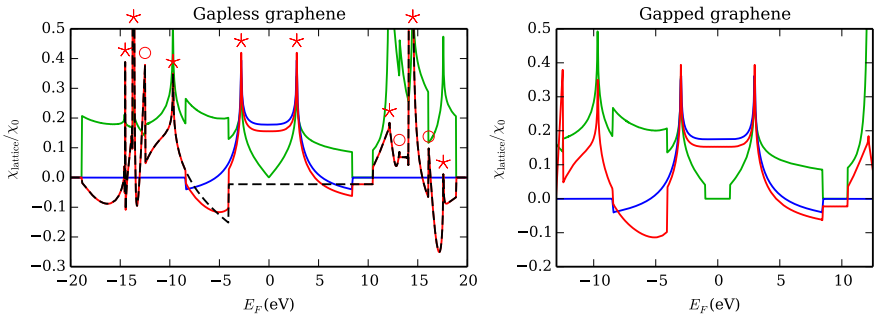

Figure 5.2: The lattice susceptibility χ_{lattice} for the 8- (red) and 2-band (blue) models of graphene described in the main text. For the gapped case, a closeup view is chosen for the sake of clarity. Actually, the parts of the curves outside of the plot range coincide with those of the left figure. The dashed black line depicts χ_{orb} of the σ-bands. The density of states is plotted in green. In the left figure, the asterisks over the peaks denote that they arise due to van Hove singularities, whereas circles are placed over finite discontinuities coming from band edges.

are adopted from Ref. [200]. In Fig. 5.1, the band structure is shown in the KK' direction for the gapped ($\Delta = 1\,\mathrm{eV}$) and gapless case.

The lattice contribution of the magnetic orbital susceptibility for gapless graphene appears on the left hand side of Fig. 5.2 as a red curve. Since the σ-bands (black dashed curve) and π-bands (blue curve) decouple due to symmetry, the π-bands yield a contribution to χ_{orb} identical to that discussed in Ref. [45]. Further, the total susceptibility and the one coming from the σ-bands coincide for low and high energies. For comparison, also the density of states is shown as a green curve.

For Fermi energies around half filling, the lattice contribution displays a constant plateau that evolves into the expected paramagnetic divergences when hitting the van Hove singularities.[189] Due to the presence of at least one van Hove singularity in each band, χ_{orb} shows a quite irregular structure. We identify the resulting paramagnetic divergences in Fig. 5.2, making a distinction with respect to finite discontinuities that come from band edges. Although the latter might be unraveled by peak asymmetry, our conclusions have been drawn from a careful analysis of the band structure. A diamagnetic response is found for Fermi energies in the intervals $(-19, -15)\,\mathrm{eV}$ and $(-8, -4)\,\mathrm{eV}$, as is suggested by the parabolic dispersion relation of the corresponding bands, i.e., Landau diamagnetism.

The full magnetic orbital response shows two delta-like diamagnetic peaks at Fermi energies $E_F \approx \pm 14\mathrm{eV}$ associated with the band-crossing at the K-points. We were able to subtract these contributions using Eq. (5.5) with $v_F \simeq 3.9 \cdot 10^5\,\mathrm{m/s}$ ($v_F \simeq 3.5 \cdot 10^5\,\mathrm{m/s}$) for the lower (upper) crossing at $E_{DC} \approx \pm 14\mathrm{eV}$, where the Fermi velocities and Dirac cone energies were extracted from the band-structure. In Fig. 5.2, we thus plot the generalized lattice contribution

$$\chi_{\mathrm{lattice}} \equiv \chi_{\mathrm{orb}} - \chi_{\mathrm{Dirac}} - \chi^{\sigma}_{\mathrm{Dirac}}\,, \tag{5.7}$$

where χ_{Dirac} just involves the valence and conduction bands, whereas $\chi^{\sigma}_{\mathrm{Dirac}}$ comprises the aforementioned delta-like Dirac contributions coming only from the σ bands.

Let us now comment on the constant diamagnetic contribution from the σ-bands inside the gap around the Γ-point which amounts to an extra $\sim 12\%$ lattice contribution to the π-electrons. For gated graphene away from half-filling and at low temperatures, we thus expect a measurable contribution of the σ-bands to the magnetic susceptibility. This response is of pure geometrical nature as we will argue below.

On the right hand side of Fig. 5.2, we show the total (red) and π-band (blue) lattice contribution χ_{lattice} of the gapped graphene model with $\Delta = 1\,\mathrm{eV}$ for energies around the neutrality point. Interestingly, both models, gapless and gapped graphene, show an almost identical lattice contribution even at the energies where their spectra strongly differ, namely close to the neutrality point, as can be appreciated form the density of states (green

curve) on the left and right side of Fig. 5.2. This is an indicative of the fact that the Dirac model is the continuum version of the lattice models under consideration.

5.3.1 Brillouin zone analysis

In order to count on a deeper understanding of the above results, we proceed to discuss the individual contribution of each point of the first Brillouin zone to $\chi_{\rm orb}$, i.e., we plot $\bar{\chi}_{\rm orb}(\mathbf{k}, E_F)$ for the first Brillouin zone with $\chi_{\rm orb}(E_F) = \sum_{\mathbf{k}} \bar{\chi}_{\rm orb}(\mathbf{k}, E_F)$. Our approach is intended to inquire about Eq. (5.1) in more detail and to unravel the physics behind it. Last but not least, it will serve as a tool to compare the magnetic response of the different models considered, see Sec. V.

In the following, we will focus on the case of gapped graphene for simplicity. The results for the first Brillouin zone are plotted in Fig. 5.3. It can be seen that the contributions to $\chi_{\rm orb}$ mostly come from points of the Brillouin zone that are pinned to the Fermi surface; the other states practically remain inert. Figs. 5.3 (a) and (c) depict this situation, dealing with more complex or simpler regions of the band structure, respectively. We also note that the response can be either diamagnetic (blue) or paramagnetic (red).

Let us now discuss the situation where the Fermi energy lies inside a gap. In fact, the highest diamagnetism is found for E_F inside the Dirac-like gap in clear contrast to the predictions of the Peierls-Landau formula. The $\mathbf{k}$-points contributing to the susceptibility are now concentrated in small regions around K and K' points as seen in Fig. 5.3 (b). Fig. 5.3 (d), on the other hand, addresses the origin of the constant diamagnetic plateau coming from σ-bands close to neutrality (cf. the dashed black line in Fig. 5.2). Interestingly, the magnetic response is now smeared throughout the whole Brillouin zone rather than being concentrated, e.g., around the Γ-point. This is probably due to a geometrical effect among those described in Ref. [48], most likely the quantum metric.

We conclude that in principle there exist clear mechanisms underlying the magnetic response of a tight-binding system and they are strongly related to the band structure. For Dirac gaps around the K-points, transitions only around these points are relevant, whereas for gaps around the Γ-point, transitions in the whole Brillouin zone contribute to the final response.

In the next section, we will extend our analysis to a more complex system, i.e., transition metal dichalcogenides in form of MoS_2.

5.4 Magnetic susceptibility of MoS_2

In this section, we discuss the orbital susceptibility for the 12-band Hamiltonian derived in Refs. [193,195,196]. A plot of the band structure along the $K - K'$ direction is shown in Fig. 5.4. Let us point out that there are two

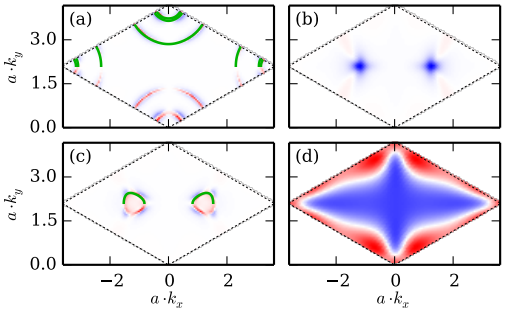

Figure 5.3: Contribution of each point of the Brillouin zone to $\chi_{\rm orb}$ for a fixed Fermi energy E_F, as defined in the main text. Paramagnetism and diamagnetism correspond to red and blue, respectively, the color scale being normalized to $\max|\bar{\chi}_{\rm orb}(\mathbf{k}, E_F)|$ for the given E_F. The green lines depict the Fermi surface. For the sake of clarity, they appear only in the upper half of each plot, but can be extended to the lower one by an horizontal mirror reflection. E_F takes the values -5.2 (a), 0 (b), 1.75 (c), and 3.2 eV (d), which are indicated in Fig. 5.1 and labeled there with the corresponding letter. In the last case, only the contribution of the σ-bands has been considered. An imaginary part of the energy equal to 0.3 eV has been used in these calculations.

Dirac-like gaps centered at K and K': one between the second and third bands and another one between the valence and conduction bands.

The full magnetic orbital susceptibility $\chi_{\rm orb}$ as calculated by means of Eq. (5.1) is plotted in Fig. 5.5 as a red curve. We compare the results with the magnetic orbital response of the Peierls-Landau formula, Eq. (5.3), seen as a black line, together with the density of states (green line). Let us also comment on the two diamagnetic regions at Fermi energies matching those of the aforementioned gaps, which are highlighted (blue) in Fig. 5.4. Their expected magnetic susceptibility according to the Dirac continuum model, Eq. (5.4), is shown in Fig. 5.5 as a blue line.

Apart from diamagnetic regions associated to Dirac gaps or parabolic bands, we have again identified the paramagnetic peaks corresponding to van Hove singularities. Some of them are also reproduced by the Peierls-Landau magnetic susceptibility. The latter fails to yield other relevant features, though, above all concerning the magnetic response of filled bands. Let us also comment on the diamagnetic peak at $E_F \approx 1.7$eV with height $-3.7\chi_0$. This peak can be associated to four gapped Dirac cones located at close vicinities of the ΓM direction, for which the Berry curvature yields large values. Interesting physics might be expected to emerge from them, especially regarding their spin split character and high directional asymme-

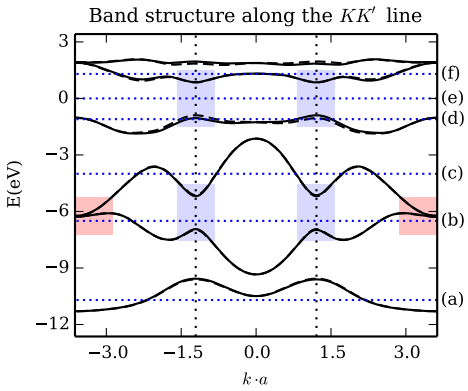

Figure 5.4: Section of the band structure of the MoS_2 12-band model of Ref. [193]. Solid (dashed) lines correspond to spin $s = (-)1$. The gaps and band overlap discussed in the main text have been highlighted in light blue and red, respectively. A close-up view of the valence and conduction bands appears in Fig. 5.7 (B). Vertical dotted lines indicate the position of K and K' points. Horizontal blue dotted lines labeled with a letter are respective to the Fermi energies of Fig. 5.6.

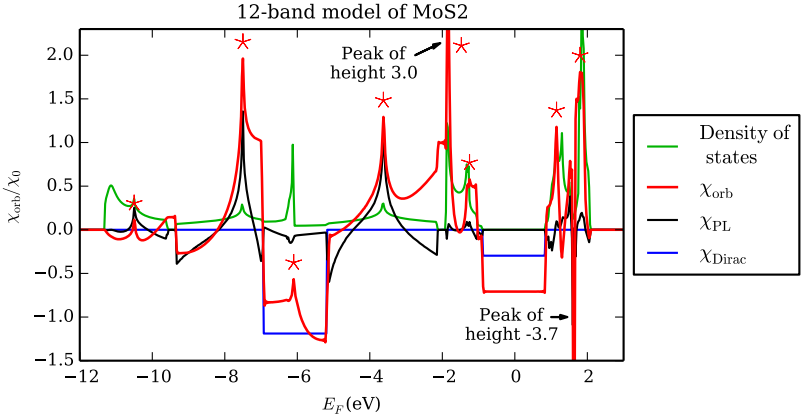

Figure 5.5: Magnetic orbital susceptibility of the MoS_2 12-band model using Eq. (5.1) (red) and Eq. (5.3) (black) and density of states (green). The text inside the plot corresponds to the red curve. Also shown the Dirac susceptibility of Eq. (5.4) for the gaps highlighted in Fig. 5.4 (blue). The asterisks mark the peaks associated to van Hove singularities.

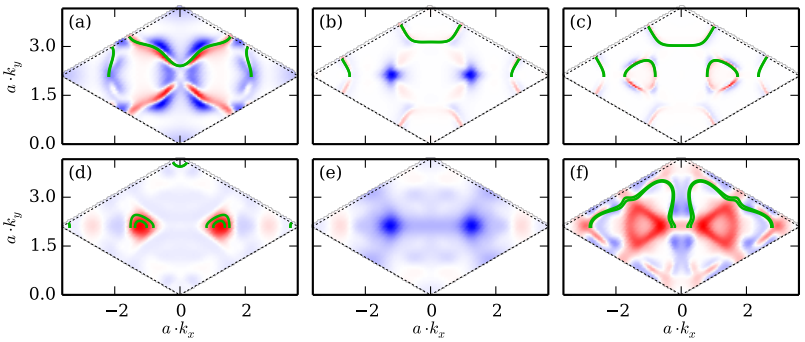

Figure 5.6: Same as Fig. 5.3 but for the 12-band model of MoS_2. E_F takes the values −10.7 (a), −6.5 (b), −4 (c), −1.1 (d), 0 (e) and 1.3 eV (f), which are indicated in Fig. 5.4 and labeled there with the corresponding letter. An imaginary part of the energy equal to 0.3 eV has been used in these calculations.

try. As for the experimental realization, reaching the corresponding Fermi energies could be overcome in the future by the use of liquid dielectric capacitors.

The red curve of Fig. 5.5 depicts one of the main results of this study, which can be experimentally verified, especially for neutral MoS_2 with the Fermi energy inside the gap. We will now continue with the Brillouin zone analysis for MoS_2.

5.4.1 Brillouin zone analysis

As in Sec. 5.3, we proceed to study the individual contribution of each point inside the 1st Brilluoin zone to χ_{orb}. Fig. 5.6 displays the results for this analysis, on the one hand confirming the conclusions we extracted from graphene and on the other hand offering more information to be discussed.

In the case of MoS_2, the subplots are now more diverse and complex than in the case of graphene. Still, we can associate most features to processes involving the Fermi surface, such as subplots (a), (c), and (d). In the case of subplot (b), we see contributions from the Fermi surface located around the Γ-point as well as processes involving the two K-points. This has been discussed above and the diamagnetic contribution due to the Dirac-like gap is shown as blue line in Fig. 5.5. Also for Fermi energies inside the valence and conduction band, the main contribution comes from the two K-points as can be seen in subplot (e). However, the structure is considerably more involved, indicating that the simple Dirac model does not quantitatively reproduce the diamagnetic response.

Let us finally discuss the spectrum shown in subplot (f), displaying fea-

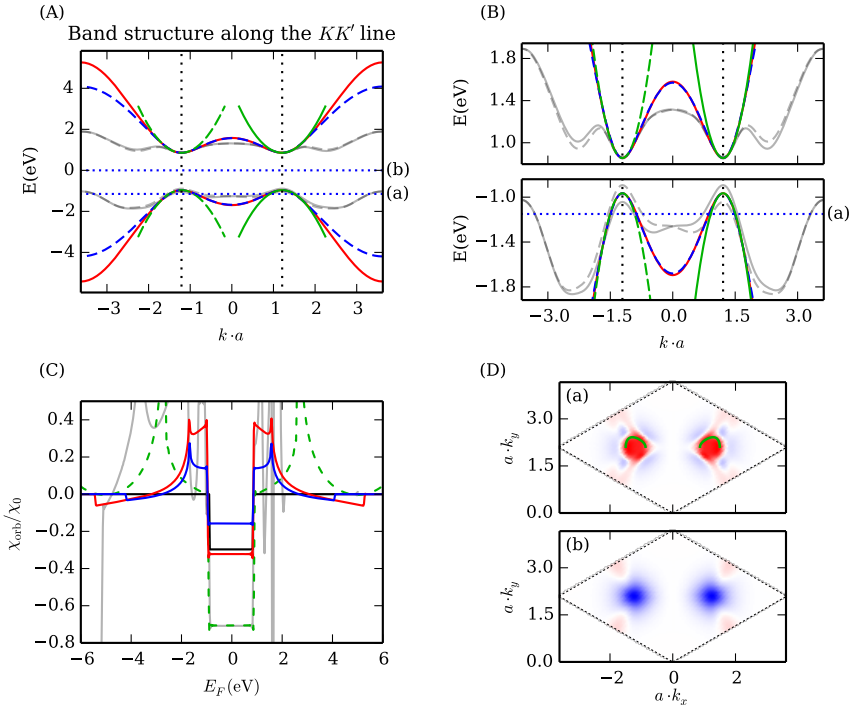

Figure 5.7: Band structure (A) and close-up view (B) for the 2-band lattice models of Eq. (5.8) with Eq. (5.9) (green); of Eq. (5.10) with Eq. (5.9) (red); and of Eq. (5.10) with Eq. (5.11) (dashed blue). Gray corresponds to the valence and conduction bands of MoS_2. Due to the differences in the unit cells, only the parabolic approximation —close to $k = 0$— of the square lattice bands is plotted near K (solid) and K' (dashed lines) points. Vertical dotted lines indicate the position of K and K' points, and horizontal blue dotted lines labeled with a letter are respective to the Fermi energies of (D). (C) depicts the magnetic susceptibilities with the same color code as (A) and (B). The extra black line depicts $\chi_{\text{Dirac}}/\chi_0$. (D) shows two subplots analogous to those of Fig. 5.3 but for the model of Eqs. (5.9) and (5.10). The corresponding Fermi energies are $-1.15\,\text{eV}$ (a) and 0 (b).

tures that were not seen in the case of graphene. Again, there is a contribution associated to the Fermi surface. But we also see a paramagnetic response displaying a prominent trigonal shape reminiscent of the Fermi surface of graphene at the M-point.

5.5 Effective models

We will now analyze reduced, effective models and test them with respect to their predictive reliability. We will first summarize the results for the continuum Dirac model and then look at two-band lattice models. Fig. 5.7 gathers all the results.

5.5.1 Effective continuum model

Let us summarize to what extent the continuum model of Eq. (5.4) agrees with the results yielded by Eq. (5.1). For graphene, we already concluded that the continuum model yields the main contribution to the magnetic response around the neutrality point. This is best seen from the lattice contribution χ_{lattice} close to half filling, which shows a constant paramagnetic offset independent of the actual gap coming from the orbital response of electrons outside the Dirac cone region. Also for energies at the two Dirac cones of the σ-band, the main contribution is given by Eq. (5.5).

For MoS_2, the discussion is more subtle and different for the two gaps present in the band structure. For the core gap, the diamagnetic depth is fairly reproduced by the Dirac well. The finer structure of the curve that corresponds to the full spectrum can be explained as a consequence of the band overlap at the corners of the 1st Brillouin zone, cf. Fig. 5.4, and the presence of a van Hove singularity within that energy range. On the other hand, when considering the gap between the valence and conduction band, there is only a qualitative agreement with the result of the Dirac continuous model, i.e., the well-like response is correctly reproduced, but the numerical value is off by approximately a factor of two. In fact, the trigonal warping in Fig. 5.6(e) indicates that the magnetic response is not well reproduced by assuming a simple Dirac-like gap (with and without a k^2-dependent mass). Also the product between the Berry curvature and the magnetic orbital moment as suggested by Ref. [48] do not yield contributions isotropically concentrated around the K-points. An effective continuum model to correctly describe the trigonal feature of the magnetic response and Berry curvature is thus still uncovered.

5.5.2 Effective two-band lattice models

For the magnetic orbital susceptibility of MoS_2 around the neutrality point, we carry out a comparison with three different two-band lattice models to

inquire about possible fits. They consist of a two-orbital square lattice and of a one-orbital hexagonal lattice with and without next-nearest neighbor coupling. We impose the constraint that they reproduce the energies of the 2-band effective Hamiltonian of Ref. [193], although neglecting the spin-valley splitting, see the close-up of the band structure in Fig. 5.7 (B). The hallmark of this effective description is the k^2-dependence of the potential and mass terms.

Firstly, let us introduce the tight-binding Hamiltonian defined on a square lattice with two orbitals at each site. The off-diagonal terms have their origin in a spin-orbit coupling. We thus have

$$H_{\mathbf{k}} = \begin{pmatrix} \frac{\Delta_0+\Delta}{2} + 2b\beta c_{\mathbf{k}} & -t_0 s_{\mathbf{k}} \\ -t_0 s_{\mathbf{k}}^* & \frac{\Delta_0-\Delta}{2} - 2b\beta c_{\mathbf{k}} \end{pmatrix}, \tag{5.8}$$

with $c_{\mathbf{k}} = 2 + \cos(ak_x) + \cos(ak_y)$ and $s_{\mathbf{k}} = \sin(ak_x) - i\sin(ak_y)$. We use the following parameters in order to match the band structure of the MoS_2 12-band model.

$$\begin{aligned} &\Delta_0 = -0.11\,\mathrm{eV}\,,\ \Delta = 1.82\,\mathrm{eV}\,,\ t_0 = 2.33\,\mathrm{eV}, \\ &\alpha = -0.01\,,\ \beta = -1.54 \end{aligned} \tag{5.9}$$

and $b = \hbar^2/(4m_0a^2) \simeq 0.572$ eV. Note that the contribution of α is neglected in the above Hamiltonian, but will be included below.

Secondly, the continuum model with quadratic mass and scalar potential can be deduced from a hexagonal lattice with a single orbital per site and next-nearest neighbor hoppings. Choosing the hopping parameters and on-site energies accordingly, we arrive at

$$H_{\mathbf{k}} = \begin{pmatrix} \frac{\Delta_0+\Delta}{2} + \frac{4b(\alpha+\beta)}{9}|\phi_{\mathbf{k}}|^2 & -\frac{2}{3}t_0\phi_{\mathbf{k}} \\ -\frac{2}{3}t_0\phi_{\mathbf{k}}^* & \frac{\Delta_0-\Delta}{2} + \frac{4b(\alpha-\beta)}{9}|\phi_{\mathbf{k}}|^2 \end{pmatrix}, \tag{5.10}$$

with the form factor $\phi_{\mathbf{k}} = \sum_j e^{i\delta_j\cdot\mathbf{k}}$ and δ_j $(j = 1, 2, 3)$ the three vectors joining nearest neighbors.

At last, the gapped Dirac lattice model with constant mass can be easily reproduced with a different choice of the parameters in Eq. (5.10):

$$\begin{aligned} &\Delta_0 = -0.11\,\mathrm{eV}\,,\ \Delta = 1.82\,\mathrm{eV}\,,\ t_0 = 2.02\,\mathrm{eV}\,, \\ &\alpha = \beta = 0\,. \end{aligned} \tag{5.11}$$

All models display the same curvature (mass) around the K-points, as can be seen from the band structures which are plotted over part of the MoS_2 spectrum in Figs. 5.7 (A) and (B).

5.5.3 Discussion

Here, we will compare the magnetic response of the effective two-band models with that of Sec. 5.4. To do so, we will include the necessary spin and valley degeneracy factors g_s and g_v, respectively, i.e., for the square lattice we include a factor $g_s g_v$ whereas for the hexagonal model only a factor g_s.

From Fig. 5.7 (C), one can appreciate a significant qualitative agreement but quantitative discrepancies between the different models even for Fermi energies inside the gap. This fact points at the discussion of Refs. [43,47], namely that a mere match of the band structure of two different solids does not guarantee a similarity in their respective χ_{orb}. Interestingly, however, the diamagnetic well depth of MoS_2 is precisely predicted by the square lattice model.

The discrepancies might lead to the conclusion that the orbital character of the lower and upper band needs to be reflected by the underlying effective tight-binding model in order to describe the magnetic response. Actually, the core gap of MoS_2 is mainly composed of p_x and p_y-orbitals (for lower and upper band), and in this case, a relatively precise χ_{orb} in terms of a continuum model could be found (cf. Sec. 5.5.1). On the contrary, the gap at the neutrality point is made up by $d_{x^2-y^2}$ and d_{xy}-orbitals (valence band) as well as predominately d_{z^2}-orbitals (conduction band),[193,195,196] for which our 2-band models fail to provide an accurate χ_{orb} value.

Under this perspective, we rather attribute the match of χ_{orb} between the 12-band and the square lattice models to a coincidence, so no further conclusions could be drawn.

A better understanding of the quantitative discrepancies and qualitative similarities emerges from a Brillouin zone analysis, that we proceed to carry out. The contributions to the magnetic response at each $\mathbf{k}$-point are shown in Fig. 5.7 (D). We choose the Hamiltonian of Eq. (5.10) with parameters of Eq. (5.9), although the other models, in particular the square lattice model, show similar behavior. The relevant Fermi energies are those either inside or very close to the gap, respective to subplots (a) and (b) of Fig. 5.7 (D). The corresponding patterns are quite similar to those of Fig. 5.6 (d) and (e). We thus conclude that the nature of the processes encoding the magnetic response is approximately the same for the two cases. This reinforces our previous comment about the qualitative agreement between their respective magnetic response. Concerning the quantitative discrepancies of a model with its effective counterpart, the threefold symmetry of Fig. 5.6 (e) cannot be reproduced by the 2-band models, implying a more complex geometrical contribution to the susceptibility than the product of the Berry curvature and the orbital magnetic moment.[48]

As a consequence of the previous discussion, it seems reasonable to state that the magnetic behavior of a material still remains at reach simply from the knowledge of the band structure, at least at a qualitative level. As for

the striking difference between the models discussed in Refs. [43,47], which might contradict this statement, we associate it to the presence of a flat band as also argued in Ref. [48]. Still, an accurate quantitative prediction depends on factors like the k-dependence of the mass term and the topological regime around the valleys and beyond.

5.6 Conclusion

In this chapter, we have studied the orbital magnetic susceptibility of graphene and MoS_2 described by effective multi-band tight-binding models. Like this, contributions from processes around the Fermi surface as well as geometrical aspects involving e.g. the Berry curvature are automatically incorporated. We obtained new results for the magnetic response for both materials which can be tested experimentally especially for Fermi energies close to the neutrality point or inside the gap.

More concretely, we calculated χ_{orb} for gapless and gapped graphene, dealing with an 8-band Slater-Koster model including also the σ-orbitals. This yields an additional $\sim 12\%$ diamagnetic contribution relative to the lattice susceptibility close to half filling, independent of whether the π-band is gapped or gapless. This additional contribution to χ_{orb} is constant inside the gap around the Γ-point and of purely geometrical nature. Still, it is fundamentally different from the geometrical susceptibility associated with the Dirac gap of the π-bands.

We were further able to identify prominent diamagnetic peaks of χ_{orb} with Dirac-cone like band-crossings which are exactly described by the McClure formula. We expect this delta-like diamagnetic response associated to Dirac cones to be a general geometrical effect due to the infinite Berry curvature, but also the related zero effective mass would give this result.

In the case of MoS_2 described by the 12-band model, we have identified two prominent diamagnetic contributions associated to two Dirac-like gaps. We have shown that the Dirac continuum model is quantitatively sensible only for the one between the core bands. As for energies close to the neutrality point, our analysis involved the comparison with three different 2-band lattice models, which match the band structure of MoS_2 in the vicinity of the gap but generally yield quantitatively different magnetic susceptibilities. Interestingly, only the one including two orbitals per site gave an accurate magnitude of the diamagnetism. The qualitative features of χ_{orb} are well reproduced in all cases, although since the topology is not the same and the values of the Berry curvature cannot be recovered, there are important quantitative differences.

Additionally, we have demonstrated that by analyzing the contribution to the total magnetic response in $\mathbf{k}$-space, valuable information can be gained to identify the processes. More concretely, we were able to associate the

response either to intraband transitions around the Fermi surface or to geometrical processes around the high-symmetry points K and M. Only the diamagnetic response of the σ-electrons inside the gap around the Γ-point could not be attributed to localized interband transitions. The finding of effective models describing this situation remains to be thoroughly clarified and shall be dealt with in future works.

Chapter 6

Conclusion

Throughout this thesis, we have focused on several novel materials, namely graphene, MoS_2 and hBN, all of which display exotic properties stemming from the particularities of their lattice structures. Light-matter interactions and the passage to semiclassical physics are the two main issues that encompass our different studies. As for the former, we have aimed at plasmons and polaritons, whereas for the latter we have addressed non-conventional ray optics and the modern theory of orbital magnetization. These research directions are far from being exhausted, and our contribution with new results actually motivates further investigations.

Regarding graphene, we performed a complete analysis about the linear current-current response function at finite temperature and chemical potential. This allowed a thorough characterization of plasmons, particularly concerning the so-far less studied transverse channel. We have reported their faster damping with temperature as compared with the longitudinal case, which entails the impossibility of inducing transverse plasmons at zero doping. The influence of the surroundings has also been addressed: to enhance the confinement of these modes, it is necessary to go far beyond the local limit through high-refractive-index embeddings, or to count on heterostructures built with perfect diamagnets. The minimum decay length is of the order of $10^{-5}\,\mathrm{m}$, much larger than that of density plasmons, which lies in the nm scale. Moreover, we discussed the absorption of electromagnetic radiation by single- and double-layer systems, finding a strong dependence on the incident angle and the polarization of light.

Subsequently, we studied mass-profile quantum dots as a new mechanism to confine carriers in graphene. We analyzed their spectrum as a function of the radius, comparing it to the previously featured potential-well dots. The influence of magnetic fields was also considered, yielding a remarkable valley splitting and different regimes according to the intensity of B: besides the typical Fock-Darwin spectrum, high values result in an equally spaced level structure arising due to the existence of the zeroth Landau level. Moreover, linear chains of mass-profile quantum dots have been discussed.

Bands of tunable gap and curvature are obtained, where overlap-assisted processes play a major role. By tuning the array parameters, interesting phenomena can be brought about. For example, for closely packed arrays, the renormalized mass can change sign; or, on the contrary, for a separation of approximately seven times the dot radius, Frenkel excitons can be encountered interacting through a dominating Förster transfer. Bose-Einstein condensates may spring up in this context, which is left to be explored in future works. The experimental feasibility of these setups is currently at reach, adding extra interest to our theoretical predictions.

Polaritons are another collective excitation arising from light-matter interactions. Part of this thesis focuses on polar hyperbolic materials, where they show extraordinary properties. Specifically, our study dealt with hBN, aiming at the explanation of the mid-infrared resonances measured on a lattice of nanocones. From the perspective of Hamiltonian optics and two different approaches, namely the EBK and Gutzwiller's formalism, the experiments were successfully reproduced and interpreted in terms of a simple physical picture. Remarkably, the convergence of the dispersion relations associated to orbits that display a common topology shines light on the origin of the resonances, evoking a constructive interference of rays. Moreover, this procedure provides a method to predict intensity patterns in near-field measurements from the knowledge of classical trajectories. A numerical simulation was performed to illustrate this point.

At last, the orbital magnetic susceptibility of graphene and MoS_2 was analyzed using multi-band tight-binding models. For the case of graphene, a $\sim 12\%$ diamagnetic contribution was obtained close to half-filling as a lattice effect of the σ orbitals, which is of purely geometrical nature. Other features, like some prominent diamagnetic peaks, were interpreted in terms of the spectrum structure. On the other hand, a 12-band model used to describe MoS_2 yields two remarkable diamagnetic wells associated to two Dirac-like gaps. The Dirac continuum model produces accurate results only for one of them, whereas for the other, close to neutrality, there are some quantitative differences. The same happens with other 2-band lattice models that fit the band structure near half filling, devised to discuss the physical origin of the magnetic response. Our analysis involved the breakdown of the magnetic susceptibility into the contribution of each point in $\mathbf{k}$ space, which provides relevant information concerning this issue.

Conclusión

A lo largo de esta tesis, se han estudiado varios materiales novedosos, a saber, grafeno, MoS_2 y hBN, los cuales presentan propiedades exóticas a raíz de las particularidades de su estructura de red. Las interacciones radiación-materia y el marco de la Física semiclásica son los dos temas principales que engloban los diferentes estudios expuestos. En cuanto al primero, nos hemos centrado en los plasmones y polaritones, mientras que el último se ha enfocado a la Óptica de rayos no convencional y a la teoría moderna de magnetización orbital. Estas líneas de investigación todavía están lejos de agotarse, y nuestra contribución con nuevos resultados de hecho motiva nuevos estudios.

Sobre grafeno, se ha llevado a cabo un análisis exhaustivo de la respuesta lineal corriente-corriente a temperatura y potencial químico finitos. Esto permite una caracterización completa de los plasmones, particularmente los propios del menos estudiado canal transversal. Hemos descrito su decaimiento con la temperatura, más rápido que el de sus análogos longitudinales, lo que conlleva la imposibilidad de inducir plasmones transversales a dopado cero. La influencia del entorno también se ha analizado: para incrementar el confinamiento de estos modos, es necesario ir más allá del límite local a través de la presencia de dieléctricos con alto índice de refracción, o contar con heteroestructuras que constan de materiales perfectamente diamagnéticos. El mínimo decaimiento obtenido es del orden de 10^{-5} m, mucho mayor que el de los plasmones de densidad, que se encuentra en la escala nanométrica. Además, se ha discutido la absorción de radiación electromagnética en sistemas de una y dos capas, observándose una fuerte dependencia con el ángulo incidente y la polarización de la luz.

Seguidamente, se han estudiado los puntos cuánticos de perfil de masas como un nuevo mecanismo para confinar portadores en grafeno. Se ha analizado su espectro en función del radio, comparándolo con los previamente descritos puntos cuánticos de pozo de potencial. La influencia de campos magnéticos también se ha tenido en cuenta, dando lugar a un destacable desdoblamiento de valle y regímenes diferentes según su intensidad: además del típico espectro de Fock-Darwin, valores elevados dan lugar a una estructura de niveles equiespaciados que surgen debido a la existencia del nivel cero de Landau. Además, se han estudiado cadenas lineales de puntos cuánticos

de perfil de masas. Se han obtenido bandas de *gap* y curvatura variables, donde procesos asistidos por el solape de las funciones de onda juegan un papel fundamental. Controlando los parámetros de la cadena, puede darse lugar a fenómenos de interés. Por ejemplo, para distribuciones compactas, la masa renormalizada puede cambiar de signo; o, por el contrario, para una separación de aproximadamente siete veces el radio, pueden encontrarse excitones de Frenkel que interaccionan a través de la dominante transferencia de Förster. En este contexto, podrían darse condensados de Bose-Einstein, cuyo estudio se pospone como objeto de futuras investigaciones. Este tipo de sistemas está actualmente al alcance experimental, lo que añade un interés extra a nuestras predicciones teóricas.

Los polaritones son otra excitación colectiva producto de las interacciones radiación-materia. Parte de esta tesis se centra en materiales polares hiperbólicos, donde presentan exóticas propiedades. Específicamente, nuestro estudio trata con hBN, atendiendo a la explicación de las resonancias medidas en el infrarrojo medio en una red de nanoconos. Desde la perspectiva de la Óptica Hamiltoniana y dos procedimientos diferentes, que son el método EBK y el formalismo de Gutzwiller, los experimentos se han reproducido con éxito y han sido interpretados en términos de una imagen física sencilla. Es destacable cómo la convergencia de las relaciones de dispersión asociadas a órbitas que tienen una topología común desvela el origen de las resonancias, evocando un fenómeno de interferencia constructiva. Además, este procedimiento proporciona un método para predecir los patrones de intensidad en medidas de campo cercano a partir del conocimiento de las trayectorias clásicas. Una simulación numérica se ha llevado a cabo para ilustrar este punto.

Por último, la susceptibilidad magnética orbital de grafeno y MoS_2 ha sido analizada a través de modelos de *tight-binding* multibanda. En el caso de grafeno, aparece una contribución diamagnética del 12 % cerca del punto de neutralidad a raíz de la contribución de red de los orbitales σ, que es de carácter puramente geométrico. Otras características, como algunos prominentes picos diamagnéticos, han sido interpretadas en términos de la estructura del espectro. Por otra parte, el modelo de 12 bandas de MoS_2 da lugar a dos notables pozos diamagnéticos asociados a dos *gaps* de Dirac. El modelo de Dirac en el continuo produce resultados precisos sólo para uno de ellos, mientras que para el otro, cerca de la neutralidad, hay algunas diferencias cuantitativas. Lo mismo ocurre con otros modelos de red de dos bandas que se ajustan al espectro a bajas energías, específicamente concebidos para discutir el origen de la respuesta magnética. Nuestro análisis desglosa la susceptibilidad magnética en la contribución de cada punto del espacio $\mathbf{k}$, lo que proporciona información relevante sobre este aspecto.

Appendix A

Linear-response theory

Linear-response theory, first presented in a seminal paper by Kubo,[201] describes the effect of a time-dependent perturbation acting on a system.

In the realm of Condensed Matter Physics, it yields insightful information regarding the spectrum of a solid, its transport and optical properties among others, the role of interactions and the possible existence of collective oscillations. Focusing on the first-order term of a perturbative expansion, it describes the probe of the system through external sources, which is closely connected to the information that experiments usually provide.

This formalism, which has become a tool of foremost importance, is briefly outlined in this appendix. We present the notation and the essential results that will be used throughout Ch. 2. More details and comprehensive discussions can be found in Refs. [85,202–204].

A.1 Formulation of the linear-response theory

Given an unperturbed Hamiltonian H_0, a time-dependent external field $F^{\text{ext}}(t)$ and an observable $\hat{B}$, a total Hamiltonian

$$H = H_0 + F^{\text{ext}}(t)\hat{B} \tag{A.1}$$

is considered. Due to the term $F^{\text{ext}}(t)\hat{B}$, the unperturbed mean value of the observable $\hat{A}$, $\langle\hat{A}\rangle_0$, is altered to yield $\langle\hat{A}\rangle_F(t)$, which fulfills

$$\langle\hat{A}\rangle_1(t) \equiv \langle\hat{A}\rangle_F(t) - \langle\hat{A}\rangle_0 = \int_0^{t-t_0} d\tau\, \chi_{AB}(\tau) F^{\text{ext}}(t-\tau) \tag{A.2}$$

at first perturbation order. Here, t_0 represents the time at which the perturbation is switched on. The retarded linear-response function has been defined as

$$\chi_{AB}(\tau) \equiv -\frac{i}{\hbar}\Theta(\tau)\langle[\hat{A}(\tau), \hat{B}(0)]\rangle_0\,, \tag{A.3}$$

where operators are expressed in the Heisenberg picture. Physically, the Θ function encodes causality and entails the analiticity of $\chi_{AB}(\omega)$ in the upper complex plane.

It is convenient to switch to the frequency domain in order to simplify convolutions in time. Eq. (A.2) turns then into

$$\langle \hat{A} \rangle_1(\omega) = \chi_{AB}(\omega) F^{\text{ext}}(\omega) \,, \tag{A.4}$$

which will be ubiquitously used henceforth. Analogous considerations concerning spatial coordinates will be discussed in Appx. A.2.

At last, Eq. (A.3) is to be recast differently in regard to computational purposes. It can be rewritten in terms of the unperturbed eigenstates $|m\rangle$ with energy ϵ_m and occupation probability P_m, with the definitions $\omega_{nm} \equiv \epsilon_n - \epsilon_m$ and $O_{mn} \equiv \langle m|\hat{O}|n\rangle$ for $\hat{O} = \hat{A}, \hat{B}$. This results in the so-called Lehmann representation,

$$\chi_{AB}(\omega) = \frac{1}{\hbar} \lim_{\eta \to 0^+} \sum_{mn} \frac{P_m - P_n}{\omega - \omega_{nm} + i\eta} A_{mn} B_{nm} \,. \tag{A.5}$$

It is also helpful to prove relations like $\chi_{AB}(-\omega) = [\chi_{B^\dagger A^\dagger}(\omega)]^*$, which generally allows to simplify the description of response functions in terms of only positive frequencies. Moreover, the important inequality $\text{Im}[\chi_{BB^\dagger}](\omega) \leq 0$ for $\omega > 0$ follows from it together with the use of the Sokhotski-Plemelj theorem.

A.2 Position-dependent observables, homogeneous and isotropic systems

The above results can be easily extended to a more general Hamiltonian

$$H = H_0 + \int d^d r' \, F^{\text{ext}}(\mathbf{r}') \hat{B}(\mathbf{r}') \tag{A.6}$$

and observables $\hat{A}(\mathbf{r})$ and $\hat{B}(\mathbf{r})$ depending on the d-dimensional position vector $\mathbf{r}$. The analogous to Eq. (A.4) takes the form

$$\langle \hat{A} \rangle_1(\mathbf{r}, \omega) = \int d^d r' \, \chi_{AB}(\mathbf{r}, \mathbf{r}', \omega) F^{\text{ext}}(\mathbf{r}', \omega) \,, \tag{A.7}$$

having defined

$$\chi_{AB}(\mathbf{r}, \mathbf{r}', \omega) \equiv \chi_{A(\mathbf{r})B(\mathbf{r}')}(\omega) \,. \tag{A.8}$$

Since for homogeneous systems $\chi_{AB}(\mathbf{r}, \mathbf{r}', \omega) = \chi_{AB}(\mathbf{r} - \mathbf{r}', \omega)$, we will handle response functions of the form $\chi_{AB}(\mathbf{r}, \omega)$. In this case, Fourier transforming the $\mathbf{r}$ variable to $\mathbf{q}$ turns Eq. (A.7) into

$$\langle \hat{A} \rangle_1(\mathbf{q}, \omega) = \chi_{AB}(\mathbf{q}, \omega) F^{\text{ext}}(\mathbf{q}, \omega) \,, \tag{A.9}$$

with

$$\chi_{AB}(\mathbf{q},\omega) = \chi_{A(\mathbf{q})B(-\mathbf{q})}(\omega)\,. \tag{A.10}$$

In turn, $O(\mathbf{q})$ is the Fourier transform of the operator $\hat{O}(\mathbf{r})$ for $\hat{O} = \hat{A}, \hat{B}$. The Lehmann representation becomes then

$$\chi_{AB}(\mathbf{q},\omega) = \frac{1}{\hbar}\lim_{\eta\to 0^+}\sum_{mn}\frac{P_m - P_n}{\omega - \omega_{nm} + i\eta}A_{mn}(\mathbf{q})B_{nm}(-\mathbf{q})\,. \tag{A.11}$$

Importantly, the full knowledge of the response function is given by $\chi_{AB}(q,\omega)$ in the case of isotropic systems.

A.3 Origin of dissipation

Without loss of generality due to linearity, consider a perturbation with a given frequency ω,

$$H = H_0 + F^{\text{ext}}(\omega)e^{-i(\omega+i\eta)t}\hat{A}^\dagger + [F^{\text{ext}}(\omega)]^* e^{i(\omega-i\eta)t}\hat{A}\,. \tag{A.12}$$

The last term is required to guarantee the hermiticity of the Hamiltonian, and the infinitesimal η, whose limit to 0 is taken in the final results, has been added so that the perturbation is adiabatically plugged in.

The average power delivered by the external field to the system during one period of oscillation T can be calculated as

$$W = \frac{1}{T}\int_0^T dt\,\frac{\partial}{\partial t}\langle\psi(t)|H(t)|\psi(t)\rangle = -2\omega\text{Im}\chi_{AA^\dagger}(\omega)|F^{\text{ext}}(\omega)|^2\,, \tag{A.13}$$

where the last equality follows after straightforward manipulations. It shows that the knowledge of $\text{Im}\chi_{AA^\dagger}$ fully determines the absorption energy rate fed to the system by the external driving force. As discussed in Appx. A.5, this fact allows to inquire about whether the system might present collective oscillations, and if so, to feature them in terms of their dispersion relation and damping.

A.4 Density-density and current-current responses

The density-density response was first approached departing from the following Hamiltonian, which only includes electric fields:

$$H = H_0 + \int d^d r\,\rho(\mathbf{r})\phi^{\text{ext}}(\mathbf{r})\,. \tag{A.14}$$

Here, $\phi^{\text{ext}}(\mathbf{r})$ denotes the applied electric potential, $\rho(\mathbf{r})$ the electronic density operator and d the dimensions of the system. The density-density correlation function $\chi_{\rho\rho}$ is then obtained by setting $\hat{A} = \hat{B} = \rho$ in Eq. (A.11).

The current-current response, however, cannot be analyzed with such a simple Hamiltonian as that of Eq. (A.14), since the magnetic fields associated to currents are neglected there. A more general one that includes them can be written in the Weyl gauge as

$$H = H_0 + \int d^d r\, \mathbf{j}(\mathbf{r}) \cdot \mathbf{A}^{\text{ext}}(\mathbf{r}) \tag{A.15}$$

with no loss of generality, where $\mathbf{j}$ and $\mathbf{A}^{\text{ext}}$ represent the current operator and external vector potential, respectively.

The current-current response function $\chi_{\mathbf{jj}}$ is obviously a tensor. Its elements $\chi_{j_\alpha j_\beta}$ can be calculated by means of Eq. (A.11) with the substitutions $\hat{A} = j_\alpha$ and $\hat{B} = j_\beta$, where Greek subscripts are used to denote vector components. The analogous to Eq. (A.9) then becomes

$$\langle j_\alpha \rangle(\mathbf{q}, \omega) = \sum_\beta \chi_{j_\alpha j_\beta}(\mathbf{q}, \omega) A^{\text{ext}}_\beta(\mathbf{q}, \omega)\,. \tag{A.16}$$

For isotropic systems, switching to a more convenient reference frame allows to simplify this description in terms of decoupled scalar variables. To do so, any vector $\mathbf{v}$ is to be spanned in its longitudinal (v_L) and transverse (v_T) components with respect to $\mathbf{q}$. Decomposing the Fourier transforms of the external vector potential $\mathbf{A}^{\text{ext}}(\mathbf{q})$ and current $\mathbf{j}(\mathbf{q})$ this way, the tensor $\chi_{\mathbf{jj}}$ becomes diagonal,[85]

$$\begin{bmatrix} \langle j_L \rangle(\mathbf{q}, \omega) \\ \langle j_T \rangle(\mathbf{q}, \omega) \end{bmatrix} = \begin{bmatrix} \chi_L(q, \omega) & 0 \\ 0 & \chi_T(q, \omega) \end{bmatrix} \begin{bmatrix} A^{\text{ext}}_L(\mathbf{q}, \omega) \\ A^{\text{ext}}_T(\mathbf{q}, \omega) \end{bmatrix}, \tag{A.17}$$

which results in the longitudinal and transverse responses being fully determined by the scalars χ_L and χ_T, respectively. These, in turn, exclusively encode the purely electric and purely magnetic phenomena. In fact, the independence of $\mathbf{B}(\mathbf{q})$ ($\mathbf{E}(\mathbf{q})$) on $A_L(\mathbf{q})$ ($A_T(\mathbf{q})$) straightforwardly follows from Maxwell's equations. As a consequence, χ_L and $\chi_{\rho\rho}$ are equivalent: the charge-continuity equation relates them, yielding

$$\chi_{\rho\rho}(q, \omega) = \frac{q^2}{\omega^2} \chi_L(q, \omega)\,. \tag{A.18}$$

In the following, thus, we will exclusively refer to the former as far as either longitudinal-current or charge-density phenomena are concerned.

As a last remark, it is important to mention that the current-current response function completely determines the electromagnetic properties of the system. Magnitudes like the conductivity

$$\sigma_{\alpha\beta}(\mathbf{q}, \omega) = \frac{ie^2}{\omega} \left[\frac{n}{m} \delta_{\alpha\beta} + \chi_{j_\alpha j_\beta}(\mathbf{q}, \omega) \right] \tag{A.19}$$

or the orbital magnetic susceptibility χ_{orb} (see Ch. 5) are two examples that can be directly calculated from them.

A.5 Interactions, the Random Phase Approximation and collective excitations

Non-interacting correlation functions can be obtained by the mere use of Eq. (A.11), setting H_0 in Eq. (A.1) equal to the Hamiltonian for free electrons H_{free}. When H_0 accounts for interactions, however, the calculation of the eigenstates may not be possible. As a consequence, response functions cannot be computed so straightforwardly.

Perturbation theory allows to avoid this setback. In general, it provides with an infinite series of terms whose sum yields the desired response function. As usual in perturbative analysis, truncating the series at a certain order may give less accurate analytical results than those obtained by partial summation. This last procedure discards the least relevant terms, but in contrast with the former, still retains an infinite number of them.

An example of paramount use in Condensed Matter Physics is the Random Phase Approximation (RPA). More particularly, we are interested in its application to the current-current response introduced in Appx. A.4. In the realm of interacting electron gases, there are different approaches that converge to the same description. Two examples restricted to the density-density correlation function are the seminal work presented by Bohm and Pines in Refs. [34,49] and its diagrammatic version, detailed in Ref. [205].

In this appendix, we proceed to outline yet another perspective based on a time-dependent Hartree theory. Ref. [85] lays it out focusing on the density-density response. Here, we will formulate it more generally, later aiming at its application also to the current-current correlation function. For this purpose, let us consider Eq. (A.1) with

$$H_0 = H_{\text{free}} + F^{\text{ind}}(t)\hat{B}\,, \tag{A.20}$$

where H_{free} represents the non-interacting Hamiltonian. $F^{\text{ind}}(t)$ corresponds to the field created by the system, in contrast with the external $F^{\text{ext}}(t)$. The total field is $F^{\text{total}} = F^{\text{ext}} + F^{\text{ind}}$. Interactions are thoroughly encoded in the second term of Eq. (A.20) through the dependence of $F^{\text{ind}}(t)$ on $\hat{B}$. The time-dependent Hartree theory consists of approximating

$$F^{\text{ind}}(t) \simeq \hat{D}(t)\langle\hat{B}\rangle(t)\,, \tag{A.21}$$

where $\hat{D}$ is the Green operator of the differential equation relating the field F to the magnitude $\langle\hat{B}\rangle$. Inserting Eq. (A.21) into Eq. (A.20) and using the definitions of Appx. A.1 with $\hat{A} = \hat{B}$, it is straightforward to reach the result

$$\chi^{\text{RPA}}_{BB}(\omega) = \frac{\chi^{(0)}_{BB}(\omega)}{1 - \hat{D}(\omega)\chi^{(0)}_{BB}(\omega)}\,, \tag{A.22}$$

where $\chi^{(0)}_{BB}$ is the non-interacting response function (namely the one obtained for $H_0 = H_{\text{free}}$). Also, simple manipulations yield the following expressions:

$$F^{\text{total}}(\omega) = \frac{F^{\text{ext}}(\omega)}{1 - \hat{D}(\omega)\chi^{(0)}_{BB}(\omega)}\,, \tag{A.23}$$

$$\langle \hat{B} \rangle(\omega) = \chi^{(0)}_{BB}(\omega) F^{\text{total}}(\omega)\,. \tag{A.24}$$

Instead of Eq. (A.21), some references adopt Eq. (A.24) as the definition of the RPA. Both perspectives are equivalent, although the former offers more physical insight in terms of a time-dependent Hartree approach.

A spatial dependence of the observables, $\hat{B}(\mathbf{r})$, can be handled as discussed in Appx. A.2, which yields the final expression

$$\chi^{\text{RPA}}_{BB}(\mathbf{q},\omega) = \frac{\chi^{(0)}_{BB}(\mathbf{q},\omega)}{1 - \hat{D}(\mathbf{q},\omega)\chi^{(0)}_{BB}(\mathbf{q},\omega)} \tag{A.25}$$

for homogeneous media, recalling that $\mathbf{q}$ can be replaced by q in the isotropic case. Eqs. (A.23) and (A.24) are likewise modified.

The application of this general result to the density-density response is immediate: Eq. (A.25) reduces to

$$\chi^{\text{RPA}}_{\rho\rho}(\mathbf{q},\omega) = \frac{\chi^{(0)}_{\rho\rho}(\mathbf{q},\omega)}{1 - v(\mathbf{q})\chi^{(0)}_{\rho\rho}(\mathbf{q},\omega)}\,, \tag{A.26}$$

when considering $\hat{B}(\mathbf{r}) = \rho(\mathbf{r})$ and the fact that the Green's function of the Poisson equation, $\nabla^2\phi = -\rho/\epsilon_0$, is the Coulomb potential $v(\mathbf{q})$.

As for the current-current correlation function, Eq. (A.25) can be used separately for the longitudinal and transverse channels due to the decoupling discussed in Appx. A.4,

$$\chi^{\text{RPA}}_{L,T}(\mathbf{q},\omega) = \frac{\chi^{(0)}_{L,T}(\mathbf{q},\omega)}{1 - d^0_{L,T}\chi^{(0)}_{L,T}(\mathbf{q},\omega)}\,. \tag{A.27}$$

For 2D media, which are our only concern throughout Ch. 2, the respective propagators d^0_L and d^0_T are[66]

$$d^0_L = \frac{q'}{2\epsilon\epsilon_0\omega^2}\,,\ d^0_T = -\frac{\mu\mu_0}{2q'}\,, \tag{A.28}$$

with

$$q' = \sqrt{q^2 - (n\omega/c)^2}\,, \tag{A.29}$$

where in turn n is the refractive index of the embedding medium, and ϵ and μ its relative electric permittivity and magnetic permeability.

We have been able to find response functions, Eq. (A.25) and its particular cases Eqs. (A.26) and (A.27), which encode interactions and therefore could manifest the existence of collective oscillations. Remarkably, the denominator of Eq. (A.25) can vanish for several values of $(\mathbf{q}, \omega)$, which actually suggests the existence of self-sustained excitations of the system with the respective wavelength and frequency. Indeed, the effect of this divergence in $\langle B \rangle_1(\mathbf{q}, \omega) = \chi^{\mathrm{RPA}}_{BB}(\mathbf{q}, \omega) F^{\mathrm{ext}}(\mathbf{q}, \omega)$ roughly reveals that $\langle \hat{B} \rangle_1(\mathbf{q}, \omega)$ may be nonzero even in the absence of external sources, $F^{\mathrm{ext}} = 0$.

A more rigorous analysis shows that excitations must be identified by the divergence of the loss function[66]

$$S(\mathbf{q}, \omega) \equiv -\mathrm{Tr}\left[\mathrm{Im}\left(\chi_{BB}(\mathbf{q}, \omega)\right)\right] \tag{A.30}$$

instead. Taking the imaginary part of the correlation function is motivated by the discussion of Appx. A.3: S is thereby related to the capacity of the system to absorb energy, which in turn indicates whether collective oscillations may exist. Taking the trace, on the other hand, manages to decouple the different oscillation modes, which becomes particularly important when dealing with tensorial response functions.

Throughout Ch. 2, the use of this magnitude is the key to describe the excitations associated to the current-current response functions, which receive the name of plasmons.

Appendix B

Spectrum and tight binding for MP-QDs

B.1 Wavefunctions of the bound states for $B \neq 0$

In this appendix, we present the general formulas necessary to solve the eigenvalue problem of a MP-QD. The general solution of Eq. (3.6) is given by

$$\chi_\sigma^\tau(r) = e^{-br^2/2} r^{n_\sigma} \begin{cases} \alpha_\sigma M\left[q_\sigma(m_1), 1+n_\sigma, br^2\right] & \text{for } r \leq R\,, \\ \beta_\sigma U\left[q_\sigma(m_2), 1+n_\sigma, br^2\right] & \text{for } r > R\,, \end{cases} \tag{B.1}$$

with

$$q_\sigma(m) = \frac{1}{4}\left[\frac{a_\sigma}{b} + 2(1+n_\sigma)\right] \tag{B.2}$$

and Eqs. (3.7) and (3.8). U and M are the confluent hypergeometric functions.[206] Since the wave function has to be non singular at the origin and square integrable, U (M) can only be a solution in the region $r > R$ ($r \leq R$). The ratio $\alpha_\sigma/\beta_\sigma$ is provided by the coupled equations resulting from inserting Eq. (3.5) in Eq. (3.1).

When imposing the continuity of the wave function at the frontier $r = R$,[207,208] the following conditions are obtained:

$$\begin{aligned} j > 0 \quad &\Rightarrow \frac{U(q_1(m_2), 1+n_1, bR^2)}{M(q_1(m_1), 1+n_1, bR^2)} = \\ &= \frac{\tau E + \Delta_1}{[\tau E + \Delta_2]\left(1 - \frac{q_1(m_1)}{1+n_1}\right)} \frac{U(q_{-1}(m_2), 1+n_{-1}, bR^2)}{M(q_{-1}(m_1), 1+n_{-1}, bR^2)}\,, \end{aligned} \tag{B.3}$$

$$\begin{aligned} j < 0 \quad &\Rightarrow \frac{U(q_{-1}(m_2), 1+n_{-1}, bR^2)}{M(q_{-1}(m_1), 1+n_{-1}, bR^2)} = \\ &= -\frac{(1+n_{-1})q_{-1}(m_2)[\tau E - \Delta_1]}{q_{-1}(m_1)[\tau E - \Delta_2]} \frac{U(q_1(m_2), 1+n_1, bR^2)}{M(q_1(m_1), 1+n_1, bR^2)}\,. \end{aligned} \tag{B.4}$$

These equations yield the allowed energies of the bound states.

It is possible to relate the solution of Eq. (3.6) —MP-QDs— and of Eq. (3.9) —PW-QDs—. The substitution

$$E \to E - U(r)\,,\ \Delta_{1,2} \to \Delta_0\,,\ m_1 \to m_2\,, \tag{B.5}$$

in Eq. (B.1) provides the wave functions of Eq. (3.9). The matching conditions then yield Eqs. (B.3) and (B.4) but with the changes

$$\tau E \pm \Delta_1 \to \tau(E - U_0) \pm \Delta_0\,, \tag{B.6}$$

$$\tau E \pm \Delta_2 \to \tau E \pm \Delta_0\,. \tag{B.7}$$

Moreover, in Eq. (3.7) when inserted in Eq. (B.2), $E \to E - U_0$ for $q_\sigma(m_1)$ whereas $E \to E$ for $q_\sigma(m_2)$. The whole set of substitutions can be understood under the following consideration: focusing on Eqs. (B.3) and (B.4), the different masses m_1 and m_2 only appear for the regions $r \leq R$ and $r > R$, respectively. In order to obtain the solution of a PW-QD, we thus change $E \to E - U_0$ only in the case $r \leq R$. On the other hand, $m_1 \to m_2$, i.e., $\Delta(r) \to \Delta_0$, holds everywhere.

The electron-hole symmetry of the solution for MP-QDs can be inferred directly from Eqs. (B.3) and (B.4). They depend on the energy solely through the variable τE. Therefore, given a state with (E, τ, j), another with $(-E, -\tau, j)$ exists. Nevertheless, this symmetry is broken in PW-QDs. The reason is that the substitutions given by Eqs. (B.6) and (B.7) in Eqs. (B.3) and (B.4) split the dependence on τE into τ and E separately.

Plots of the wave function components appear in Fig. B.1. In the upper panels, the effect of increasing the magnetic field is analyzed. A polarization of the B-sublattice takes place in both valleys as well as the quenching of the kinetic energy with magnetic field is revealed as a shift of the radial probability towards the center of the well. The lower panels, on the other hand, focus on levels with different j values at a fixed field B. The increase in the total angular momentum J_z entails a shift of the radial probability away from the center of the dot. This is in agreement with the lower localization of the states with energies closer to the top of the well.

B.2 Wavefunctions of the bound states for $B = 0$

In the case of $B = 0$, Eq. (B.1) reduces to

$$\chi_\sigma^\tau(r) = \begin{cases} \delta_\sigma J_{j-\sigma/2}\left[k(m_1)r\right] & \text{for } r \leq R\,, \\ \gamma_\sigma H^{(1)}_{j-\sigma/2}\left[i\,k(m_2)r\right] & \text{for } r > R\,. \end{cases} \tag{B.8}$$

In turn,

$$k(m) \equiv \sqrt{|(\tau E - m v_F^2)(\tau E + m v_F^2)|}/\hbar v_F \tag{B.9}$$

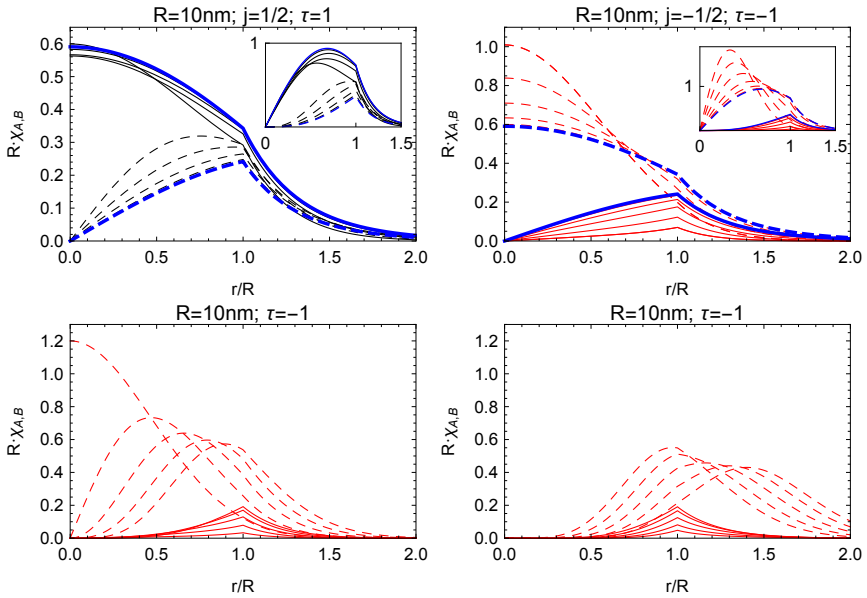

Figure B.1: Components of the MP-QD wave function, Eqs. (B.1) and (3.5). Solid (dashed) lines refer to the A (B) sublattice. Upper panels: Plots for different values of the magnetic field B. The blue curves correspond to zero magnetic field ($B = 0$), whereas black ($\tau = 1$) and red ($\tau = -1$) curves show the eigenfunctions at finite magnetic field for $R/l_B = \{1, 1.5, 2\}$: greater values of R/l_B are respective to the more deviated curves from the blue ones. For comparison, an extra solution for $R/l_B = 2.5$ in the regime with only $\tau = -1$ levels has been plotted for $\tau = -1$. The insets depict the radial probability ($2\pi r R|\chi_{A,B}|^2$ vs. r/R) associated to the wave functions. Lower panels: Plots for $R = 10\,\text{nm}$, $R/l_B = 3$, corresponding to the region where only $\tau = -1$ levels are present and different values of j. Left plot: $j = \{-1/2, -3/2, -5/2, -7/2, -9/2\}$ corresponding to A (B) sublattice curves ordered from bottom (left) to top (right). Right plot: $j = \{-11/2, -13/2, -15/2, -17/2, -19/2\}$ corresponding to A (B) sublattice curves ordered from top (left) to bottom (right).

and $J_{j-\sigma/2}$ and $H^{(1)}_{j-\sigma/2}$ are the Bessel functions and the Hankel functions of the first kind as defined in Ref. [206]. The ratio $\delta_\sigma/\gamma_\sigma$ is calculated analogously to $\alpha_\sigma/\beta_\sigma$ in appendix B.1.

The continuity condition for the wave function yields in this case

$$\begin{aligned} &i\,\tau\,\mathrm{sg}(E)\eta(m_2)J_{j-1/2}\left[k(m_1)R\right]H^{(1)}_{j+1/2}\left[i\,k(m_2)R\right] = \\ &= \eta(m_1)J_{j+1/2}\left[k(m_1)R\right]H^{(1)}_{j-1/2}\left[i\,k(m_2)R\right]\,, \end{aligned} \tag{B.10}$$

which again gives the allowed energies of the bound states. We also defined

$$\eta(m) \equiv \sqrt{\left|\frac{\tau E - m v_F^2}{\tau E + m v_F^2}\right|}\,. \tag{B.11}$$

The considerations regarding the electron-hole symmetry which are related to the τE dependence also apply here, see appendix B.1. Moreover, the properties of Bessel and Hankel functions

$$J_{-n}(z) = (-1)^n J_n\,,\ H^{(1)}_{-\nu}(z) = e^{\nu\pi i}H^{(1)}_{\nu}(z)\,, \tag{B.12}$$

together with

$$\frac{\eta(m_1)}{\eta(m_2)} \xrightarrow{\tau\to-\tau} \frac{\eta(m_2)}{\eta(m_1)} \tag{B.13}$$

allow to prove the double degeneracy of levels, i.e., a solution with (E,τ,j) implies the existence of another with $(E,-\tau,-j)$. In contrast with the electron-hole symmetry, the substitutions of Eqs. (B.6) and (B.7) in (B.10) (yielding a PW-QD) do not lift this degeneracy.

As we mention in the main text and show in Figs. 3.4 and 3.5, a splitting happens when a magnetic field is applied. Plots of several wave functions and their corresponding radial probabilities are shown in Fig. B.2.

B.3 Tight binding in a lattice of MP-QDs

Our aim is to construct a tight-binding model for a system in which the overlap λ of neighboring wave functions cannot be neglected. This is motivated by Fig. B.3, which plots the overlap for a couple of quantum dots as a function of the distance. As a start point, we will discard terms which are cubic or of higher order in λ. Actually, we will show that $O(\lambda^2)$ terms will be significant in packed lattices of quantum dots.

Let $|n\rangle$ be the wave function of a particular state of a single well located at a certain position. The set S containing all kets $|n\rangle$ respective to every lattice site and every energy level is not orthonormal because the overlap $\langle n|n'\rangle$ between neighbors is not negligible. However, the Gram-Schmidt

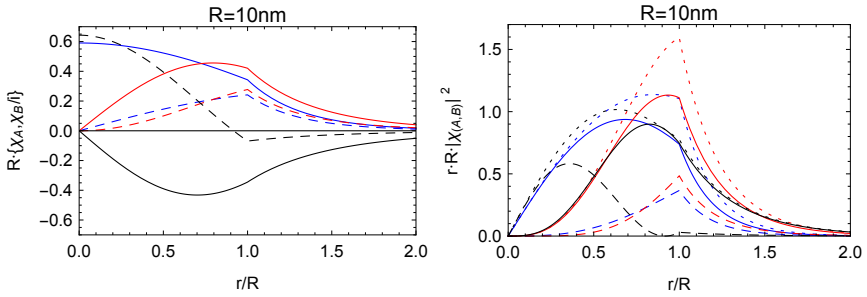

Figure B.2: Components of the wave function (left hand side), Eqs. (3.5) and (B.8), and their associated radial probabilities (right hand side) for $\tau = 1$ and $j = 1/2$ (blue), $j = 3/2$ (red) and $j = -1/2$ (black). Solid (dashed) lines correspond to the A (B) sublattice, and dotted lines to the total radial density probability. A wave function with $\tau = -1$ and $j = -1/2$ is also plotted in Fig. B.1 (right hand side of upper panel).

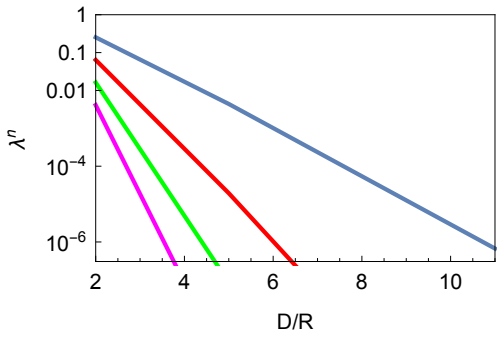

Figure B.3: Powers of the overlap, λ^n, between wave functions belonging to wells whose centers lie at a distance D. $n = 1, 2, 3, 4$ correspond to blue, red, green and magenta.

algorithm allows to obtain an orthonormal basis S' by linear combinations of the vectors belonging to S. Denoting the elements of S' by $|f_n\rangle$, we can write the identity as

$$I = \sum_n |f_n\rangle\langle f_n| \,. \tag{B.14}$$

Carrying out the algorithm to obtain $|f_n\rangle$, the unity operator in terms of the S-basis vectors only including correction terms to lowest orders reads

$$I = \sum_n |n\rangle\langle n| - \sum_{j\neq n} \langle j|n\rangle |j\rangle\langle n| \,. \tag{B.15}$$

To express the Hamiltonian in the original basis S, we will use this representation of the identity operator.

Let us apply the aforementioned procedure to a set of N MP-QDs whose centers are located at $\mathbf{R}_i$ with $i = 1, \ldots, N$. We will consider wells that only have one valence and conduction bound state with energy $\pm E$ ($E > 0$) and $j = \pm 1/2$ (cf. Fig. 3.3). Therefore, we can unambiguously label the S states by $|\pm\mathbf{R}_i\rangle$.

We define the following parameters, describing the hopping processes depicted in Fig. 3.6:

$$\lambda_{ij}^{\pm} = \langle \pm\mathbf{R}_i | \pm\mathbf{R}_j \rangle \,, \tag{B.16}$$

$$\xi^{\pm} = \langle \pm\mathbf{R}_i | \Delta U_i | \pm\mathbf{R}_i \rangle \,, \tag{B.17}$$

$$\eta^{\pm} = \langle \pm\mathbf{R}_i | \Delta U_i | \mp\mathbf{R}_i \rangle \,, \tag{B.18}$$

$$\kappa_{ij}^{\pm} = \langle \pm\mathbf{R}_i | \Delta U_j | \pm\mathbf{R}_j \rangle \,, \tag{B.19}$$

$$\mu_{ij}^{\pm} = \langle \pm\mathbf{R}_i | \Delta U_j | \mp\mathbf{R}_j \rangle \,. \tag{B.20}$$

Assuming inversion symmetry for the array under consideration and making use of the properties of the wave functions, the following identities can be proved:

$$\{\lambda_{ij}^{\pm}, \xi^{\pm}, \kappa_{ij}^{\pm}\} \in \mathbb{R} \,,\ \lambda_{ij}^{+} = \lambda_{ij}^{-} \equiv \lambda_{ij} \,,\ \lambda_{ij} = \lambda_{ji} \,, \tag{B.21}$$

$$\xi^{+} = -\xi^{-} \,,\ \eta^{\pm} = 0 \,,\ \kappa_{ij}^{+} = -\kappa_{ij}^{-} \,,\ \kappa_{ij}^{\pm} = \kappa_{ji}^{\pm} \,, \tag{B.22}$$

$$\mu_{ij}^{\pm} \equiv \mu^{\pm}(\mathbf{R}_i - \mathbf{R}_j) = \mu^{\pm}(|\mathbf{R}_j - \mathbf{R}_i|\hat{x}) e^{\pm i\theta_{\mathbf{R}_j - \mathbf{R}_i}} \,, \tag{B.23}$$

$$\mu^{\pm}(|\mathbf{R}_j - \mathbf{R}_i|\hat{x}) \in \mathbb{R} \,,\ \mu_{ij}^{+} = -\mu_{ij}^{-*} . \tag{B.24}$$

$\hat{x}$ is the unitary vector in the x direction, $\theta_{\mathbf{R}_j - \mathbf{R}_i}$ is the angle between $\mathbf{R}_j - \mathbf{R}_i$ and $\hat{x}$ and $h(\mathbf{R}_i - \mathbf{R}_j) \equiv h_{ij}$, where $h = \lambda^{\pm}, \kappa^{\pm}, \mu^{\pm}$. In turn,

$$\Delta U_j = H - H_{\mathbf{R}_j}, \tag{B.25}$$

$H = \sum_i H_{\mathbf{R}_i}$ being the total Hamiltonian and $H_{\mathbf{R}_j}$ the Hamiltonian of a single MP-QD centered at $\mathbf{R}_j$. ΔU_j accounts then for the influence of the

lattice on the Hamiltonian of an isolated dot and results in the hopping of electrons between different wells.

The dependence of Eqs. (B.16)-(B.20) on D/R, where D is the distance between the centers of the dots, is plotted in Fig. 3.7 for a double MP-QD. It can be seen that $\mu, \kappa < \lambda(m_2 - m_1)v_F^2$ and $\xi < \lambda^2(m_2 - m_1)v_F^2$, which will be taken into account when discarding terms of greater order than λ^2 in subsequent calculations.

Under these considerations and with Eq. (B.15), the Hamiltonian acting on $|\pm\mathbf{R}_m\rangle$ can be expressed as

$$\begin{aligned} H|\pm\mathbf{R}_m\rangle &= (H_{\mathbf{R}_m} + I\cdot\Delta U_m)\,|\pm\mathbf{R}_m\rangle = \\ &= \left[\pm|E| + \xi^{\pm} - \sum_{i\neq m}\lambda_{mi}\kappa_{im}^{\pm}\right]|\pm\mathbf{R}_m\rangle \\ &+ \sum_{j\neq m}\left[\kappa_{jm}^{\pm} - \xi^{\pm}\lambda_{jm} - \sum_{i\neq\{j,m\}}\lambda_{ji}\kappa_{im}^{\pm}\right]|\pm\mathbf{R}_j\rangle \\ &+ \sum_{j\neq m}\left[\mu_{jm}^{\pm} - \sum_{i\neq\{j,m\}}\lambda_{ji}\mu_{im}^{\pm}\right]|\mp\mathbf{R}_j\rangle \\ &- \sum_{j\neq m}\lambda_{mj}\mu_{jm}^{\pm}|\mp\mathbf{R}_m\rangle\,. \end{aligned} \tag{B.26}$$

Eq. (B.26) gives the matrix elements of H in the S basis for a still unspecified geometry of the quantum dot set.

This general result can be applied to different systems. The simplest consists in only two coupled MP-QDs. Its spectrum, with the individual energy levels split, appears in Fig. 3.7. One can see there that for $D \lesssim 4R$, the influence of $O(\lambda)$ terms is significant, although there is not a great difference between neglecting λ^2 and λ^3 terms even at small distances between the wells. Second order processes, however, will be more relevant in lattices due to the assistance of next-nearest neighbor hopping processes. In this respect, see the following discussion and Fig. B.4.

For a periodic system of MP-QDs, it is more convenient to work in a Fourier transformed basis defined by

$$|\pm\mathbf{R}\rangle = \frac{1}{2\pi}\int d^2k\; e^{i\mathbf{k}\cdot\mathbf{R}}|\pm\mathbf{k}\rangle. \tag{B.27}$$

Inserting Eq. (B.27) in Eq. (B.26), the Hamiltonian can be expressed in

block diagonal form. The block respective to $\mathbf{k}$ reads

$$H(\mathbf{k}) \equiv \begin{bmatrix} \langle -\mathbf{k}|H|-\mathbf{k}\rangle & \langle -\mathbf{k}|H|+\mathbf{k}\rangle \\ \langle +\mathbf{k}|H|-\mathbf{k}\rangle & \langle +\mathbf{k}|H|+\mathbf{k}\rangle \end{bmatrix} = \\ = \begin{bmatrix} h_1^- + \sum_\delta h_{2,\delta}^- e^{i\mathbf{k}\cdot\delta} & \sum_\delta h_{3,\delta}^- e^{i\mathbf{k}\cdot\delta} \\ \sum_\delta h_{3,\delta}^+ e^{i\mathbf{k}\cdot\delta} & h_1^+ + \sum_\delta h_{2,\delta}^+ e^{i\mathbf{k}\cdot\delta} \end{bmatrix}. \tag{B.28}$$

Dropping the subscripts, δ is defined by

$$\delta = \mathbf{R}_j - \mathbf{R}_m \tag{B.29}$$

choosing the adequate j and m. We have also defined correspondingly

$$h_1^\pm = \pm|E| + \xi^\pm - \sum_{i\neq m} \lambda_{mi}\kappa_{im}^\pm\,, \tag{B.30}$$

$$h_{2,\delta}^\pm = \kappa_{jm}^\pm - \xi^\pm\lambda_{jm} - \sum_{i\neq\{j,m\}} \lambda_{ji}\kappa_{im}^\pm\,, \tag{B.31}$$

$$h_{3,\delta}^\pm = \mu_{jm}^\pm - \sum_{i\neq m} \lambda_{ji}\mu_{im}^\pm. \tag{B.32}$$

The following identities, the last of which guarantees the hermiticity of the Hamiltonian, can be proved attending to the symmetry of the wave functions and ΔU_j:

$$h_1^+ = -h_1^-,\ h_{2,\delta}^+ = -h_{2,\delta}^-,\ h_{3,\delta}^+ = {h_{3,-\delta}^-}^*. \tag{B.33}$$

We can apply the general result Eq. (B.28) to the simplest lattice, namely a one-dimensional chain with a single atom per node. To do so, we must determine the relevant processes which contribute significantly to Eqs. (B.30)-(B.32). That analysis was carried out and is summarized in Fig. B.4.

There, we see that departing from the criterion of neglecting λ^2, only the direct processes κ and μ between neighboring wells are relevant. However, as long as the chain lattice parameter becomes close to the diameter of the wells, $O(\lambda^2)$ processes become increasingly more relevant. In particular, a next-nearest neighbor (nnn) hopping process is assisted by the wave function overlap, whereas direct processes to nnn are negligible.

Once we have discarded all irrelevant terms in Eqs. (B.30)-(B.32), we can diagonalize Eq. (B.28) to obtain the bands and the tight-binding description is complete. Spectra for various lattice parameters are plotted in Fig. 3.8.

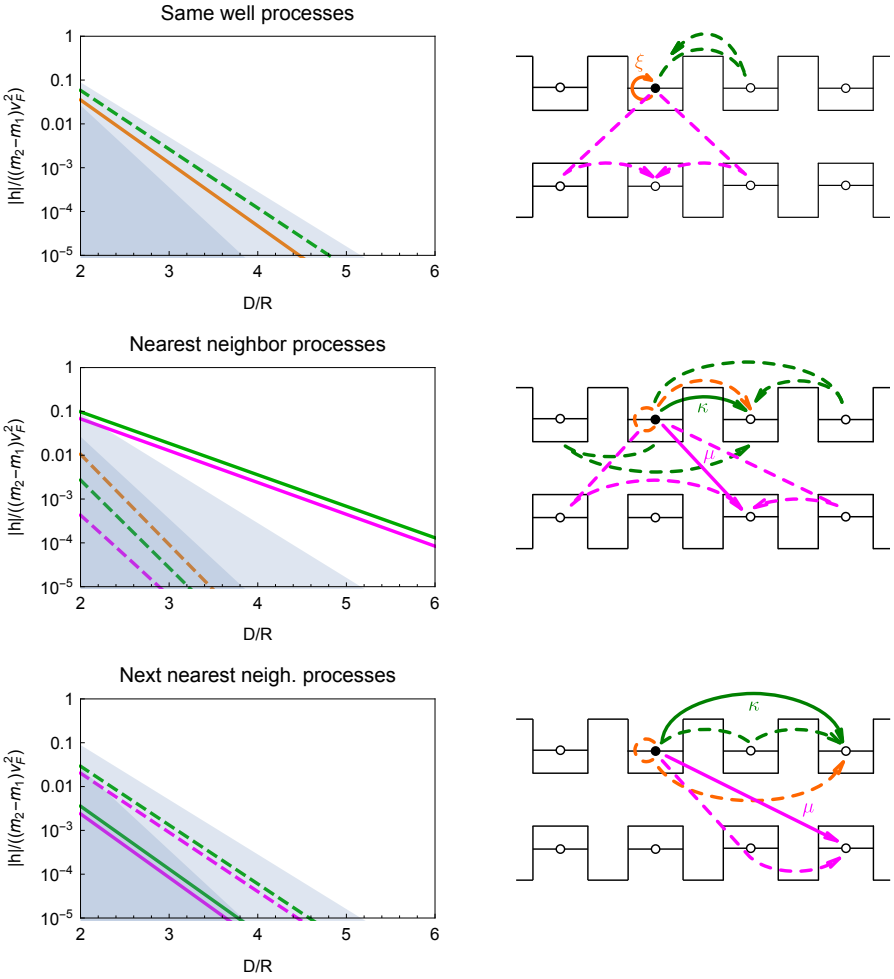

Figure B.4: Analogous to Fig. 3.7. Hopping processes to the same well, to a nearest neighbor or to a next-nearest neighbor are analyzed separately. The sketches on the right give the legend of the plots on the left. Solid lines correspond to direct processes, and dashed lines to processes assisted by λ together with a direct hopping, i.e., terms of the kind $\sum_{i,j,m} \lambda_{ji} h^{\pm}_{im}$ appearing in Eq. (B.26) ($h = \xi, \kappa, \mu$). When in each right outline several processes are labeled by a single line style, the associated curve on the left plot corresponds to the sum of their probability amplitudes. In the upper left plot, the magenta processes do not appear because the sum of their amplitudes vanishes due to Eq. (B.23). In the bottom left plot, the amplitude of the orange process is not identically zero, but so small that lies outside the plot range. For shadowed regions, see Fig. 3.7.

Appendix C

Wave solution and reflection phase shift in an hBN spheroid

C.1 Electromagnetic solution of the resonances

In this appendix, we sketch the solution of the electromagnetic problem for an hBN granule embedded in vacuum. The contour conditions for the scalar potential Φ will be applied to a prolate spheroid with its symmetry axis parallel to the z axis of the permittivity tensor.

The inside and outside regions delimited by the surface will be associated to the subscripts 1 and 2, respectively. Assuming that the size of the granule is much smaller than c/ω, the quasi-static approximation for the electric field is justified, $\mathbf{E}_i \simeq -\partial_{\mathbf{r}}\Phi_i$. When inserted in $\nabla \cdot \mathbf{D} = 0$ with $\mathbf{D} = \hat{\epsilon}\,\mathbf{E}$, this yields the Walker equation[144] for the inner potential,

$$\left[\epsilon_z \partial_z^2 + \epsilon_\perp(\partial_x^2 + \partial_y^2)\right] \Phi_1 = 0\,, \tag{C.1}$$

whereas the outer potential satisfies Laplace's, $\nabla^2\Phi_2 = 0$.

Given the geometry of the problem, it is convenient to work in renormalized ellipsoidal coordinates. They are defined by Eqs. (4.10) for the inside region (see also Fig. 4.5) and Eqs. (4.16) for the outside. The aforementioned differential equations become separable, and the analytical solution can be written as[144,165,178]

$$\Phi_1 \propto P_l^m(\cos\xi) P_l^m(\cos\theta) e^{im\psi}\,, \qquad 0 < \xi < \bar{\xi}\,, \tag{C.2}$$

$$\Phi_2 \propto Q_l^m(\cosh\eta) P_l^m(\cos\theta) e^{im\psi}\,, \qquad \eta > \bar{\eta}\,. \tag{C.3}$$

Here, $l \geq 0$ and $|m| \leq l$ are integers, and $P_l^m(z)$ and $Q_l^m(z)$ are the associated Legendre functions of the first and the second kinds, respectively.[206]

Turning to the application of the boundary conditions, the potential and the normal component of the displacement vector $\mathbf{D}$ must be continuous at

the surface:[144,165]

$$\Phi_1(\bar{\xi},\theta,\psi) = \Phi_2(\bar{\eta},\theta,\psi)\,, \tag{C.4}$$

$$\frac{\epsilon_z}{\sqrt{1-g_1}}\left.\frac{\partial\Phi_1}{\partial(\cos\xi)}\right|_{\xi=\bar{\xi}} = \frac{1}{\sqrt{1-g_2}}\left.\frac{\partial\Phi_2}{\partial(\cosh\eta)}\right|_{\eta=\bar{\eta}}\,, \tag{C.5}$$

with the definition $g_i = \frac{a_\perp^2}{a_z^2}\frac{\epsilon_{z,i}^2}{\epsilon_{\perp,i}}$ and subscripts $i = 1, 2$ referring to hBN and vacuum, respectively.

The above requirements can be merged into the final equation

$$i\sqrt{\epsilon_\perp}\sqrt{\epsilon_z}\frac{d}{d\bar{\xi}}\ln P_l^m(\cos\bar{\xi}) = \frac{d}{d\bar{\eta}}\ln Q_l^m(\cosh\bar{\eta})\,. \tag{C.6}$$

Note that this expression depends only on the aspect ratio and not the size of the spheroid, which is consistent with the scale invariance of Eq. (C.1). Bearing in mind Eqs. (4.2) and (4.11), Eq. (C.6) gives several solutions for the eigenfrequency ω for each l and m, as we proceed to show. They will be labeled with three indices, in turn related to the quantum numbers arising from the EBK conditions, see Sec. 4.4.

For that purpose and following Ref. [144], Eq. (C.6) can be rewritten as

$$\epsilon_z\left(\frac{|m|}{\tan^2\bar{\xi}}+k+\sum_{i=1}^{N}\frac{2}{x_i^2\tan^2\bar{\xi}-1+x_i^2}\right) = \\ -\cosh\bar{\eta}\frac{d}{d\cosh\bar{\eta}}\ln Q_l^m(\cosh\bar{\eta})\,, \tag{C.7}$$

where $0 < x_i < 1$ are the positive roots of the associated Legendre function $P_l^m(x)$ sorted in ascending order, $N = [(l-|m|)/2]$ is the number of such roots, $[z]$ is the integer part of z, and $k = 2N - n + |m|$ is either 0 or -1.

The right-hand side of Eq. (C.7) is a positive finite number,[165] while the left-hand side is a sum over poles that occur at

$$\tan^2\bar{\xi} = x_i^{-2} - 1\,. \tag{C.8}$$

In addition, there is another pole at $\tan^2\bar{\xi}$ if $m \neq 0$. It is easy to see then that Eq. (C.7) may have multiple solutions, as stated above. In hBN, the hyperbolic response occurs in two separate frequency ranges. For the upper reststrahlen band, as the frequency ω changes from $\omega_{TO,\perp}$ to $\omega_{LO,\perp}$, $\epsilon_\perp$ varies from $-\infty$ to 0, while ϵ_z is positive and approximately constant. To find the number of solutions of Eq. (C.7), one just counts the number of the poles crossed by $\tan^2\bar{\xi}$ as the frequency is increased. We can index these solutions by an integer n which is equal to zero if the pole is at $\tan^2\bar{\xi} = 0$ and equal to i if the pole originates from x_i —Eq. (C.8)—. One concludes that n runs from 1 to N for $m = 0$ and from 0 to N for $m \neq 0$. At frequencies that belong to the lower band, hBN behaves as a type-I HM, namely with $\epsilon_\perp > 0$

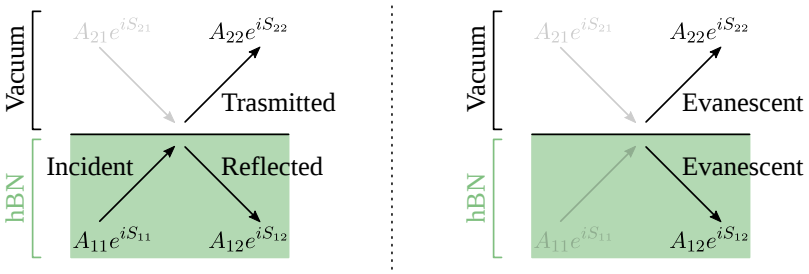

Figure C.1: Outlines of the hBN-vacuum interface depicting internal reflection and refraction (left) and surface modes (right). Faint arrows correspond to neglected terms in Eqs. (C.10)-(C.12).

and $\epsilon_z < 0$, and a similar analysis yields n running from 1 to $l - |m| - N$. Therefore, the total number of solutions in both bands together is equal to l for $m = 0$ and $l - |m| + 1$ for $m \neq 0$.

As has been shown, the modes can be unambiguously labeled by the indices (n, l, m), associated to radial oscillations, the total angular momentum and its projection on the z axis, respectively. A thorough discussion can be found in Ref. [165], and the application to the experiment described in Sec. 4.2 is detailed in Ref. [29]. Some plots of the solutions extracted from the latter have been reproduced in Fig. 4.4.

C.2 Phase shift of internal reflections and evanescent modes

In this appendix, we will compute the phase shift of polaritons after a reflection at a spheroidal surface, as well as the condition to encounter evanescent modes. In contrast to the approach in Appx. C.1, the potentials Φ_j must be separated into a component propagating towards the surface and another getting away from it:

$$\Phi_j = A_{j1}e^{iS_{j1}} + A_{j2}e^{iS_{j2}}\,, \quad j = 1, 2. \tag{C.9}$$

Here, the first index in the phases S_{jk} and amplitudes A_{jk} labels the medium, whereas the second distinguishes between incident and reflected waves. The notation is established in the outlines of Fig. C.1.

Inserting the potentials into the boundary conditions —Eqs. (C.4) and (C.5)— yields

$$S_{11} + S_{12} = S_{21} + S_{22}\,, \tag{C.10}$$

$$A_{11} + A_{12} = A_{21} + A_{22}\,, \tag{C.11}$$

$$i\sqrt{\epsilon_\perp}\sqrt{\epsilon_z}\left(A_{11}\frac{\partial S_{11}}{\partial \xi} + A_{12}\frac{\partial S_{12}}{\partial \xi}\right) = A_{21}\frac{\partial S_{21}}{\partial \eta} + A_{22}\frac{\partial S_{22}}{\partial \eta}\,. \tag{C.12}$$

To determine the coefficients accompanying A_{jk}, we count on the eikonal equations, namely Eq. (4.8) for hBN and Laplace's equation for vacuum.* Their solution was calculated in Sec. 4.3 by means of Hamiltonian optics: $\nabla S_{jk} = \mathbf{p}$, with $\mathbf{p}$ respectively given by Eqs. (4.14) and (4.19). The sign of $\mathbf{p}$ must be chosen according to the propagating direction, see outlines in Fig. C.1.

Under these considerations, it is straightforward to solve the linear system of equations for the amplitudes A_{jk} in different cases. As for internal reflections, A_{21} must be set equal to 0, see the left sketch in Fig. C.1. Then, the phase shift δ can be calculated as $e^{i\delta} = A_{12}/A_{11}$, resulting in Eq. (4.23).

Concerning the existence of surface modes, the outline of Fig. C.1 (right) applies: all waves propagating towards the surface must be discarded, and therefore $A_{11} = A_{21} = 0$. The equations for the amplitudes then yield

$$i\sqrt{\epsilon_\perp}\sqrt{\epsilon_z}p_\xi = p_\eta\,. \tag{C.13}$$

In this case, both p_η and p_ξ are purely imaginary, as expected, accounting for the evanescence of the modes away from the surface. This condition was used in Sec. 4.3.3 to obtain the effective surface Hamiltonian.

*Recall from Sec. 4.3 that these are only valid in the large wavevector limit, which is the case of our concern.

Appendix D

Magnetic response of tight-binding models

We summarize the formalism used to obtain the magnetic response[45] for arbitrary tight-binding models. Particular attention is paid to show its gauge-invariant nature.

D.1 Hamiltonian and gauge invariance

We consider a generic tight-binding Hamiltonian in a 3D lattice

$$H = \sum_{i,j} h_{ij} \, |i\rangle\langle j| \, , \tag{D.1}$$

where $i(j)$ runs over all orbitals in the lattice. $|i\rangle$ is a shorthand for the state $|\mathbf{r}_i, \alpha_i\rangle$, located at the position $\mathbf{r}_i$ and with orbital index α_i, one for each orbital in the unit cell. It is convenient to consider this discrete set as part of the usual continuum $\langle \mathbf{r}, \alpha | \mathbf{r}', \alpha' \rangle = \delta(\mathbf{r} - \mathbf{r}')\delta_{\alpha\alpha'}$, where $|\mathbf{r}, \alpha\rangle$ is the eigenstate of the position operator for the orbital index α, $\mathbf{R}_\alpha$, with conjugate momentum $\mathbf{P}_\alpha$. They satisfy canonical commutation relations, $[\hat{\mathbf{n}} \cdot \mathbf{R}_\alpha, \ \hat{\mathbf{n}} \cdot \mathbf{P}_{\alpha'}] = i\,\hbar\,\delta_{\alpha\alpha'}$, $\hat{\mathbf{n}}$ being an arbitrary unit vector. Notice that they are diagonal in orbital index.

In the absence of a magnetic field we have

$$|\mathbf{r} + \mathbf{a}, \alpha\rangle = e^{-\frac{i}{\hbar}\mathbf{a}\cdot\mathbf{P}} \, |\mathbf{r}, \alpha\rangle \, , \tag{D.2}$$

with $\mathbf{P} = \sum_\alpha \mathbf{P}_\alpha$. In the presence of a magnetic field with vector potential $\mathcal{A}(\mathbf{r})$ and operator $\mathbf{A}(\mathbf{R}) = \sum_\alpha \int d^3r \mathcal{A}(\mathbf{r}) |\mathbf{r}, \alpha\rangle\langle \mathbf{r}, \alpha|$, the replacement $\mathbf{P} \to \mathbf{\Pi} = \mathbf{P} - e\mathbf{A}(\mathbf{R})$, where $\mathbf{R} = \sum_\alpha \mathbf{R}_\alpha$, changes Eq. (D.2) to

$$e^{-\frac{i}{\hbar}\mathbf{a}\cdot\mathbf{\Pi}} \, |\mathbf{r}, \alpha\rangle = e^{i\phi(\mathbf{r}, \mathbf{r}+\mathbf{a})} |\mathbf{r} + \mathbf{a}, \alpha\rangle \, , \tag{D.3}$$

with the Berry phase for parallel transport becoming here the usual Peierls phase, $\phi(\mathbf{r}, \mathbf{r}') = \frac{e}{\hbar} \int_{\mathbf{r}}^{\mathbf{r}'} d\mathbf{l} \cdot \mathcal{A}$.

The original Hamiltonian in the absence of the field becomes in the presence of the field

$$H = \sum_{i,j} h_{ij} \, |\mathbf{r}_i, \alpha_i\rangle\langle \mathbf{r}_i, \alpha_j| \, e^{\frac{i}{\hbar}\delta_{ij}\cdot\mathbf{\Pi}} \,, \tag{D.4}$$

with $\delta_{ij} = \mathbf{r}_j - \mathbf{r}_i$. This manifestly gauge-invariant form is due to both the presence of $\mathbf{\Pi}$ and the shared location of bra and ket in Eq. (D.4).

D.2 Current operator and replicas

The previous formulation provides a unique, unambiguous prescription for the current operator anywhere in space. Let us consider a single oriented hopping term,

$$H_{ij} = h_{ij} \, |\mathbf{r}_i, \alpha_i\rangle\langle \mathbf{r}_i, \alpha_j| \, e^{\frac{i}{\hbar}\delta_{ij}\cdot\mathbf{\Pi}} \,. \tag{D.5}$$

The current operator, given by $\mathbf{J}(\mathbf{r}) = -\frac{\delta H}{\delta \mathcal{A}(\mathbf{r})}$, leads for H_{ij} to

$$\begin{aligned} \mathbf{J}_{ij}(\mathbf{r}) = \frac{ie}{\hbar} h_{ij} \, \delta_{ij} |\mathbf{r}_i, \alpha_i\rangle\langle \mathbf{r}_i, \alpha_j| \int_0^1 ds \\ \times \, e^{\frac{i}{\hbar}s\delta_{ij}\cdot\mathbf{\Pi}} \, |\mathbf{r}, \alpha_j\rangle\langle \mathbf{r}, \alpha_j| \, e^{\frac{i}{\hbar}(1-s)\delta_{ij}\cdot\mathbf{\Pi}} \,, \end{aligned} \tag{D.6}$$

where the relation $\delta e^K = \int_0^1 ds \; e^{sK} \; \delta K \; e^{(1-s)K}$ has been used for dealing with non- commuting operators K and δK.[80] The point of writing the current in this form is to exhibit its gauge-invariant nature. A more familiar expression would be

$$\begin{aligned} \mathbf{J}_{ij}(\mathbf{r}) = \frac{ie}{\hbar} h_{ij} \delta_{ij} e^{-i\phi(\mathbf{r}_i, \mathbf{r}_j)} |\mathbf{r}_i, \alpha_i\rangle\langle \mathbf{r}_j, \alpha_j| \\ \times \int_0^1 ds \delta(\mathbf{r}_i - \mathbf{r} + s \, \delta_{ij}) \,, \end{aligned} \tag{D.7}$$

where the last integral fixes the straight line between $\mathbf{r}_i$ and $\mathbf{r}_j$ as the loci for non zero currents: the familiar network picture now for quantum operators. The continuity equation holds everywhere with source and drain end points.

The extreme localization of the network-like current was found inconvenient for the perturbative approach,[45] and a continuum of replicas of the original system obtained by displacing the reference lattice by ρ, taken uniformly within the unit cell, was introduced,

$$H = \frac{1}{N} \sum_{i,j} h_{ij} \int d^3\rho \, |\mathbf{r}_i + \rho, \alpha_i\rangle\langle \mathbf{r}_i + \rho, \alpha_j| e^{\frac{i}{\hbar}\delta_{ij}\cdot\mathbf{\Pi}} \,, \tag{D.8}$$

N being the total number of cells. Replicas labeled by ρ are different modulo a lattice vector, allowing ρ to span all space after appropriate normalization.

Different replicas are dynamically independent: a particle in one of them will hop in its own discrete lattice, unaware of any of the other replicas, allowing the average to be taken at the Hamiltonian level. The lattice is displaced but the field is kept in place: each replica experiences a slightly different field, and the process can be interpreted alternatively as an average over slightly displaced fields. This replication will leave properties of the original problem virtually unaffected, unless the field changes drastically at the lattice length scale, a situation where even the tight-binding Hamiltonian is questionable. Furthermore, a translation amounts to a gauge transformation for a uniform magnetic field, leaving physical properties intact. Irrespective of its origin, the manifestly gauge-invariant Hamiltonian of Eq. (D.8), leads to the following gauge-invariant current operator, unambiguously defined everywhere in space,

$$\mathbf{J}(\mathbf{r}) = \frac{ie}{\hbar}\frac{1}{N}\sum_i\sum_j h_{ij}\delta_{ij}\int d^3\rho\,|\mathbf{r}_i+\rho,\alpha_i\rangle\langle\mathbf{r}_i+\rho,\alpha_j|\times \\ \times\int_0^1 ds\, e^{\frac{i}{\hbar}s\delta_{ij}\cdot\mathbf{\Pi}}\,|\mathbf{r},\alpha_j\rangle\langle\mathbf{r},\alpha_j|\,e^{\frac{i}{\hbar}(1-s)\delta_{ij}\cdot\mathbf{\Pi}}\,. \tag{D.9}$$

D.3 Paramagnetic current, linear response and orbital susceptibility

In the absence of fields, the Hamiltonian Bloch matrix, $\hat{H}_{\mathbf{k}} = H_{\alpha\beta}(\mathbf{k})$, is

$$H_{\alpha\beta}(\mathbf{k}) = \frac{1}{N}\sum_{i(\alpha),j(\beta)} h_{ij}e^{i\mathbf{k}\cdot\delta_{ij}}\,, \tag{D.10}$$

where $i(\alpha)$ ($j(\beta)$) runs over all orbitals of α (β) index. The paramagnetic current operator in real space reads

$$\mathbf{J}(\mathbf{r}) = \frac{ie}{\hbar}\frac{1}{N}\sum_{i,j} h_{ij}\delta_{ij}\int_0^1 ds|\mathbf{r}-s\delta_{ij},\alpha_i\rangle\langle\mathbf{r}+(1-s)\delta_{ij},\beta_j| \tag{D.11}$$

with Fourier components

$$\mathbf{J}(\mathbf{q}) = \frac{e}{\hbar}\frac{1}{V^{1/2}}\sum_{\alpha,\beta}\sum_{\mathbf{k}}|\mathbf{k}-\mathbf{q}/2,\alpha\rangle\gamma_{\alpha\beta}(\mathbf{k},\mathbf{q})\langle\mathbf{k}+\mathbf{q}/2,\beta|\,, \tag{D.12}$$

total volume V, and matrix kernel $\hat{\gamma}_{\mathbf{k},\mathbf{q}} = \gamma_{\alpha\beta}(\mathbf{k},\mathbf{q})$ given by

$$\gamma_{\alpha\beta}(\mathbf{k},\mathbf{q}) = \frac{1}{N}\sum_{i(\alpha),j(\beta)} ih_{ij}\delta_{ij}e^{i\mathbf{k}\cdot\delta_{ij}}\mathrm{sinc}(\mathbf{q}\cdot\delta_{ij}/2)\,, \tag{D.13}$$

where $\mathrm{sinc}(x) = \sin(x)/x$.

In the presence of fields, the Hamiltonian is perturbed to linear order by $V = -\sum_{\mathbf{q}} \mathbf{J}(\mathbf{q}) \cdot \mathcal{A}(-\mathbf{q})$, and linear response prescribes the result $\langle \mathbf{J}(\mathbf{q}) \rangle = \chi(\mathbf{q}) \mathcal{A}(\mathbf{q})$, with

$$\begin{aligned} \chi(\mathbf{q}) = & \frac{e^2}{\hbar^2} \frac{1}{2\pi i} \int dE \, n_F(E) \frac{1}{V} \times \\ & \times \sum_{\mathbf{k}} \mathrm{Tr}\{ \hat{\gamma}_{\mathbf{k},\mathbf{q}} \hat{G}^r_{\mathbf{k}+\mathbf{q}/2} \hat{\gamma}_{\mathbf{k},-\mathbf{q}} \hat{G}^r_{\mathbf{k}-\mathbf{q}/2} + \\ & - \hat{\gamma}_{\mathbf{k},\mathbf{q}} \hat{G}^a_{\mathbf{k}+\mathbf{q}/2} \hat{\gamma}_{\mathbf{k},-\mathbf{q}} \hat{G}^a_{\mathbf{k}-\mathbf{q}/2} \} \, , \end{aligned} \tag{D.14}$$

with retarded and advanced Green's function for the unperturbed Hamiltonian, $\hat{G}^{r,a}(E) = (E \pm i0^+ - \hat{H})^{-1}$, diagonal in Bloch space $\hat{G}^{r,a}_{\mathbf{k}}(E) = (E \pm i0^+ - \hat{H}_{\mathbf{k}})^{-1}$. This expression is valid for arbitrary $\mathbf{q}$. To study the low $\mathbf{q}$ limit, pertinent for a uniform magnetic field, it is convenient to define the following auxiliary tensor,

$$\begin{aligned} \chi_0(\mathbf{q}) = & \frac{e^2}{\hbar^2} \frac{1}{2\pi i} \int dE \, n_F(E) \frac{1}{V} \times \\ & \times \sum_{\mathbf{k}} \mathrm{Tr}\{ \hat{\gamma}_{\mathbf{k}} \hat{G}^r_{\mathbf{k}+\mathbf{q}/2} \hat{\gamma}_{\mathbf{k}} \hat{G}^r_{\mathbf{k}-\mathbf{q}/2} - \hat{\gamma}_{\mathbf{k}} \hat{G}^a_{\mathbf{k}+\mathbf{q}/2} \hat{\gamma}_{\mathbf{k}} \hat{G}^a_{\mathbf{k}-\mathbf{q}/2} \} \, , \end{aligned} \tag{D.15}$$

where vertex matrices in Eq. (D.14) have been taken at $\mathbf{q} = 0$. The physical response for a uniform magnetic field, $\chi_{\mathrm{phys}}(\mathbf{q})$, is given by the q^2 term in the expansion of $\chi_0(\mathbf{q})$:

$$\chi_{\mathrm{phys}}(\mathbf{q} \approx 0) = \chi_0(\mathbf{q}) - \chi(\mathbf{q} = 0) + \mathcal{O}(q^4) \, . \tag{D.16}$$

For a uniform magnetic field along an arbitrary direction $\hat{\mathbf{z}}$, the orbital magnetic susceptibility corresponds to

$$\frac{\chi_{\mathrm{orb}}}{\mu_0} = \lim_{q \to 0} \frac{1}{q^2} \chi^{yy}_{\mathrm{phys}}(q\hat{\mathbf{x}}) \, , \tag{D.17}$$

x and y being orthogonal axis in the plane perpendicular to $\hat{\mathbf{z}}$. A Taylor expansion of $(\Delta_{\pm} \hat{G}_{\mathbf{k}})$ to order q^2 with repeated use of the relation $\nabla \hat{G}_{\mathbf{k}} = \hat{G}_{\mathbf{k}} \hat{\gamma}_{\mathbf{k}} \hat{G}_{\mathbf{k}}$, and standard manipulations then lead to Eq. (5.1) of Ch. 5, with $\mathbf{k}$ dependencies removed and $\hat{G} = \hat{G}^r$. The result was first obtained in Ref. [45] as a necessary tight-binding generalization of Fukuyama's result.[187]

There is an additional contribution to the paramagnetic current response, $\langle \Delta \mathbf{J}(\mathbf{q}) \rangle = \Delta\chi(\mathbf{q}) \mathcal{A}(\mathbf{q})$, coming from the ignored q dependence of vertex matrices $\hat{\gamma}_{\mathbf{k},\mathbf{q}}$, and given to order q^2 by the following expression in dyadic form

$$\Delta\chi(\mathbf{q}) = \frac{e^2}{\hbar^2} \frac{1}{N} \sum_{i,j} \langle H_{ij} \rangle \delta_{ij} \, \delta_{ij} [1 - 2\mathrm{sinc}(\mathbf{q} \cdot \delta_{ij}/2)] \, , \tag{D.18}$$

but it does not show up in the physical current, being canceled by the diamagnetic term as we now show.

D.4 Diamagnetic current and cancellation

Unlike the traditional case, the current operator of Eq. (D.9) has terms to all orders in the field. To the linear order relevant here, functional differentiation of Eq. (D.9) leads to the following expression for the diamagnetic current in real space[80]

$$\langle \mathbf{J}_{\rm dia}(\mathbf{r})\rangle = \frac{e^2}{\hbar^2}\frac{1}{N}\sum_{i,j}\delta_{ij}\delta_{ij}\langle H_{ij}\rangle \int_0^1 ds \int_0^1 ds' \times \\ \times \left[s\mathcal{A}(\mathbf{r}-ss'\delta_{ij}) + s'\mathcal{A}(\mathbf{r}+ss'\delta_{ij})\right], \tag{D.19}$$

already evaluated in the ground state. In Fourier space, $\langle \mathbf{J}_{\rm dia}(\mathbf{q})\rangle = \chi_{\rm dia}(\mathbf{q})\mathcal{A}(\mathbf{q})$, the diamagnetic tensor reads

$$\chi_{\rm dia}(\mathbf{q}) = \frac{e^2}{\hbar^2}\frac{1}{N}\sum_{i,j}\langle H_{ij}\rangle\delta_{ij}\delta_{ij}{\rm sinc}^2(\mathbf{q}\cdot\delta_{ij}/2)\,. \tag{D.20}$$

In contrast with the usual case, the diamagnetic contribution has q-dependence beyond the constant term,[80] and its calculation for a uniform magnetic field has to be completed to order q^2. Combining Eq. (D.20) with the previous contribution from the paramagnetic current, Eq. (D.18), the announced cancellation takes place

$$\chi_{\rm dia}(\mathbf{q}) + \Delta\chi(\mathbf{q}) = 0 + \mathcal{O}(q^4)\,, \tag{D.21}$$

leaving alone $\chi_{\rm phys}$ as the physical response to a uniform field, with the known Eq. (5.1) for the magnetic susceptibility.

D.5 Absence of longitudinal response

A longitudinal, static vector potential is a gauge transformation, without physical effects. Our gauge invariant perturbative response should then vanish to all orders, and we explicitly show it to the calculated q^2 order. The longitudinal response to a longitudinal vector potential along an arbitrary direction $\hat{\mathbf{x}}$ is given by

$$\frac{\chi^{xx}_{\rm phys}(q\hat{\mathbf{x}})}{q^2/V} \propto \sum_{\mathbf{k}} {\rm Tr}\left\{\hat\gamma^x\hat G\hat\gamma^x\hat G\hat\gamma^x\hat G\hat\gamma^x\hat G + \hat G\hat\gamma^x\hat G\hat\gamma^x\hat G\frac{\partial\hat\gamma^x}{\partial k_x}\right\}, \tag{D.22}$$

with factors irrelevant for the argument ignored. Up to a total derivative, the second trace cancels the first one,

$$\begin{aligned}{\rm Tr}\left\{\hat G\hat\gamma^x\hat G\hat\gamma^x\hat G\frac{\partial\hat\gamma^x}{\partial k_x}\right\} &= -{\rm Tr}\{\hat\gamma^x\hat G\hat\gamma^x\hat G\hat\gamma^x\hat G\hat\gamma^x\hat G\}+ \\ &+\frac{1}{3}\frac{\partial}{\partial k_x}{\rm Tr}\{\hat G\hat\gamma^x\hat G\hat\gamma^x\hat G\hat\gamma^x\}\,,\end{aligned} \tag{D.23}$$

and the longitudinal response vanishes, $\chi^{xx}_{\rm phys}(q\hat{\mathbf{x}}) = 0$. In a similar way, it can be shown that a longitudinal static perturbation does not produce a transverse response, $\chi^{yx}_{\rm phys}(q\hat{\mathbf{x}}) = 0$, and vice versa.

D.6 Sum rule

The susceptibility sum rule,

$$\int dE_F \; \chi_{\rm orb}(E_F) = 0\,, \tag{D.24}$$

was first stated in Ref. [45]. Its proof from this formalism is direct. Writing as $E_F \frac{d\chi_{\rm orb}}{dE_F}$ the integrand in Eq. (D.24) from partial integration, then $\frac{d\chi_{\rm orb}}{dE_F}$ is the zero-temperature energy integrand of Eq. (5.1) evaluated at E_F. It is the imaginary part of an analytic complex function in the upper complex plane, thanks to the presence of products of $\hat{G}^r$. Closing the contour with the standard semicircle, where the integral vanishes owing to the asymptotic behavior $\hat{G}^r(z) \sim z^{-1}$, completes the proof. The sum rule also holds at finite temperatures, where responses for non-interacting electrons are always a convolution of zero temperature results with the unit area function $\beta/(4\cosh^2(\beta\mu/2))$.

Bibliography

[1] Kostya S. KS Novoselov, Andre K. AK Geim, S. V. SV Morozov, D. Jiang, Y_ Zhang, S. V. Dubonos, , I. V. Grigorieva, and A. A. Firsov. Electric field effect in atomically thin carbon films. *Science*, 306(5696):666–669, 2004.

[2] Philip Richard Wallace. The band theory of graphite. *Physical Review*, 71(9):622, 1947.

[3] A. K. Geim and K. S. Novoselov. The rise of graphene. *Nature Materials*, 6(3):183–191, 2007.

[4] AH Castro Neto, F. Guinea, N. M. R. Peres, Kostya S. Novoselov, and Andre K. Geim. The electronic properties of graphene. *Reviews of modern physics*, 81(1):109, 2009.

[5] N. Stander, B. Huard, and D. Goldhaber-Gordon. Evidence for klein tunneling in graphene p- n junctions. *Physical Review Letters*, 102(2):026807, 2009.

[6] K. S. Novoselov, D. Jiang, F. Schedin, T. J. Booth, V. V. Khotkevich, S. V. Morozov, and A. K. Geim. Two-dimensional atomic crystals. *Proceedings of the National Academy of Sciences of the United States of America*, 102(30):10451–10453, 2005.

[7] Yuanbo Zhang, Yan-Wen Tan, Horst L. Stormer, and Philip Kim. Experimental observation of the quantum hall effect and berry's phase in graphene. *Nature*, 438(7065):201–204, 2005.

[8] N. M. R. Peres. Colloquium: The transport properties of graphene: An introduction. *Reviews of Modern Physics*, 82(3):2673, 2010.

[9] Kin Fai Mak, Matthew Y. Sfeir, Yang Wu, Chun Hung Lui, James A. Misewich, and Tony F. Heinz. Measurement of the optical conductivity of graphene. *Physical review letters*, 101(19):196405, 2008.

[10] Francesco Bonaccorso, Z. Sun, Ta Hasan, and A. C. AC Ferrari. Graphene photonics and optoelectronics. *Nature photonics*, 4(9):611–622, 2010.

[11] M. I. Katsnelson, K. S. Novoselov, and A. K. Geim. Chiral tunnelling and the klein paradox in graphene. *Nat Phys*, 2(9):620–625, 2006.

[12] A. J. Martínez-Galera, I. Brihuega, A. Gutiérrez-Rubio, T. Stauber, and J. M. Gómez-Rodríguez. Towards scalable nano-engineering of graphene. *Scientific Reports*, 4:7314, 2014.

[13] Qing Hua Wang, Kourosh Kalantar-Zadeh, Andras Kis, Jonathan N. Coleman, and Michael S. Strano. Electronics and optoelectronics of two-dimensional transition metal dichalcogenides. *Nature Nanotechnology*, 7(11):699–712, 2012.

[14] A. K. Geim and I. V. Grigorieva. Van der Waals heterostructures. *Nature*, 499(7459):419–425, 2013.

[15] Wanxiang Feng, Yugui Yao, Wenguang Zhu, Jinjian Zhou, Wang Yao, and Di Xiao. Intrinsic spin hall effect in monolayers of group-vi dichalcogenides: A first-principles study. *Physical Review B - Condensed Matter and Materials Physics*, 86(16):165108, 2012.

[16] Di Xiao. Valley-contrasting physics in graphene: Magnetic moment and topological transport. *Physical Review Letters*, 99(23):236809, 2007.

[17] Di Xiao, Gui-Bin Liu, Wanxiang Feng, Xiaodong Xu, and Wang Yao. Coupled spin and valley physics in monolayers of mos2 and other group-vi dichalcogenides. *Physical Review Letters*, 108(19):196802, 2012.

[18] Hiram J. Conley, Bin Wang, Jed I. Ziegler, Richard F. Haglund, Sokrates T. Pantelides, and Kirill I. Bolotin. Bandgap Engineering of Strained Monolayer and Bilayer MoS2. *Nano Letters*, 13(8):3626–3630, 2013.

[19] A. Kuc, N. Zibouche, and T. Heine. Influence of quantum confinement on the electronic structure of the transition metal sulfide ts2. *Physical Review B*, 83(24):245213, 2011.

[20] Wang Yao, Di Xiao, and Qian Niu. Valley-dependent optoelectronics from inversion symmetry breaking. *Physical Review B*, 77(23):235406, 2008.

[21] Hualing Zeng, Junfeng Dai, Wang Yao, Di Xiao, and Xiaodong Cui. Valley polarization in MoS2 monolayers by optical pumping. *Nature Nanotechnology*, 7(8):490–493, 2012.

[22] C. R. Dean, A. F. Young, I. Meric, C. Lee, L. Wang, S. Sorgenfrei, K. Watanabe, T. Taniguchi, P. Kim, K. L. Shepard, and J. Hone. Boron nitride substrates for high-quality graphene electronics. *Nature Nanotechnology*, 5(10):722–726, 2010.

[23] W. Gannett, W. Regan, K. Watanabe, T. Taniguchi, M. F. Crommie, and A. Zettl. Boron nitride substrates for high mobility chemical vapor deposited graphene. *Applied Physics Letters*, 98(24):242105, 2011.

[24] Pablo San-Jose, A. Gutiérrez-Rubio, Mauricio Sturla, and Francisco Guinea. Spontaneous strains and gap in graphene on boron nitride. *Physical Review B*, 90(7):075428, 2014.

[25] B. Amorim, A. Cortijo, F. de Juan, A.G. Grushin, F. Guinea, A. Gutiérrez-Rubio, H. Ochoa, V. Parente, R. Roldán, P. San-Jose, J. Schiefele, M. Sturla, and M.A.H. Vozmediano. Novel effects of strains in graphene and other two dimensional materials. *Physics Reports*, 617:1–54, 2016.

[26] Yu Guo, Ward Newman, Cristian L. Cortes, and Zubin Jacob. Applications of Hyperbolic Metamaterial Substrates. *Advances in OptoElectronics*, 2012:e452502, 2012.

[27] Zhaowei Liu, Hyesog Lee, Yi Xiong, Cheng Sun, and Xiang Zhang. Far-field optical hyperlens magnifying sub-diffraction-limited objects. *Science*, 315(5819):1686–1686, 2007.

[28] Joshua D. Caldwell, Lucas Lindsay, Vincenzo Giannini, Igor Vurgaftman, Thomas L. Reinecke, Stefan A. Maier, and Orest J. Glembocki. Low-loss, infrared and terahertz nanophotonics using surface phonon polaritons. *Nanophotonics*, 4(1):44–68, 2015.

[29] Joshua D. Caldwell, Andrey V. Kretinin, Yiguo Chen, Vincenzo Giannini, Michael M. Fogler, Yan Francescato, Chase T. Ellis, Joseph G. Tischler, Colin R. Woods, Alexander J. Giles, Minghui Hong, Kenji Watanabe, Takashi Taniguchi, Stefan A. Maier, and Kostya S. Novoselov. Sub-diffractional volume-confined polaritons in the natural hyperbolic material hexagonal boron nitride. *Nature Communications*, 5:5221, 2014.

[30] Alexander Poddubny, Ivan Iorsh, Pavel Belov, and Yuri Kivshar. Hyperbolic metamaterials. *Nature Photonics*, 7(12):948–957, 2013.

[31] Zubin Jacob, Leonid V. Alekseyev, and Evgenii Narimanov. Optical hyperlens: far-field imaging beyond the diffraction limit. *Optics express*, 14(18):8247–8256, 2006.

[32] Stefan Alexander Maier. *Plasmonics: fundamentals and applications*. Springer Science & Business Media, 2007.

[33] RH Ritchie. Plasma losses by fast electrons in thin films. *Physical Review*, 106(5):874, 1957.

[34] David Pines and David Bohm. A collective description of electron interactions: Ii. collective vs individual particle aspects of the interactions. *Physical Review*, 85(2):338, 1952.

[35] T. Stauber. Plasmonics in dirac systems: from graphene to topological insulators. *Journal of Physics: Condensed Matter*, 26(12):123201, 2014.

[36] Frank HL Koppens, Darrick E Chang, and F Javier Garcia de Abajo. Graphene plasmonics: a platform for strong light–matter interactions. *Nano letters*, 11(8):3370–3377, 2011.

[37] Long Ju, Baisong Geng, Jason Horng, Caglar Girit, Michael Martin, Zhao Hao, Hans A. Bechtel, Xiaogan Liang, Alex Zettl, Y. Ron Shen, and Others. Graphene plasmonics for tunable terahertz metamaterials. *Nature nanotechnology*, 6(10):630–634, 2011.

[38] Marinko Jablan, Hrvoje Buljan, and Marin Soljačić. Plasmonics in graphene at infrared frequencies. *Physical review B*, 80(24):245435, 2009.

[39] A. N. Grigorenko, Marco Polini, and K. S. Novoselov. Graphene plasmonics. *Nature photonics*, 6(11):749–758, 2012.

[40] S. Dai, Z. Fei, Q. Ma, A. S. Rodin, M. Wagner, A. S. McLeod, M. K. Liu, W. Gannett, W. Regan, K. Watanabe, and Others. Tunable phonon polaritons in atomically thin van der waals crystals of boron nitride. *Science*, 343(6175):1125–1129, 2014.

[41] S. Dai, Q. Ma, T. Andersen, A. S. Mcleod, Z. Fei, M. K. Liu, M. Wagner, K. Watanabe, T. Taniguchi, M. Thiemens, F. Keilmann, P. Jarillo-Herrero, M. M. Fogler, and D. N. Basov. Subdiffractional focusing and guiding of polaritonic rays in a natural hyperbolic material. *Nature Communications*, 6:6963, 2015.

[42] C. L. Cortes, W. Newman, S. Molesky, and Z. Jacob. Quantum nanophotonics using hyperbolic metamaterials. *Journal of Optics*, 14(6):063001, 2012.

[43] Arnaud Raoux, Frédéric Piéchon, Jean-Noël Fuchs, and Gilles Montambaux. Orbital magnetism in coupled-bands models. *Physical Review B*, 91(8):085120, 2015.

[44] Mikito Koshino and Tsuneya Ando. Orbital diamagnetism in multilayer graphenes: Systematic study with the effective mass approximation. *Physical Review B*, 76(8):085425, 2007.

[45] G Gómez-Santos and T Stauber. Measurable lattice effects on the charge and magnetic response in graphene. *Phys. Rev. Lett.*, 106(4):045504, 2011.

[46] T. Thonhauser, Davide Ceresoli, David Vanderbilt, and R. Resta. Orbital magnetization in periodic insulators. *Physical Review Letters*, 95(13):137205, 2005.

[47] A. Raoux, M. Morigi, J.-N. Fuchs, F. Piéchon, and G. Montambaux. From dia- to paramagnetic orbital susceptibility of massless fermions. *Physical Review Letters*, 112(2):026402, 2014.

[48] Yang Gao, Shengyuan A. Yang, and Qian Niu. Geometrical effects in orbital magnetic susceptibility. *Phys. Rev. B*, 91:214405, 2015.

[49] David Pines. *Elementary excitations in solids: lectures on phonons, electrons, and plasmons*, volume 5. WA Benjamin, 1964.

[50] Andreas Otto. Excitation of nonradiative surface plasma waves in silver by the method of frustrated total reflection. *Zeitschrift für Physik*, 216(4):398, 1968.

[51] Erwin Kretschmann. Die bestimmung optischer konstanten von metallen durch anregung von oberflächenplasmaschwingungen. *Zeitschrift für Physik*, 241(4):313, 1971.

[52] Francisco J Garcia-Vidal, Luis Martin-Moreno, TW Ebbesen, and L Kuipers. Light passing through subwavelength apertures. *Reviews of Modern Physics*, 82(1):729, 2010.

[53] Ekmel Ozbay. Plasmonics: merging photonics and electronics at nanoscale dimensions. *Science*, 311(5758):189–193, 2006.

[54] Stefan A. Maier, Paul E. Barclay, Thomas J. Johnson, Michelle D. Friedman, and Oskar Painter. Low-loss fiber accessible plasmon waveguide for planar energy guiding and sensing. *Applied Physics Letters*, 84(20):3990–3992, 2004.

[55] Stefan A. Maier and Harry A. Atwater. Plasmonics: Localization and guiding of electromagnetic energy in metal/dielectric structures. *Journal of Applied Physics*, 98(1):011101, 2005.

[56] P. Berini, R. Charbonneau, N. Lahoud, and G. Mattiussi. Characterization of long-range surface-plasmon-polariton waveguides. *Journal of Applied Physics*, 98(4):043109, 2005.

[57] William L. Barnes, Alain Dereux, and Thomas W. Ebbesen. Surface plasmon subwavelength optics. *Nature*, 424(6950):824–830, 2003.

[58] RR Nair, P Blake, AN Grigorenko, KS Novoselov, TJ Booth, T Stauber, NMR Peres, and AK Geim. Fine structure constant defines visual transparency of graphene. *Science*, 320(5881):1308–1308, 2008.

[59] ZQ Li, Eric A Henriksen, Z Jiang, Zhao Hao, Michael C Martin, P Kim, HL Stormer, and Dimitri N Basov. Dirac charge dynamics in graphene by infrared spectroscopy. *Nature Physics*, 4(7):532–535, 2008.

[60] T Stauber, NMR Peres, and AH Castro Neto. Conductivity of suspended and non-suspended graphene at finite gate voltage. *Physical Review B*, 78(8):085418, 2008.

[61] Jianing Chen, Michela Badioli, Pablo Alonso-González, Sukosin Thongrattanasiri, Florian Huth, Johann Osmond, Marko Spasenović, Alba Centeno, Amaia Pesquera, Philippe Godignon, et al. Optical nano-imaging of gate-tunable graphene plasmons. *Nature*, 487(7405):77–81, 2012.

[62] Zhe Fei, AS Rodin, GO Andreev, W Bao, AS McLeod, M Wagner, LM Zhang, Z Zhao, M Thiemens, G Dominguez, et al. Gate-tuning of graphene plasmons revealed by infrared nano-imaging. *Nature*, 487(7405):82–85, 2012.

[63] B Wunsch, T Stauber, F Sols, and F Guinea. Dynamical polarization of graphene at finite doping. *New Journal of Physics*, 8(12):318, 2006.

[64] EH Hwang and S Das Sarma. Dielectric function, screening, and plasmons in two-dimensional graphene. *Physical Review B*, 75(20):205418, 2007.

[65] MR Ramezanali, MM Vazifeh, Reza Asgari, Marco Polini, and AH MacDonald. Finite-temperature screening and the specific heat of doped graphene sheets. *Journal of Physics A: Mathematical and Theoretical*, 42(21):214015, 2009.

[66] Tobias Stauber and Guillermo Gómez-Santos. Plasmons in layered structures including graphene. *New Journal of Physics*, 14(10):105018, 2012.

[67] T Stauber. Analytical expressions for the polarizability of the honeycomb lattice. *Physical Review B*, 82(20):201404, 2010.

[68] Tobias Stauber, John Schliemann, and NMR Peres. Dynamical polarizability of graphene beyond the dirac cone approximation. *Physical Review B*, 81(8):085409, 2010.

[69] Andreas Scholz and John Schliemann. Dynamical current-current susceptibility of gapped graphene. *Physical Review B*, 83(23):235409, 2011.

[70] Saeed H Abedinpour, Giovanni Vignale, A Principi, Marco Polini, Wang-Kong Tse, and AH MacDonald. Drude weight, plasmon dispersion, and ac conductivity in doped graphene sheets. *Physical Review B*, 84(4):045429, 2011.

[71] R Roldán, J-N Fuchs, and MO Goerbig. Collective modes of doped graphene and a standard two-dimensional electron gas in a strong magnetic field: Linear magnetoplasmons versus magnetoexcitons. *Physical Review B*, 80(8):085408, 2009.

[72] G Gómez-Santos and T Stauber. Graphene plasmons and retardation: Strong light-matter coupling. *EPL (Europhysics Letters)*, 99(2):27006, 2012.

[73] SA Mikhailov and K Ziegler. New electromagnetic mode in graphene. *Physical review letters*, 99(1):016803, 2007.

[74] Marinko Jablan, Hrvoje Buljan, and Marin Soljačić. Transverse electric plasmons in bilayer graphene. *Optics express*, 19(12):11236–11241, 2011.

[75] FMD Pellegrino, GGN Angilella, and R Pucci. Linear response correlation functions in strained graphene. *Physical Review B*, 84(19):195407, 2011.

[76] G Gómez-Santos and T Stauber. Fluorescence quenching in graphene: A fundamental ruler and evidence for transverse plasmons. *Physical Review B*, 84(16):165438, 2011.

[77] T Stauber and G Gómez-Santos. Plasmons and near-field amplification in double-layer graphene. *Physical Review B*, 85(7):075410, 2012.

[78] Sergey G Menabde, Daniel R Mason, Evgeny E Kornev, Changhee Lee, and Namkyoo Park. Direct optical probing of transverse electric mode in graphene. *Scientific reports*, 6, 2016.

[79] A Principi, Marco Polini, and Giovanni Vignale. Linear response of doped graphene sheets to vector potentials. *Physical Review B*, 80(7):075418, 2009.

[80] T Stauber and G Gómez-Santos. Dynamical current-current correlation of the hexagonal lattice and graphene. *Physical Review B*, 82(15):155412, 2010.

[81] Oskar Vafek. Thermoplasma polariton within scaling theory of single-layer graphene. *Physical review letters*, 97(26):266406, 2006.

[82] LA Falkovsky and AA Varlamov. Space-time dispersion of graphene conductivity. *The European Physical Journal B*, 56(4):281–284, 2007.

[83] OV Kotov, MA Kol'chenko, and Yu E Lozovik. Ultrahigh refractive index sensitivity of te-polarized electromagnetic waves in graphene at the interface between two dielectric media. *Optics express*, 21(11):13533–13546, 2013.

[84] Rosario EV Profumo, Reza Asgari, Marco Polini, and AH MacDonald. Double-layer graphene and topological insulator thin-film plasmons. *Physical Review B*, 85(8):085443, 2012.

[85] Gabriele Giuliani and Giovanni Vignale. *Quantum theory of the electron liquid*. Cambridge university press, 2005.

[86] LA Falkovsky and SS Pershoguba. Optical far-infrared properties of a graphene monolayer and multilayer. *Physical Review B*, 76(15):153410, 2007.

[87] PE Gaskell, HS Skulason, C Rodenchuk, and T Szkopek. Counting graphene layers on glass via optical reflection microscopy. *Applied physics letters*, 94(14):143101, 2009.

[88] Sukosin Thongrattanasiri, Frank HL Koppens, and F Javier García de Abajo. Complete optical absorption in periodically patterned graphene. *Physical review letters*, 108(4):047401, 2012.

[89] Thomas W Ebbesen, HJ Lezec, HF Ghaemi, Tineke Thio, and PA Wolff. Extraordinary optical transmission through sub-wavelength hole arrays. *Nature*, 391(6668):667–669, 1998.

[90] A. H. Castro Neto, F. Guinea, N. M. R. Peres, K. S. Novoselov, and A. K. Geim. The electronic properties of graphene. *Rev. Mod. Phys.*, 81:109–162, 2009.

[91] L. A. Ponomarenko, F. Schedin, M. I. Katsnelson, R. Yang, E. W. Hill, K. S. Novoselov, and A. K. Geim. Chaotic dirac billiard in graphene quantum dots. *Science*, 320(5874):356–358, 2008.

[92] Christian Volk, Christoph Neumann, Sebastian Kazarski, Stefan Fringes, Stephan Engels, Federica Haupt, André Müller, and Christoph Stampfer. Probing relaxation times in graphene quantum dots. *Nat Commun*, 4:1753, 2013.

[93] C. Stampfer, J. Güttinger, S. Hellmüller, F. Molitor, K. Ensslin, and T. Ihn. Energy gaps in etched graphene nanoribbons. *Phys. Rev. Lett.*, 102:056403, 2009.

[94] Jens Baringhaus, Ming Ruan, Frederik Edler, Antonio Tejeda, Muriel Sicot, Amina Taleb-Ibrahimi, An-Ping Li, Zhigang Jiang, Edward H Conrad, Claire Berger, et al. Exceptional ballistic transport in epitaxial graphene nanoribbons. *Nature*, 506(7488):349–354, 2014.

[95] Patrik Recher, Bjoern Trauzettel, Adam Rycerz, Ya M Blanter, CWJ Beenakker, and AF Morpurgo. Aharonov-bohm effect and broken valley degeneracy in graphene rings. *Phys. Rev. B*, 76(23):235404, 2007.

[96] B Wunsch, T Stauber, and F Guinea. Electron-electron interactions and charging effects in graphene quantum dots. *Phys. Rev. B*, 77(3):035316, 2008.

[97] Igor Romanovsky, Constantine Yannouleas, and Uzi Landman. Topological effects and particle physics analogies beyond the massless dirac-weyl fermion in graphene nanorings. *Phys. Rev. B*, 87(16):165431, 2013.

[98] PG Silvestrov and KB Efetov. Quantum dots in graphene. *Phys. Rev. Lett.*, 98(1):016802, 2007.

[99] A De Martino, L Dell'Anna, and R Egger. Magnetic confinement of massless dirac fermions in graphene. *Phys. Rev. Lett.*, 98(6):066802, 2007.

[100] NMR Peres, JNB Rodrigues, T Stauber, and JMB Lopes dos Santos. Dirac electrons in graphene-based quantum wires and quantum dots. *Journal of Physics: Condensed Matter*, 21(34):344202, 2009.

[101] S Rusponi, M Papagno, P Moras, S Vlaic, M Etzkorn, PM Sheverdyaeva, D Pacilé, H Brune, and C Carbone. Highly anisotropic dirac cones in epitaxial graphene modulated by an island superlattice. *Phys. Rev. Lett.*, 105(24):246803, 2010.

[102] B Hunt, JD Sanchez-Yamagishi, AF Young, M Yankowitz, Brian J LeRoy, K Watanabe, T Taniguchi, P Moon, M Koshino, P Jarillo-Herrero, et al. Massive dirac fermions and hofstadter butterfly in a van der waals heterostructure. *Science*, 340(6139):1427–1430, 2013.

[103] Michael S Fuhrer. Critical mass in graphene. *Science*, 340(6139):1413–1414, 2013.

[104] Jonas R.F. Lima. Controlling the energy gap of graphene by fermi velocity engineering. *arXiv:1412.0516v1*, 2014.

[105] GM Maksimova, ES Azarova, AV Telezhnikov, and VA Burdov. Graphene superlattice with periodically modulated dirac gap. *Phys. Rev. B*, 86(20):205422, 2012.

[106] Wei Liu, Z. F. Wang, Q. W. Shi, Jinlong Yang, and Feng Liu. Bandgap scaling of graphene nanohole superlattices. *Phys. Rev. B*, 80:233405, 2009.

[107] R Jackiw. Fractional and majorana fermions: the physics of zero-energy modes. *Physica Scripta*, 2012(T146):014005, 2012.

[108] Gerson J. Ferreira and Daniel Loss. Magnetically defined qubits on 3d topological insulators. *Phys. Rev. Lett.*, 111:106802, 2013.

[109] M Zahid Hasan and Charles L Kane. Colloquium: topological insulators. *Reviews of Modern Physics*, 82(4):3045, 2010.

[110] Xiao-Liang Qi and Shou-Cheng Zhang. Topological insulators and superconductors. *Reviews of Modern Physics*, 83(4):1057, 2011.

[111] Daniel Loss and David P DiVincenzo. Quantum computation with quantum dots. *Physical Review A*, 57(1):120, 1998.

[112] Björn Trauzettel, Denis V Bulaev, Daniel Loss, and Guido Burkard. Spin qubits in graphene quantum dots. *Nature Physics*, 3(3):192–196, 2007.

[113] A Rycerz, J Tworzydło, and CWJ Beenakker. Valley filter and valley valve in graphene. *Nature Physics*, 3(3):172–175, 2007.

[114] J. Güttinger, T. Frey, C. Stampfer, T. Ihn, and K. Ensslin. Spin states in graphene quantum dots. *Phys. Rev. Lett.*, 105:116801, 2010.

[115] Patrik Recher, Johan Nilsson, Guido Burkard, and Björn Trauzettel. Bound states and magnetic field induced valley splitting in gate-tunable graphene quantum dots. *Phys. Rev. B*, 79(8):085407, 2009.

[116] M. V. Berry and R. J. Mondragon. Neutrino billiards: Time-reversal symmetry-breaking without magnetic fields. *Proceedings of the Royal Society of London. A. Mathematical and Physical Sciences*, 412(1842):53–74, 1987.

[117] G. Giavaras and Franco Nori. Graphene quantum dots formed by a spatial modulation of the dirac gap. *Applied Physics Letters*, 97(24):–, 2010.

[118] G. Giavaras and Franco Nori. Dirac gap-induced graphene quantum dot in an electrostatic potential. *Phys. Rev. B*, 83:165427, 2011.

[119] Jia-Lin Zhu, Xingyuan Wang, and Ning Yang. Confined electronic states and their modulations in graphene nanorings. *Phys. Rev. B*, 86:125435, 2012.

[120] Patrik Recher and Björn Trauzettel. Quantum dots and spin qubits in graphene. *Nanotechnology*, 21(30):302001, 2010.

[121] N Levy, SA Burke, KL Meaker, M Panlasigui, A Zettl, F Guinea, AH Castro Neto, and MF Crommie. Strain-induced pseudo–magnetic fields greater than 300 tesla in graphene nanobubbles. *Science*, 329(5991):544–547, 2010.

[122] Z. F. Wang and Feng Liu. Nanopatterned graphene quantum dots as building blocks for quantum cellular automata. *Nanoscale*, 3:4201–4205, 2011.

[123] S. Marchini, S. Günther, and J. Wintterlin. Scanning tunneling microscopy of graphene on ru(0001). *Phys. Rev. B*, 76:075429, 2007.

[124] Yu S Dedkov, Michail Fonin, Ulrich Rüdiger, and Clemens Laubschat. Rashba effect in the graphene/ni (111) system. *Physical review letters*, 100(10):107602, 2008.

[125] Alexander Grüneis and Denis V. Vyalikh. Tunable hybridization between electronic states of graphene and a metal surface. *Phys. Rev. B*, 77:193401, 2008.

[126] Ivo Pletikosić, Marko Kralj, Petar Pervan, Radovan Brako, J Coraux, AT N'diaye, C Busse, and Th Michely. Dirac cones and minigaps for graphene on ir (111). *Physical Review Letters*, 102(5):056808, 2009.

[127] Norbert Nemec, David Tománek, and Gianaurelio Cuniberti. Modeling extended contacts for nanotube and graphene devices. *Physical Review B*, 77(12):125420, 2008.

[128] Sebastian Bleikamp, Peter J Feibelman, Thomas Michely, et al. Two-dimensional ir cluster lattice on a graphene moiré on ir (111). *Physical Review Letters*, 97(21):215501, 2006.

[129] Peter J. Feibelman. Pinning of graphene to ir(111) by flat ir dots. *Phys. Rev. B*, 77:165419, 2008.

[130] T. Stauber and R. Zimmermann. Optical absorption in quantum dots: Coupling to longitudinal optical phonons treated exactly. *Phys. Rev. B*, 73:115303, 2006.

[131] F Duncan M Haldane. Model for a quantum hall effect without landau levels: Condensed-matter realization of the" parity anomaly". *Phys. Rev. Lett.*, 61(18):2015, 1988.

[132] Mikito Koshino and Tsuneya Ando. Anomalous orbital magnetism in dirac-electron systems: Role of pseudospin paramagnetism. *Phys. Rev. B*, 81:195431, 2010.

[133] Paulina Plochocka, Clément Faugeras, Milan Orlita, Marcin L Sadowski, Gérard Martinez, Marek Potemski, Mark O Goerbig, J-N Fuchs, Claire Berger, and Walter A De Heer. High-energy limit of massless dirac fermions in multilayer graphene using magneto-optical transmission spectroscopy. *Phys. Rev. Lett.*, 100(8):087401, 2008.

[134] Tobias Stauber, NMR Peres, Francisco Guinea, and AH Castro Neto. Fermi liquid theory of a fermi ring. *Phys. Rev. B*, 75(11):115425, 2007.

[135] A. O. Govorov. Spin and energy transfer in nanocrystals without tunneling. *Phys. Rev. B*, 68:075315, 2003.

[136] Lukas Novotny and Bert Hecht. *Principles of nano-optics*. Cambridge university press, 2012.

[137] Jenö Sólyom. *Fundamentals of the Physics of Solids: Normal, Broken-Symmetry, and Correlated Systems*, volume 3. Springer, 2010.

[138] T Langer, DF Förster, C Busse, T Michely, H Pfnür, and C Tegenkamp. Sheet plasmons in modulated graphene on ir (111). *New Journal of Physics*, 13(5):053006, 2011.

[139] Xiaoji G. Xu, Behnood G. Ghamsari, Jian-Hua Jiang, Leonid Gilburd, Gregory O. Andreev, Chunyi Zhi, Yoshio Bando, Dmitri Golberg, Pierre Berini, and Gilbert C. Walker. One-dimensional surface phonon polaritons in boron nitride nanotubes. *Nature Communications*, 5:4782, 2014.

[140] Xiaodong Yang, Jie Yao, Junsuk Rho, Xiaobo Yin, and Xiang Zhang. Experimental realization of three-dimensional indefinite cavities at the nanoscale with anomalous scaling laws. *Nature Photonics*, 6(7):450–454, 2012.

[141] Peining Li, Martin Lewin, Andrey V. Kretinin, Joshua D. Caldwell, Kostya S. Novoselov, Takashi Taniguchi, Kenji Watanabe, Fabian Gaussmann, and Thomas Taubner. Hyperbolic phonon-polaritons in boron nitride for near-field optical imaging and focusing. *Nature Communications*, 6:7507, 2015.

[142] John Brian Pendry. Negative refraction makes a perfect lens. *Physical review letters*, 85(18):3966, 2000.

[143] Alessandro Salandrino and Nader Engheta. Far-field subdiffraction optical microscopy using metamaterial crystals: Theory and simulations. *Physical Review B*, 74(7):075103, 2006.

[144] L. R. Walker. Magnetostatic Modes in Ferromagnetic Resonance. *Physical Review*, 105(2):390–399, 1957.

[145] R. K. Fisher and R. W. Gould. Resonance Cones in the Field Pattern of a Short Antenna in an Anisotropic Plasma. *Physical Review Letters*, 22(21):1093–1095, 1969.

[146] H. T. Stinson, J. S. Wu, B. Y. Jiang, Z. Fei, A. S. Rodin, B. C. Chapler, A. S. McLeod, A. Castro Neto, Y. S. Lee, M. M. Fogler, and D. N. Basov. Infrared nanospectroscopy and imaging of collective superfluid excitations in anisotropic superconductors. *Physical Review B*, 90(1):014502, 2014.

[147] Filippo Alpeggiani and Lucio Claudio Andreani. Josephson surface plasmons in spatially confined cuprate superconductors. *Physical Review B*, 88(17):174513, 2013.

[148] Grzegorz Pawlik, Karol Tarnowski, Wiktor Walasik, Antoni C. Mitus, and I. C. Khoo. Liquid crystal hyperbolic metamaterial for wide-angle negative–positive refraction and reflection. *Optics letters*, 39(7):1744–1747, 2014.

[149] Ari Sihvola. Metamaterials in electromagnetics. *Metamaterials*, 1(1):2–11, 2007.

[150] Jenö Sólyom. *Fundamentals of the Physics of Solids: Volume 1: Structure and Dynamics*, volume 1. Springer Science & Business Media, 2007.

[151] Zhiwen Shi, Hans A. Bechtel, Samuel Berweger, Yinghui Sun, Bo Zeng, Chenhao Jin, Henry Chang, Michael C. Martin, Markus B. Raschke, and Feng Wang. Amplitude-and phase-resolved nanospectral imaging of phonon polaritons in hexagonal boron nitride. *ACS Photonics*, 2(7):790–796, 2015.

[152] M. M. Fogler, L. V. Butov, and K. S. Novoselov. High-temperature superfluidity with indirect excitons in van der Waals heterostructures. *Nature communications*, 5, 2014.

[153] Jacob B. Khurgin and Alexandra Boltasseva. Reflecting upon the losses in plasmonics and metamaterials. *MRS bulletin*, 37(08):768–779, 2012.

[154] Joshua D. Caldwell, Orest J. Glembocki, Yan Francescato, Nicholas Sharac, Vincenzo Giannini, Francisco J. Bezares, James P. Long, Jeffrey C. Owrutsky, Igor Vurgaftman, Joseph G. Tischler, and others. Low-loss, extreme subdiffraction photon confinement via silicon carbide localized surface phonon polariton resonators. *Nano letters*, 13(8):3690–3697, 2013.

[155] Max Born and Emil Wolf. *Principles of optics: electromagnetic theory of propagation, interference and diffraction of light*. CUP Archive, 2000.

[156] Matthias Brack and Rajat K. Bhaduri. *Semiclassical physics*, volume 96. Westview Press, 2003.

[157] A. Douglas Stone. Einstein's unknown insight and the problem of quantizing chaos. *Physics Today*, 58(8):37, 2005.

[158] Alfred Engel and E. Shucking. The Collected Papers of Albert Einstein. Vol. 6. The Berlin years: writings, 1914–1917. *English translation. Princeton University Press, Princeton*, 1997.

[159] Joseph B. Keller and S. I. Rubinow. Asymptotic solution of eigenvalue problems. *Annals of Physics*, 9(1):24–75, 1960.

[160] Joseph B. Keller. Corrected Bohr-Sommerfeld quantum conditions for nonseparable systems. *Annals of Physics*, 4(2):180–188, 1958.

[161] Joseph B. Keller. Semiclassical mechanics. *Siam Review*, 27(4):485–504, 1985.

[162] Vladimir Igorevich Arnol'd. *Mathematical methods of classical mechanics*, volume 60. Springer Science & Business Media, 2013.

[163] R. Landauer. Associated Legendre polynomial approximations. *Journal of Applied Physics*, 22(1):87–89, 1951.

[164] Zhiyuan Sun, Á Gutiérrez-Rubio, D. N. Basov, and M. M. Fogler. Hamiltonian optics of hyperbolic polaritons in nanogranules. *Nano letters*, 15(7):4455–4460, 2015.

[165] Vladimir A. Fonoberov and Alexander A. Balandin. Polar optical phonons in wurtzite spheroidal quantum dots: theory and application to ZnO and ZnO/MgZnO nanostructures. *Journal of Physics: Condensed Matter*, 17(7):1085, 2005.

[166] Zubin Jacob and Evgenii E. Narimanov. Optical hyperspace for plasmons: Dyakonov states in metamaterials. *Applied Physics Letters*, 93(22):221109, 2008.

[167] E. Cojocaru. Comparative analysis of Dyakonov hybrid surface waves at dielectric–elliptic and dielectric–hyperbolic media interfaces. *JOSA B*, 31(11):2558–2564, 2014.

[168] Osamu Takayama, Lucian-Cornel Crasovan, Steffen Kj\a er Johansen, Dumitru Mihalache, David Artigas, and Lluis Torner. Dyakonov surface waves: a review. *Electromagnetics*, 28(3):126–145, 2008.

[169] Osamu Takayama, David Artigas, and Lluis Torner. Lossless directional guiding of light in dielectric nanosheets using Dyakonov surface waves. *Nature nanotechnology*, 9(6):419–424, 2014.

[170] Drew Patrick Pulsifer, Muhammad Faryad, and Akhlesh Lakhtakia. Observation of the Dyakonov-Tamm wave. *Physical review letters*, 111(24):243902, 2013.

[171] Martin C. Gutzwiller. *Chaos in classical and quantum mechanics*, volume 1. Springer Science & Business Media, 2013.

[172] Herbert Goldstein. *Classical mechanics*. Pearson Education India, 1965.

[173] Michael V. Berry and Michael Tabor. Closed orbits and the regular bound spectrum. In *Proceedings of the Royal Society of London A: Mathematical, Physical and Engineering Sciences*, volume 349, pages 101–123. The Royal Society, 1976.

[174] L. M. Zhang, G. O. Andreev, Z. Fei, A. S. McLeod, G. Dominguez, M. Thiemens, A. H. Castro-Neto, D. N. Basov, and M. M. Fogler. Near-field spectroscopy of silicon dioxide thin films. *Physical Review B*, 85(7):075419, 2012.

[175] Alexander S. McLeod, P. Kelly, M. D. Goldflam, Z. Gainsforth, A. J. Westphal, Gerardo Dominguez, Mark H. Thiemens, Michael M. Fogler, and D. N. Basov. Model for quantitative tip-enhanced spectroscopy and the extraction of nanoscale-resolved optical constants. *Physical Review B*, 90(8):085136, 2014.

[176] B.-Y. Jiang, L. M. Zhang, AH Castro Neto, D. N. Basov, and M. M. Fogler. Generalized spectral method for near-field optical microscopy. *Journal of Applied Physics*, 119(5):054305, 2016.

[177] James R. Wait. Some solutions for electromagnetic problems involving spheroidal, spherical, and cylindrical bodies. *Res. NBS (Math. and Mathematical Physics) B*, 64:15–32, 1959.

[178] Philip McCord Morse, Herman Feshbach, and others. *Methods of theoretical physics*, volume 1. McGraw-Hill New York, 1953.

[179] E. I. Blount. Bloch electrons in a magnetic field. *Phys. Rev.*, 126:1636–1653, 1962.

[180] Prasanta K. Misra and Laura M. Roth. Theory of diamagnetic susceptibility of metals. *Phys. Rev.*, 177:1089–1102, 1969.

[181] Neil W Ashcroft and N David Mermin. Solid state phys. *Saunders, Philadelphia*, page 293, 1976.

[182] K. S. Novoselov, A. K. Geim, S. V. Morozov, D. Jiang, M. I. Katsnelson, I. V. Grigorieva, S. V. Dubonos, and A. A. Firsov. Two-dimensional gas of massless dirac fermions in graphene. *Nature*, 438(7065):197–200, 2005.

[183] Junren Shi, G. Vignale, Di Xiao, and Qian Niu. Quantum theory of orbital magnetization and its generalization to interacting systems. *Phys. Rev. Lett.*, 99:197202, 2007.

[184] Di Xiao, Ming-Che Chang, and Qian Niu. Berry phase effects on electronic properties. *Reviews of modern physics*, 82(3):1959, 2010.

[185] T Thonhauser. Theory of orbital magnetization in solids. *International Journal of Modern Physics B*, 25(11):1429–1458, 2011.

[186] Yang Gao, Shengyuan A. Yang, and Qian Niu. Field induced positional shift of bloch electrons and its dynamical implications. *Phys. Rev. Lett.*, 112:166601, 2014.

[187] Hidetoshi Fukuyama. Theory of orbital magnetism of bloch electrons: Coulomb interactions. *Progress of Theoretical Physics*, 45(3):704–729, 1971.

[188] S. A. Safran and F. J. DiSalvo. Theory of magnetic susceptibility of graphite intercalation compounds. *Phys. Rev. B*, 20:4889–4895, 1979.

[189] G Vignale. Orbital paramagnetism of electrons in a two-dimensional lattice. *Phys. Rev. Lett.*, 67(3):358, 1991.

[190] R Peierls. On the theory of diamagnetism of conduction electrons. *Z. Phys*, 80:763–791, 1933.

[191] Yuya Ominato and Mikito Koshino. Orbital magnetism of graphene nanostructures. *Solid State Communications*, 175–176:51 – 61, 2013. Special Issue: Graphene V: Recent Advances in Studies of Graphene and Graphene analogues.

[192] R. V. Gorbachev, J. C. W. Song, G. L. Yu, A. V. Kretinin, F. Withers, Y. Cao, A. Mishchenko, I. V. Grigorieva, K. S. Novoselov, L. S. Levitov, and A. K. Geim. Detecting topological currents in graphene superlattices. *Science*, 346(6208):448–451, 2014.

[193] Habib Rostami and Reza Asgari. Valley zeeman effect and spin-valley polarized conductance in monolayer mos 2 in a perpendicular magnetic field. *Physical Review B*, 91(7):075433, 2015.

[194] Zhilin Li, Lianlian Chen, Sheng Meng, Liwei Guo, Jiao Huang, Yu Liu, Wenjun Wang, and Xiaolong Chen. Field and temperature dependence of intrinsic diamagnetism in graphene: Theory and experiment. *Physical Review B*, 91(9):094429, 2015.

[195] Andor Kormányos, Viktor Zólyomi, Neil D. Drummond, Péter Rakyta, Guido Burkard, and Vladimir I. Fal'ko. Monolayer mos_2: Trigonal warping, the γ valley, and spin-orbit coupling effects. *Phys. Rev. B*, 88:045416, 2013.

[196] E. Cappelluti, R. Roldán, J. Silva-Guillén, P. Ordejón, and F. Guinea. Tight-binding model and direct-gap/indirect-gap transition in single-layer and multilayer mos_2. *Phys. Rev. B*, 88:075409, 2013.

[197] J. W. McClure. Diamagnetism of graphite. *Phys. Rev.*, 104:666–671, 1956.

[198] J. W. McClure. Theory of diamagnetism of graphite. *Phys. Rev.*, 119:606–613, 1960.

[199] A Principi, Marco Polini, Giovanni Vignale, and Mikhail Iosifovich Katsnelson. Many-body orbital paramagnetism in doped graphene sheets. *Phys. Rev. Lett.*, 104(22):225503, 2010.

[200] Shengjun Yuan, Malte Rösner, Alexander Schulz, Tim O. Wehling, and Mikhail I. Katsnelson. Electronic structures and optical properties of partially and fully fluorinated graphene. *Phys. Rev. Lett.*, 114:047403, 2015.

[201] Ryogo Kubo. Statistical-mechanical theory of irreversible processes. i. general theory and simple applications to magnetic and conduction problems. *Journal of the Physical Society of Japan*, 12(6):570–586, 1957.

[202] Alexander L Fetter and John Dirk Walecka. *Quantum theory of many-particle systems*. Courier Corporation, 2003.

[203] Gerald D Mahan. *Many-particle physics*. Springer Science & Business Media, 2013.

[204] Henrik Bruus and Karsten Flensberg. *Many-body quantum theory in condensed matter physics: an introduction*. OUP Oxford, 2004.

[205] Murray Gell-Mann and Keith A Brueckner. Correlation energy of an electron gas at high density. *Physical Review*, 106(2):364, 1957.

[206] Milton Abramowitz and Irene Stegun. Handbook of mathematical functions. 1970.

[207] Vidal Alonso, Salvatore De Vincenzo, and Luigi Mondino. On the boundary conditions for the dirac equation. *European Journal of Physics*, 18(5):315, 1997.

[208] Edward McCann and Vladimir I Fal'ko. Symmetry of boundary conditions of the dirac equation for electrons in carbon nanotubes. *Journal of Physics: Condensed Matter*, 16(13):2371, 2004.